FORM FINDING OF COMPRESSIVELY SELF-SUPPORTING SURFACES

Kavinda Isuru Udayanga Nanayakkara

178095V

Degree of Master of Science

Department of Civil Engineering

University of Moratuwa

Sri Lanka

February 2019

FORM FINDING OF COMPRESSIVELY SELF-SUPPORTING SURFACES

Kavinda Isuru Udayanga Nanayakkara

178095V

Thesis submitted in partial fulfilment of the requirements for the degree
Master of Science in Civil Engineering

Department of Civil Engineering

University of Moratuwa

Sri Lanka

February 2019

DECLARATION

I declare that this is my own work and this thesis does not incorporate without acknowledgement any material previously submitted for a degree or diploma in any other University or institute of higher learning, and to the best of my knowledge and belief it does not contain any material previously published or written by another person except where the acknowledgement is made in the text.

Also, I hereby grant to University of Moratuwa the non-exclusive right to reproduce and distribute my thesis, in whole or in part, in print, electronic or other medium. I retain the right to use this content in whole or part in future works (such as articles or books).

Signature: Date:

The above candidate has carried out research for the masters thesis under my supervision.

Name of the supervisor: Prof W.P.S. Dias

Signature of the supervisor: Date:

ABSTRACT

Compression-only surfaces are efficient structural forms as they fully utilize material at every cross-section. Thrust Network Analysis is a versatile tool which can be used for form exploration of compression-only surfaces. However, the form finding ability comes with the limitation of loading being in a single direction (e.g. gravity). As such, Thrust Network Analysis is not readily usable for form exploration under combined gravity and lateral loadings, such as seismic and wind loading. This research attempts to address this shortcoming by providing feedback to designers on the seismic capacity and wind loading capacity of the form while allowing them to carry out form exploration under gravity only loading condition.

For two dimensional arch forms and three-dimensional shells a procedure to provide real-time feedback on the thickness requirements of the form under seismic loading condition is proposed and implemented. For the case of a symmetric catenary arch subjected to a uniformly distributed loading a general solution for the thickness requirements can be given in a graphical format. It is further observed that the seismic loading capacity of compression only forms can be improved by bulking the supports.

A procedure is presented to provide similar feedback for two-dimensional compression-only surfaces subjected to combined gravity and wind loading. The feedback procedure and hence the usage of the feedback information in the design procedures differ for seismic and wind loadings, as seismic loads acts as a set of parallel loads and wind load acts perpendicular to the surface.

Keywords: compression-only forms, Thrust Network Analysis, quasi-static seismic loading, wind loading, design feedback

DEDICATION

To the giants, upon whose shoulders I stand.

ACKNOWLEDGEMENT

My work towards a Master of Science Degree and this thesis would not have been successful if not for the guidance and support from many individuals who devoted their time and resources towards the success of this project.

I am very much thankful to my research supervisor, Prof. Priyan Dias, for his guidance and support throughout the research project. If not for his guidance and motivation this research project would not have gotten so far.

The research work included an extensive literature survey and study of historical structures. I owe much to the long list of researchers who shared their work in various ways, including on ResearchGate® platform. The assistance provided by Dr. Tim Michiels in sharing his research results and providing clarifications, and Dr. Dhananjaya Gamalath in providing relevant details on historical vaults and domes of Sri Lanka, is specially appreciated.

Prof. Rangika Halwatura and Dr. Chinthaka Mallikarachchi of the progress review committee and the fellow research assistants at Department of Civil Engineering of University of Moratuwa are acknowledged for their critical comments which were useful in refining and guiding the work towards a successful outcome.

The research work was partially funded by a short-term grant (SRC/ST/2018/17) from the Senate Research Committee of the University of Moratuwa. Furthermore, I am thankful to the National Science Foundation for providing partial funds to present work relating to this project at the Annual Symposium of the International Association of Shell and Spatial Structures (IASS) 2018 at Boston, USA and to the Educational Trust of the Institution of Structural Engineers (IStructE) whose Pai Lin Li Travel Award provided a remarkable opportunity to expose myself to work on shell structures done in India and Europe.

Finally, I owe a huge debt of gratitude to my parents for believing in my work and supporting me in various ways, including financial assistance when needed.

With the support from those who are mentioned here by name and otherwise, my research towards the Master of Science Degree became a successful endeavour and it is my wish that its findings would be beneficial to science and mankind.

TABLE OF CONTENTS

LIST OF FIGURES

LIST OF TABLES

LIST OF ABBREVIATIONS

Abbreviation	Description
AD	Anno Domini
BC	Before Christ
CAD	Computer Aided Draughting
FEM	Finite Element Method
GUI	Graphical User Interface
PhD	Doctor of Philosophy
SQP	Sequential Quadratic Programming
TNA	Thrust Network Analysis

1. INTRODUCTION

Compressively self-supported unreinforced masonry structures were designed and built as early as 1600s. Different analytical methodologies were developed and used for both analysis and form finding of compressively self-supporting surface structures, from unreinforced masonry vaults and domes in medieval Europe to very thin fibre reinforced concrete shells found in contemporary architecture.

As Bagrianski and Halpern [1] identifies, there are three primary form finding techniques for compression only surfaces: (i) Physical hanging models; (ii) Equilibrium methods; and (iii) Optimization schemes. Physical hanging models were brought to prominence by Antonia Gaudi, Heinz Isler and Frei Otto, at different points in history. However, equilibrium methods, which use the computational power of micro-processors, are currently in vogue. Dynamic relaxation, force density, stress distribution, thrust networks and particle spring models are equilibrium methods, to name but a few. Almost all the equilibrium methods are based on Heyman's safe theorem and Hooke's observation of funicular forms.

As historical vaulted masonry structures were built using large pieces of rock, major part of the load was due to their self-weight. This led to the reasonable assumption of loading being in the direction of gravity only. However, improvements in materials and production processes allowed for these structures to be lightweight, primarily motivated by the improved environmental performance achieved through the reduction of material usage. Consequently, this led to a lower contribution from self-weight and a higher significance on lateral loading (i.e. seismic and wind loading). This simultaneous presence of vertical and horizontal loads is excluded in the fundamental levels of more popular form finding methodologies, such as Thrust Network Analysis (TNA). As such a closer evaluation of the existing equilibrium methodologies are required to find ways to incorporate horizontal loading to form finding of compressively self-supporting surfaces.

Considering the use of computational power in these methodologies, it could be seen that improving computational efficiency can lead to time advantages in exploration of novel self-supporting forms. Furthermore, borrowing ideas from allied areas of studies such as computer science and mathematics could shed new light on the current understandings of the subject.

Based on the initial literature survey and study of existing form finding methodologies for self-supporting structures, the following were set as the main objectives of the study.

1. To identify the possibilities of improving computational efficiency of current methodologies, through improved mathematical formulation.
2. To identify the possibility of extending the existing equilibrium methodologies to consider horizontal and vertical loads, simultaneously, in form finding of compressively self-supporting structures.

The thesis includes three main chapters. Chapter 02 provides a concise recording of the existing compression-only structures of the world and the evolution of analysis and form-finding of compression-only forms. Thrust Network Analysis was identified as the most advanced and widely used equilibrium method for form-finding of compression-only forms and Chapter 03 presents the Thrust Network Analysis and presents an improved implementation of the methodology. Chapter 04 proposes methodologies for feedback procedures for analysis of compression-only forms under combined gravity and lateral loadings. This chapter further presents application of the procedures and comments on the results. Finally, Chapter 05 gives conclusions of the research and makes recommendations for future improvements upon the findings of the current research.

2. STUDY OF THE EVOLUTION OF CONSTRUCTION AND FORM FINDING OF COMPRESSIVELY SELF-SUPPORTING STRUCTURES

Compressively self-supporting structures were built long before the development of current tools in structural engineering design and analysis, and as such the body of knowledge in compressively self-supporting structures has its foundation in very early studies – Leonardo Da Vinci's (1452-1519) wedge model for arches and Hook's observation of hanging chain in 1676 - and lays the foundation for modern free-form compression-only structures, which are not confined to the traditional geometrical shapes.

A good starting point for this study of existing form finding methods of compressively self-supporting structures is to study the history of arches; the earliest compressively self-supporting forms. There are three intertwined timelines of interest, primarily identified by the progress and purpose of the developments. The longest and the primary timeline in an engineering perspective is the one showing how the practice of constructing compressively self-supporting structures has progressed. The second relates as to how the scientific theory has developed and refined, and this timeline starts in late middle ages (1250-1500AD) and shows rapid action during renaissance (1600-1800AD) and beyond. The third timeline has most of its development during the past couple of centuries and relates to the development of the thrust line and the limit analysis as we know now.

2.1. A Brief History of Compressively Self-Supporting Structures

As is the case with many key inventions of human history – fire and the wheel- it is not possible to pin-point where, when and how this mystery of architecture and construction – the arch- came about. It is commonly agreed that the true arches first came to be in Mesopotamia back in 3000BC, or earlier. Karl-Eugen Kurrer [2] notes that a 5000-year-old Mesopotamian burial chamber having a barrel vault of approximately 1m span is in display at the Berlin Museum of Prehistory and Ancient History. The barns of Ramesseum, Egypt (1200 BC) and the support structure of the

Hanging Gardens of Babylon (700BC) are further evidence of the use of arches in early civilizations [3].

Etruscans were the first to formalize the practice of building arches and as evident by the arches in the Etruscan wall of Perugia -300 BC, they have used specially cut and dressed stone for the arches. With the assimilation of Etruscan empire to the Roman Empire, after the Etruscan-Roman wars, the architectural elements too were integrated. Due to the Roman wars to follow, or otherwise, the art of building arches too was spread across the globe.

There is even evidence of arches in Teotihuacan - Mexico, where an arched roof tunnel was discovered under the Pyramid of Quetzalcoatl, in 2012 [4]. The construction was dated back to 200AD. There is evidence in literature of the existence of arches in ancient Chinese Empires, but none remain today as they were of wooden construction [5].

The Sassanian Empire (modern-day Iran) was a great exponent of arches, vaults and domes, commonly featuring those in castles -Ardashir I, Palace (Figure 2.1)- public spaces - Bishapur Hall, Shapur I, Kazerun (Figure 2.2)- places of worship -Anahita Temple - and even in bridges - Firozabad Bridge (Figure 2.3). Capture of Roman Valerians by Shapur I is a primary reason for this widespread use of arches and vaults [6].

Dhananjaya Gamalath [7] has carried out an extensive study on the Buddhist image houses of Sri Lanka constructed during Anuradhapura Kingdom (200BC to 1200AD). He identifies '*gedige*' as one of the four typologies used for image houses. The *gedige* image houses are identified by thick masonry walls which support a masonry domed roof, and likely to have been an enclosure for standing Buddha statues. Gamalath [7] concedes that the *gedige* tradition might have been inherited from India – primarily from the structures in Bithargoan, but the subsequent developments were local. He shows this by noting the progression of architectural and artistic elements of Buddha image houses through time and across different architectural types. Although he identifies 38 *gedige* image houses, only few of them still stand and the identification as *gedige* tradition is by remaining architectural and structural features. The remaining structures include Thivanka image house, Thuparama Image House [8]. The barrel vaults in the temple of Tooth Relic in Kandy (Figure 2.4) is one evidence of this structural form being in the repertoire of the ancient builders in Sri Lanka long after the Anuradhapura kingdom.

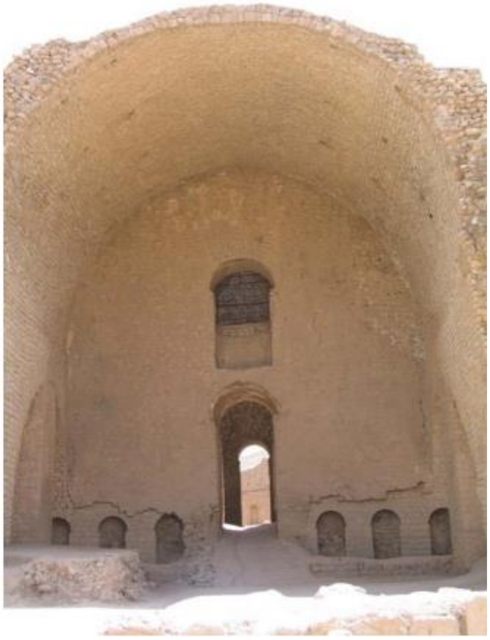

Figure 2.1: Barrel vault in Ardashir I Palace (3rd century AD). Source: Fig 2.4 from Motlagh [6].

Figure 2.2: An arch structure in Bishapur Hall (3rd Century AD). Source: Fig 2.6a from Motlagh [6].

Figure 2.3: Semi-circle arches in Firozabad Bridge. Source: Fig 2.2 from Motlagh [6].

With multiple foreign invasions the technological developments in Sri Lankan architecture stagnated, but the developments in the western empires continued. During the renaissance there were many impressive cathedrals incorporating massive domes- Santa Maria del Fiore in Florence -1418 AD (Figure 2.5) and St Peter's in Rome-between 1506 and 1626 AD (Figure 2.6) - innovative arch bridges – Ponte Santa Trinita -1566 AD (Figure 2.7) - constructed with both theory and practice developing alongside. However, the arch bridges did make its way back to Sri Lanka as the colonisers took to developing infrastructure, especially the railways, during the days of industrial revolution (e.g. Nine Arch Bridge in Demodara, Sri Lanka).

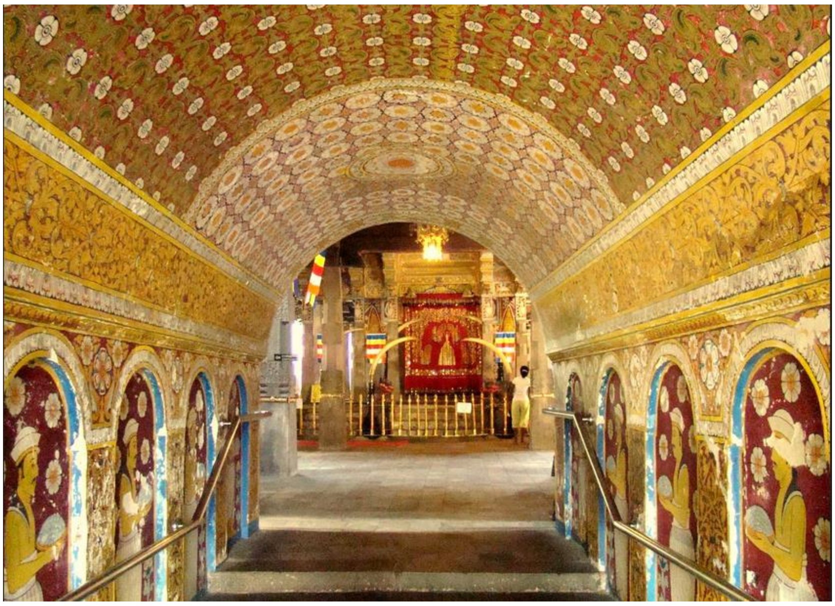

Figure 2.4: Barrel vault in Dalada Maligawa, Kandy.

Figure 2.5: Santa Maria del Fiore in Florence. Source: *http://teatriemusei.ovest.com*.

The early Roman arch (100BC) was a circular arch, which gives a rise to span ratio of 1:2, and the late Roman days and middle ages (500 -1500AD) saw the use circular segmental arches- e.g. Ponte Vecchio in Florence (1300-1366AD) with a rise to span of 1:6.5 [2]. Although simple shapes to generate, these are not the most efficient compression-only geometries.

Figure 2.6: Panoramic view of St Peter's in Rome, shows barrel vaults in the transepts and the central dome. Source: Jonathan Garcla.

Significant developments were made to the arches during the Renaissance, owing much to the development in mathematics and the freedom to innovate. This is evident in the Pontypridd bridge by the Welsh master-bricklayer William Edwards, which- to put lightly- was a 10 year long practical building experiment taking three attempts to finally be built as a safely standing structure [2].

With the developments in mathematics, especially in geometry, and in mechanics, Renaissance brought about new forms for arch bridges; (i) three centred arch (ii) ellipse and (iii) inverted catenary. Ponte Santa Trinita (1569 AD) in Florence is the first evidence of a catenary being used to derive the shape of an arch, albeit the method making little sense with current day knowledge [2]. Surveys conducted in Sassanid Palaces (modern-day Iran) has shown indication of possible use of catenary in their shape profiles, but no written evidence exists [2].

Fleisch Bridge (1598 AD) in Nuremberg (Figure 2.8) shows how rapid these ideas travelled across the continent especially due to the trading partnerships between cities of Europe. Designs of the centering for this bridge show how much the builders understood the structural behaviour; the need for a stiffer centering on piles to take initial load so that there is time for the mortar to set, the step-by-step slow removal of centering so that the arch deforms gradually to take its final form, and a mortar capable of plastic deformation so tensile cracks on extrados at the impost (arch springing) are controlled [2].

Figure 2.7: Ponte Santa Trinita. Source: Structurae.net/ photographer: Karl Gotsch

Figure 2.8: Fleisch Bridge, Nuremberg. Source: Structurae.net/ photographer: Nicolas Janberg.

The progression of the tradition of building arches from Mesopotamian civilization to renaissance can be summarized in a timeline as shown in Figure 2.9. Although, the development of arches in European renaissance is heavily documented, it is not the only development of arches and domes that took place in the world at the time. Personal communications with an Iranian Architect and preservationist of historic buildings- Mostafa Aref Hagi-, revealed the rich tradition of ‘Karbandi’ which incorporates architecture with the understanding of compression only forms and geometry. These masterpieces of Persian architecture still stand in parts of Iran (see Figure 2.10). Unfortunately, the text books on the analysis and construction of these structures are only available in Persian.

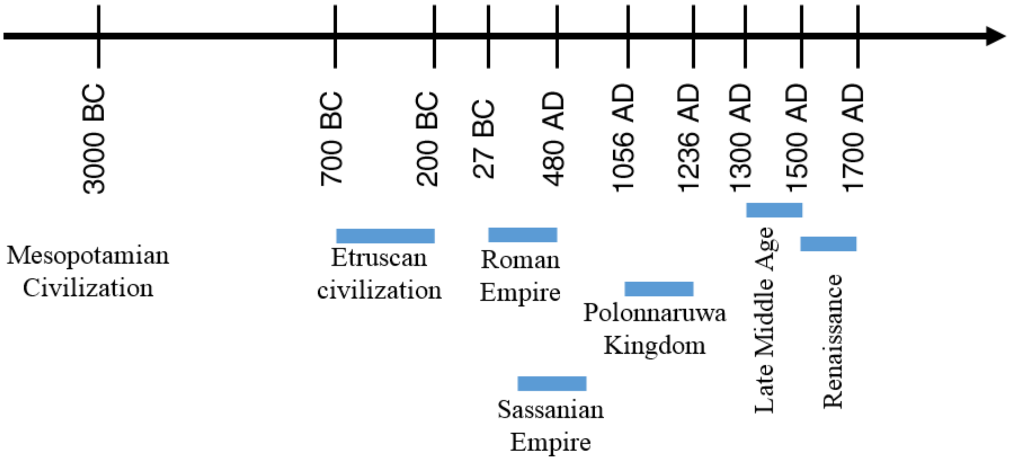

Figure 2.9: A historical timeline of practice and development of building arches.

Figure 2.10: A Karbandi structure in Zoltan Mir Ahmad – a traditional Persian bath- in Kashan, Iran. Image courtesy: Mostafa Aref Hagi.

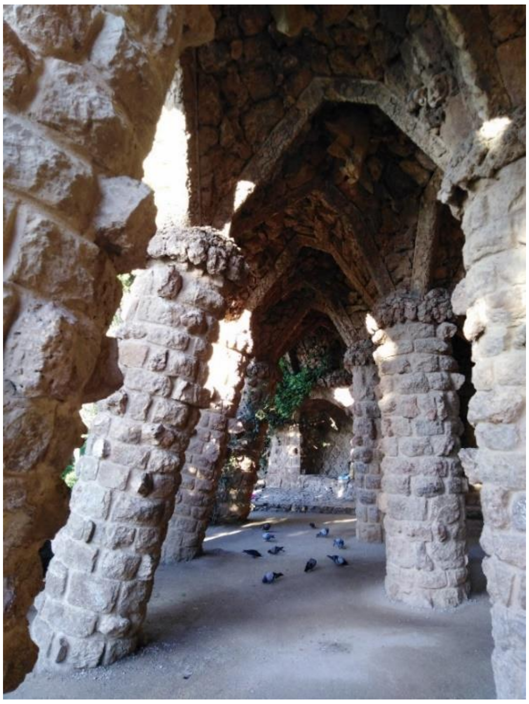

Figure 2.11: Columns supporting a viaduct at Park Guell, Barcelona.

At the turn of the 20th century Catalan modernisme gave a fresh crop of compression only forms. Although the innovation is founded on art and architecture the importance given to the forms and forces has left a collection of intriguing structures across Barcelona, designed by Architects lead by Antoni Gaudi and Lluís Domènech i Montaner.

Their structures are not limited to arches and domes but pays respect to the forms and forces. This is clear in the viaducts in Park Guell in Barcelona (see Figure 2.11) – the columns are built at an angle such that it would carry the thrust force from the structure above as axial compressions.

The more impressive structures of this era, which included form finding through hanging chain models (a physical manifestation of the line of thrust discussed in 2.2.3) include La Sagrada Familia (see Figure 2.12), Colonia Guell (see Figure 2.13), Casa Milla (see Figure 2.14). The Hospital de Sant Pau by Domènech i Montaner seems to include dome structures influenced by the Persian architecture mentioned earlier (see Figure 2.15).

Figure 2.12: Slender columns supporting the thrust of the domed roof and towers in La Sagrada Familia, Barcelona.

Figure 2.13: The compression only support structure of the Crypt at Colonia Guell.

Figure 2.14: The support structure for the roof terrace at the attic of Casa Milla, Barcelona.

Figure 2.15: Roof structures at Hospital Sant Pau in Barcelona, indicating influence from Persian Architectural technique of Karbandi.

With the advent of industrial revolution steel and concrete became the main construction materials, opening new possibilities in rising-up –shear cores and tube in tube systems - and spanning long – suspension bridges. Despite that engineer-builders – likes of Rafael Guastavino and Felix Candela – and Architect-Engineer innovators – likes of Heinz Isler and Frei Otto- kept alive the tradition of self-supporting shells, building iconic structures similar to timbrel vault ceiling in the Grand Central Terminal in New York (Figure 2.16) and the Manheim Multihalle. In Sri Lanka, the revival of concrete shell structures was due to the work and efforts of Dr A. N. S. Kulasinghe. Although his works were mostly limited to concrete shells, the innovative use of prestressing added a new dimension to the structural solution. His key works include hypar roof (following the work of Candela) in Ceylon Port Commission Car Park (1958), prestressed roof structures in Galle Harbour warehouse, Ceylon Port Commission Canteen (1958), Kulasinghe auditorium at NERD centre and hollow dagobas including Waraya Sambuddha Jayanthi Chaitya (1957-1985), Kalutara Bodhi Chaitya (1968-1973) and Mahaweli Maha Seya (1983-2016) [9].

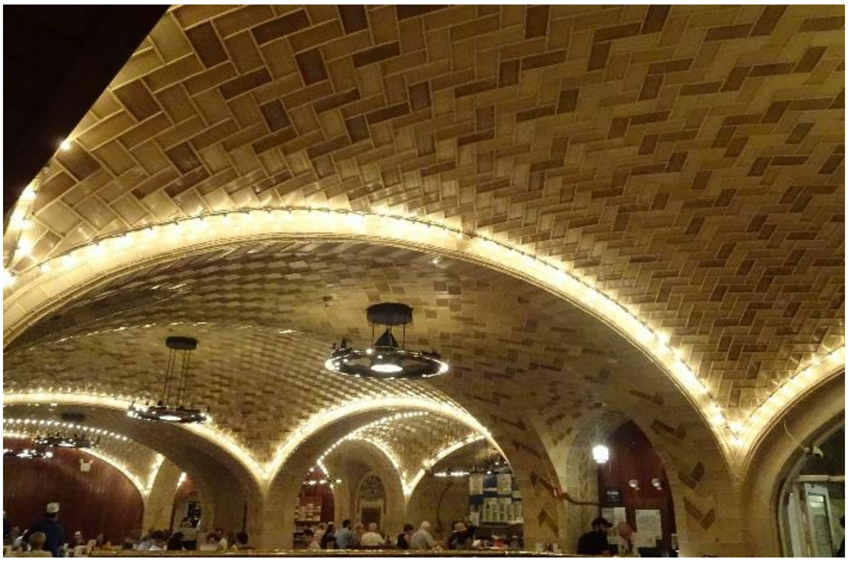

Figure 2.16: Guastavino vaulting in Grand Central Terminal, New York.

With the growing concern of sustainable construction compression-only forms are making a comeback in Europe - through the works of Block Research Group at ETH Zürich- and in Africa, sprouted from the vaults of Mapungubwe National Park visitor centre.

Among the work done by the Block Research Group at ETH is the Armadillo Vault (see Figure 2.17) which is a stone vault constructed using digital fabrications tools, Droneport prototype built using thin shell Catalan vaulting technology and ETH Pavilion for the 2015 Idea City Festival, which uses boards made of recycled tetra-packaging as the construction material.

The Institute of Lightweight Structures (ILEK) at the University of Stuttgart have also build prototype vaults over the years as part of their research efforts. Among those two key works are (i) the glass dome (see Figure 2.18) – which is proportionally thinner than an egg shell and (ii) smartShell (see Figure 2.19) - which uses active controls to resist variable loading conditions.

It is key to note that projects of both the above two institutes are aimed at showcasing the potential of compression only shells. The Auroville Earth Institute takes a more practical approach to their work and have an extensive array of earthen vault and dome constructions built for functional buildings. Their projects include various buildings in Auroville (see Figure 2.20), a conical vault in Sharanam, and Dhyana-lingam Dome in Coimbatore. Similar work are done in Africa by Light Earth Designs LLC, including the award winning Rwanda Cricket Stadium.

Figure 2.17: Armadillo Vault designed by Block Research Group. Source: DeZeen [10].

Figure 2.18: ILEK Glass Dome at University of Stuttgart.

Figure 2.19: SmartShell at Institute of Lightweight Structures (ILEK), University of Stuttgart.


Figure 2.20: Vaults and thin shells at Auroville Earth Institute (AVEI), Tamil Nadu India.

2.2. Development of the Theory of Arches

Before embarking on the journey through the history of arches it is worth identifying the two competing yet related ideas of 'loadbearing structure' and 'loadbearing system'. Throughout history there is a back and forth between these two ideas, but one cannot exist without due recognition to the other, as we would find out.

Based on the origins of the word, a bow (Latin *arcus*) would be a loadbearing structure as the loadbearing characteristic is achieved by the rigid structure. In terms of structural mechanics this would be an elastic arch with not negligible amount of bending work to achieve equilibrium and stability. On the other hand, a vault (Latin *voluta*) would be a loadbearing system where the loadbearing character is achieved by a collection of discrete units working together. This conceptual idea is in fact evident in the construction, and even in the final product; i.e. in Figure 2.21 the arch is a rigid mass assumed to act as homogenous unit whereas in Figure 2.2 individual building blocks are meant to act as loadbearing elements on their own. This difference is further visualized in the photo elastic experiments conducted by Bert Heinrich (1979) (see Figure 2.22).

Figure 2.21: Pont de la Liberation Bridge in France, constructed of unreinforced concrete. Source: Structurae.net/ Photographer: Jacques Mossot.

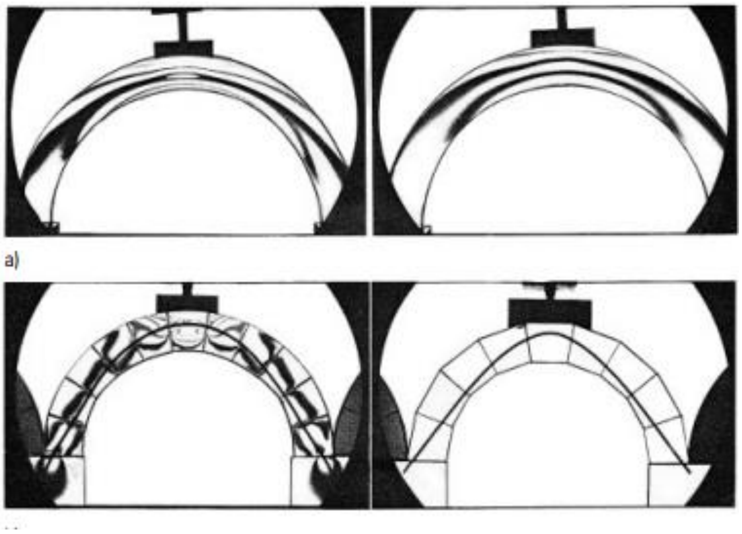

Figure 2.22: Photo elastic experiment carried out on a model subjected to a central point load: isochromatic lines of (a) monolithic arch model, and (b) masonry arch model. Source: Kurrer [2].

2.2.1. Wedge Theory for Masonry Arches

It is obvious that the early master builders used some methodology or theory in building those impressive arches; from Pantheon (126AD) to Hagia Sophia (537AD). This ‘non-scientific’ theory is based on proportions; arch thickness to span and buttress depth to span ratios. For an example, Gothic architecture of late middle ages gives depth of buttress as quarter of the span and renaissance architecture gives the same as half or a third of the span.

Da Vinci’s (1452-1519AD) model of masonry arch (Figure 2.23) is the traceable starting point of this development. This is the logical first step from the Etruscan arch with properly cut stone to a mathematical analysis. The model proposed satisfies the equilibrium condition for the loadbearing elements but infringes the transition condition, in that the friction at joints are not considered. But Da Vinci is fully aware that an arch gives a horizontal thrust at the springings and proposes experimental setups to measure the same [2].

Mathematical formulations of this model came about in late 17th century – early 18th century period. These wedge-based theories are based on the early understanding of mechanics as the sum of simple machines; lever, wheel and axle, inclined plane, wedge, pulley and the screw [2].

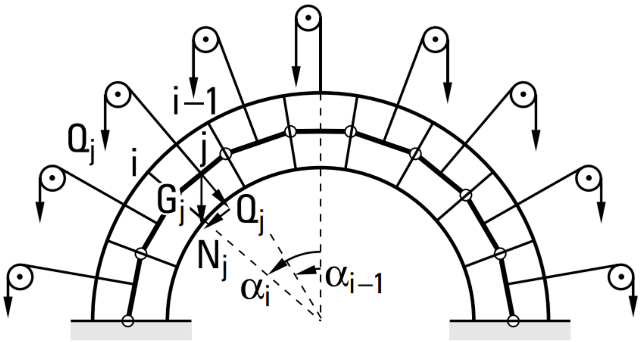

Figure 2.23: Da Vinci's wedge model for arches. Source: Kurrer [2].

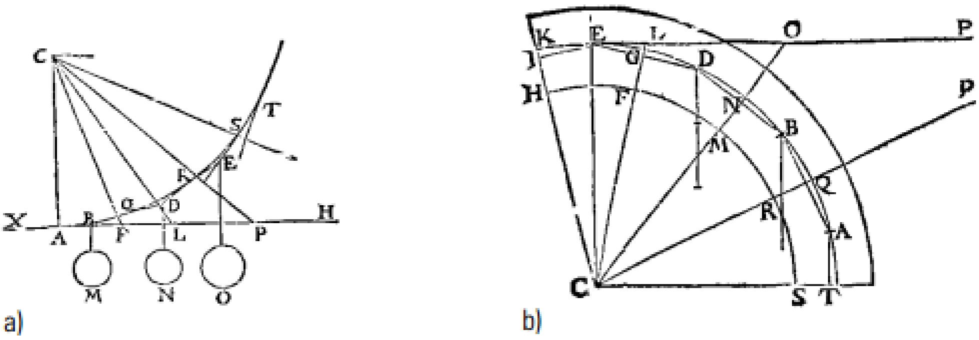

Figure 2.24: La Hire's first masonry arch model (a) funicular polygon, (b) wedge model from inversion. Source: Kurrer [2].

Philippe de La Hire (1730) presented a masonry arch theory which models individual blocks as weights attached to a funicular polygon (Figure 2.24). The funicular polygon is then inverted to form the wedge model. This inadvertently forms a part of the line of thrust problem and in terms of a wedge theory neglects the friction at joints.

Bernard Forest de Bélidor (1757) developed a wedge theory where he too prescribed weights of wedges and ignored friction at joints. He understood the existence of an unaccounted force and steadily increased the weight of voussoirs from keystone to the abutments to restore the equilibrium.

La Hire (1712) and Bélidor (1729) calculated the horizontal thrust on arches and hence the thickness of buttresses. Huerta (2006) notes that these values to be consistent with the traditional proportional rules. La Hire and Bélidor's theories were the universally accepted theory throughout the 18th Century and into the 19th Century. Also, it is of interest to note that the design of buttress was the main concern of the design. As it would be evident through limit analysis unacceptable movements of the buttress is the most likely condition for the collapse of an arch.

The classical theory of dry friction was established in 1700s but failed to add any improvement of significance to the arch theory. As such the loadbearing system view of the arch faced a dead-end. However, the wedge theory survived longer than it should have owing to the fact that arches were built using distinct blocks, as opposed to one single cohesive unit [2].

It is important to note here that the geometrical theories- from master masons to La Hire and Bélidor - are assumed to be correct for a structure of any size. However, Galileo Galilei (1638 AD) presented the square-cube law – 'load (mass) grows with the third power of linear dimension; the strength grows with the second power; hence a structure becomes weaker as it grows in size'. This essentially questions the premise of geometrical design. As we go on to observe through the idea of thrust line the master builders were correct in using geometrical design as stability, not strength, was the primary criterion for the design of masonry arches.

2.2.2. Collapse Mechanisms to Voussoir Rotation Theory

The understanding of collapse mechanisms paves the way for the next significant jump from the wedge theory of arches, and points to the ultimate load theory in the end. During the 18th century, many French and Italian scientist have conducted thought experiments on collapse mechanism and Danyzy (1732/1778) and Boistard (1810) are few of those to conduct small model tests on masonry arches.

Following the tradition of kinematic view of statics, Bernardino Baldi (1553-1617) presents a collapse mechanism for a semi-circular arch (Figure 2.25). Although his reasoning is far from enlightening, he notes three significant points about collapse mechanism, which have been commonly used since; (i) division of the arch into three equal parts, (ii) central part breaks along the middle, and (iii) the two rigid bodies created above rotate about the intrados.

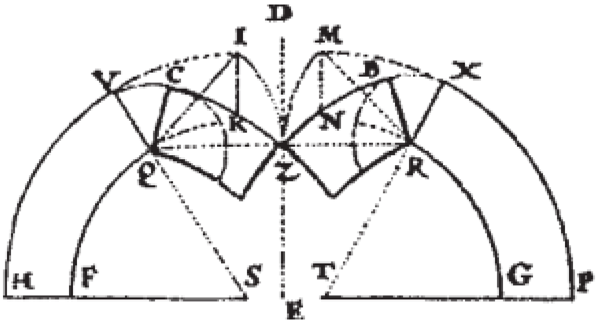

Figure 2.25: Collapse mechanism for semi-circular arches by Baldi. Source: Kurrer 2008 [2].

Few others to have made their contributions during this time are Honoré Fabri (1669) who simplified the line of thrust to two straight lines, Johann Esaias Silberschlag (1773) who used a three-pin system to calculate the horizontal thrust of segmental arches, and Derand (1643) who presented empirical rules for the thickness of abutments.

Pierre Couplet (1730) presented a limiting value for the thickness of the arch, based on a collapse mechanism with five hinge points. He deviated from the assumptions of La Hire, which was the common method of the day and assumed (i) infinite friction at joints, (ii) infinite compressive strength, and (iii) zero tensile strength. Heyman (1982) notes this as the historico-logical starting point of ultimate load theory and borrows these assumptions in reformulating the same in late 20th century.

Couplet's work is even more impressive when one compares his limiting arch thickness ($d_{u,Couplet} = 0.101R$) with those derived in modern times; Petit (1835) presents $d_{u,Petit} = 0.1078R$, Milankovitch (1907) presents $d_{u,Milankovitch} =$

$0.1075R$, both of which are confirmed by Ochsendorf (2002). The Danyzy (1732/1778) experiments too confirm Couplet's result. Karl-Eugen Kurrer (2008) notes that the significant leap of Couplet's theory is in fact the leap away from the traditional thinking of six simple machines and their combinations.

Charles Auguste Coulomb (1773) presented the voussoir rotation theory where he calculated limiting values for the horizontal thrust based on four cases; (i) downward and (ii) upward sliding of the central part of an arch divided to three equal parts, (iii) inward, and (iv) outward rotation of an arch with three hinges (Figure 2.26). The first two cases become irrelevant in practice as this would only occur with very thick arches. Further, he correctly locates the position of the joint of rupture, which La Hire (1712) did not locate and Bélidor (1729) arbitrarily fixed midway between the crown and springing [2].

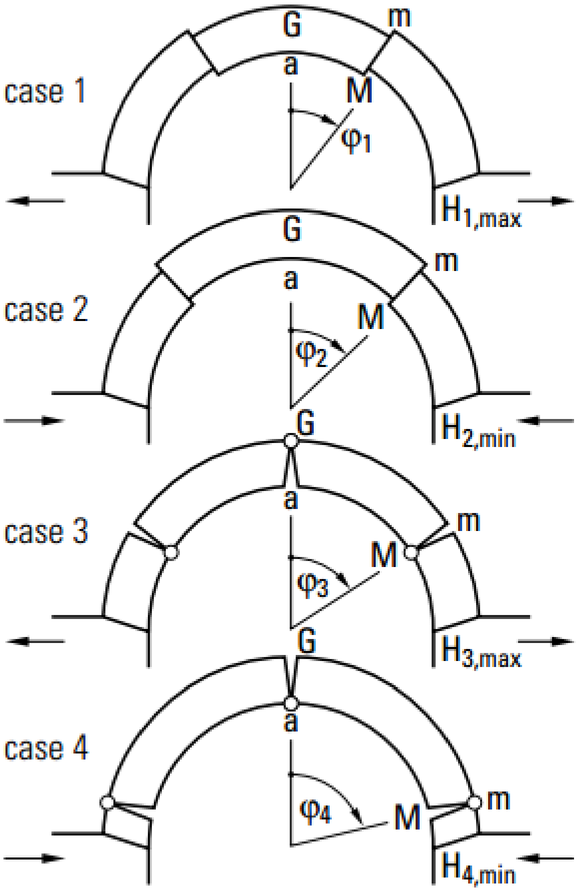

Figure 2.26: Voussoir rotation theory by Coulomb; horizontal thrust for (1) sliding downwards, (2) sliding upwards, (3) and (4) rotation about M. Source: Kurrer [2].

French Engineer Audoy (1820) rediscovered Coulomb's voussoir theory which was left unused for nearly a half a century. He introduced a factor of safety since the thicknesses derived from the theory were much too small. However, his formulae were too complicated for practical use.

Spanish Civil Engineer Joaquin Monasterio (1800-1810) for the first-time investigated collapse mechanisms of asymmetrical masonry arches of varying thickness and brought the mathematical analysis of collapse mechanisms of arches to a close.

This collapse-based thinking does consider the arch as distinct rigid bodies but is fundamentally different from wedge theories in that the separation is based on true crack patterns. As such it is an emulation of the true behaviour of the arch as one load bearing structure, and all the subsequent developments view the arch as one loadbearing structure, as opposed to the loadbearing system view of wedge theory.

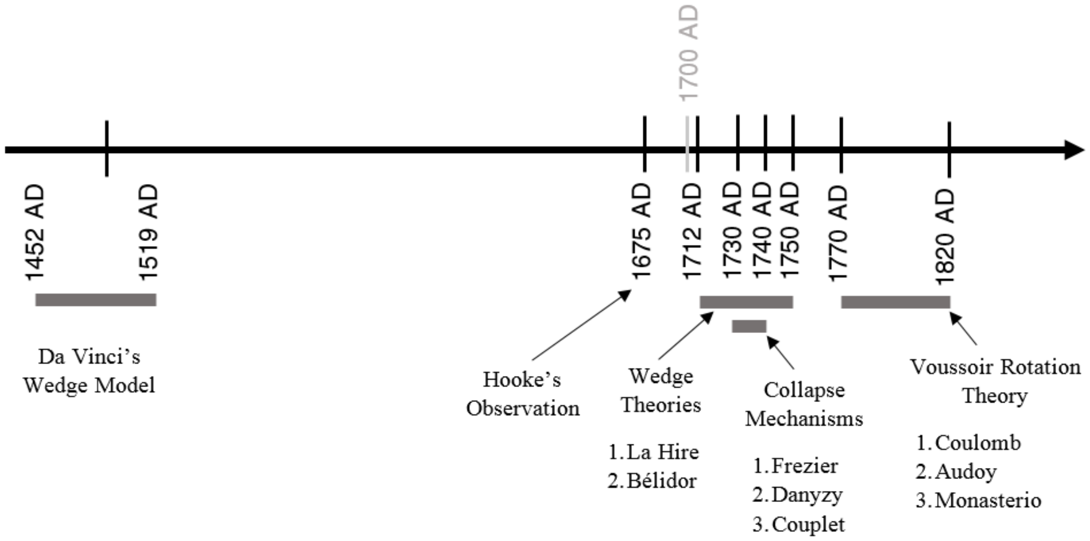

Figure 2.27: A historical timeline of the development of the theory of arches; from wedge theories to voussoir rotation theories.

2.2.3. Line of Thrust[1]

As evident from the previous discussion, the idea of a line of thrust was discussed and used on and off during the previous development stages of the arch theories (see Figure 2.27). Line of thrust is understood as the locus containing all the points where the thrust at every joint intersects the plane of joint.

---

[1] May interchangeably be referred to as thrustline.

The idea of a line of thrust comes from Robert Hooke (1675) whose observation is unavoidable in any discussion relating to the line of thrust; “As hangs the flexible line, so but inverted will stand the rigid arch”. This line of thought following the idea of line of thrust culminated in Heyman’s safe theorem, which is widely accepted today as the basis for assessment of masonry arches, vaults and domes (see Figure 2.28).

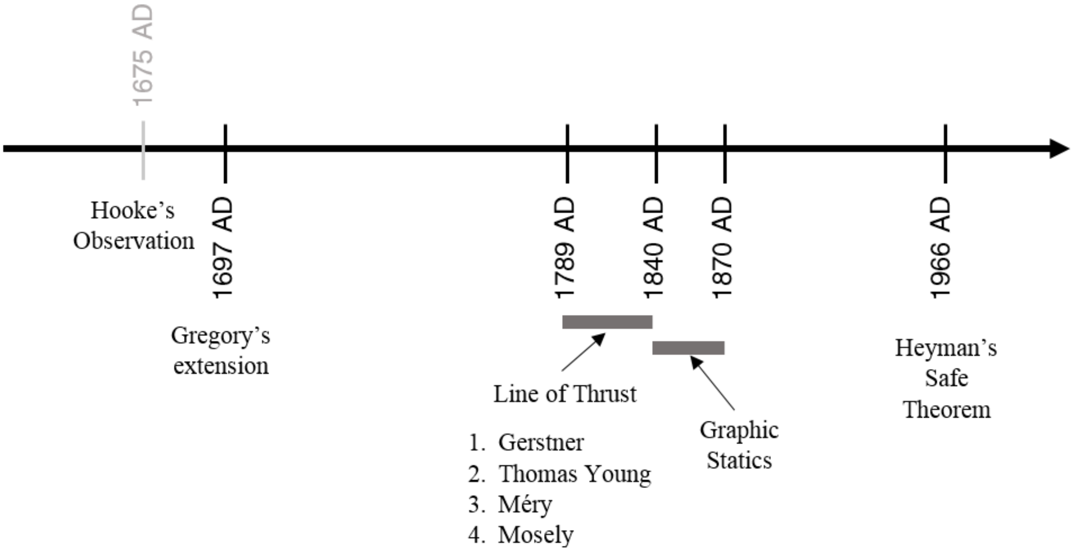

Figure 2.28: A historical timeline of the development and evolution of the idea of thrust line.

English mathematician David Gregory (1697) found the mathematical expression of the catenary and restated the Hook’s observation thus: “none but the catenaria is the figure of a true legitimate arch… And when an arch of any other figure is supported, it is because in its thickness some catenaria is included”. It is important to note that this simple restatement is significant in that it deviates from Robert Hooke’s claim of arch shape being a catenary to an arch of any shape containing some catenary.

Subsequent applications and study of the thrust line include Jakob Bernoulli’s (1704) definition of the shape of a thin catenary arch and William Emerson (1754) and Charles Hutton’s (1772) definition of catenary arches for specific loading cases.

The most significant application of the line of thrust at the time was made by Poleni (1748) in his analysis of the dome of the St. Peter’s in Rome (see Figure 2.29). His work is based on Gregory and suffers from the shortcomings in the abstraction of the loadbearing structure to a loadbearing system synthesised in the form of addition without due regards to the interaction between individual elements.

Franz Joseph Ritter von Gerstner (1789) finally filled this gap by constructing the catenary arch by infinitesimalising a bar in equilibrium under its self-weight. Afterwards Gerstner (1831) formalised the study of the line of thrust by formulating the three prime tasks of line of thrust.

1. Determine the line of thrust for a given loading case.
2. Determine the loading case for a given arch centre-of –gravity axis such that said axis coincides with the line of thrust.
3. Take into account the line of thrust for a given loading case and masonry arch centre-of-gravity axis.

If one looks at the development of the line of thrust up to this point, it is possible to recognize that the first two prime tasks were handled to some degree in studies predating Gerstner.

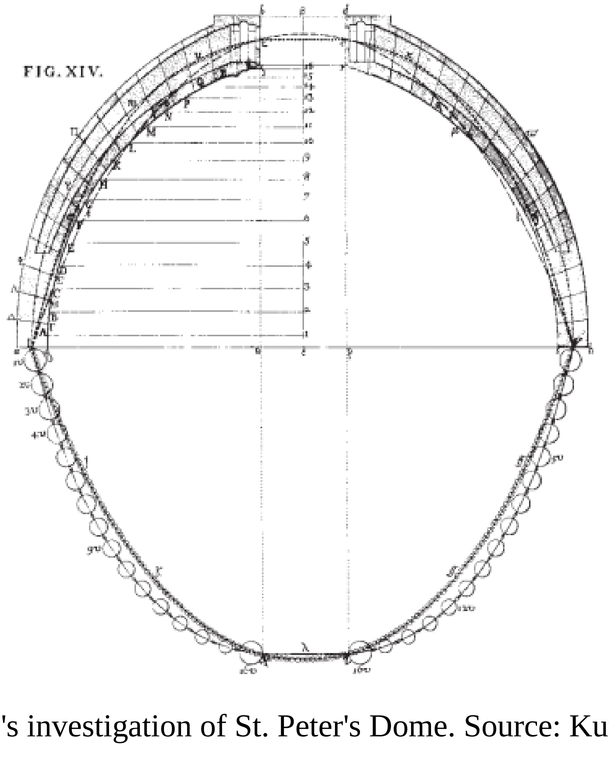

Figure 2.29: Poleni's investigation of St. Peter's Dome. Source: Kurrer [2].

While Germans credit Gerstner for the line of thrust concept, French and English literature attributes the line of thrust concept to Méry (1840) and Mosely (1835), both of whom merged the thrust line and the collapse mechanisms [2].

However, Thomas Young (1817) was the first person to present a complete thrustline arch theory [11], although it did not have much impact during its day and was only recently rediscovered by Huerta (2001). He presented a general mathematical expression of the line of thrust for different loads. Huerta [3] notes that Young's analysis of Telford's bridge design – which none of the leading structural engineers of the day were able to verify- was in fact completely correct, with the implicit use of a geometrical factor of safety (Figure 2.30). But, unfortunately, his style of writing made it difficult for others-at the time- to fully comprehend his ideas and hence never became general practice.

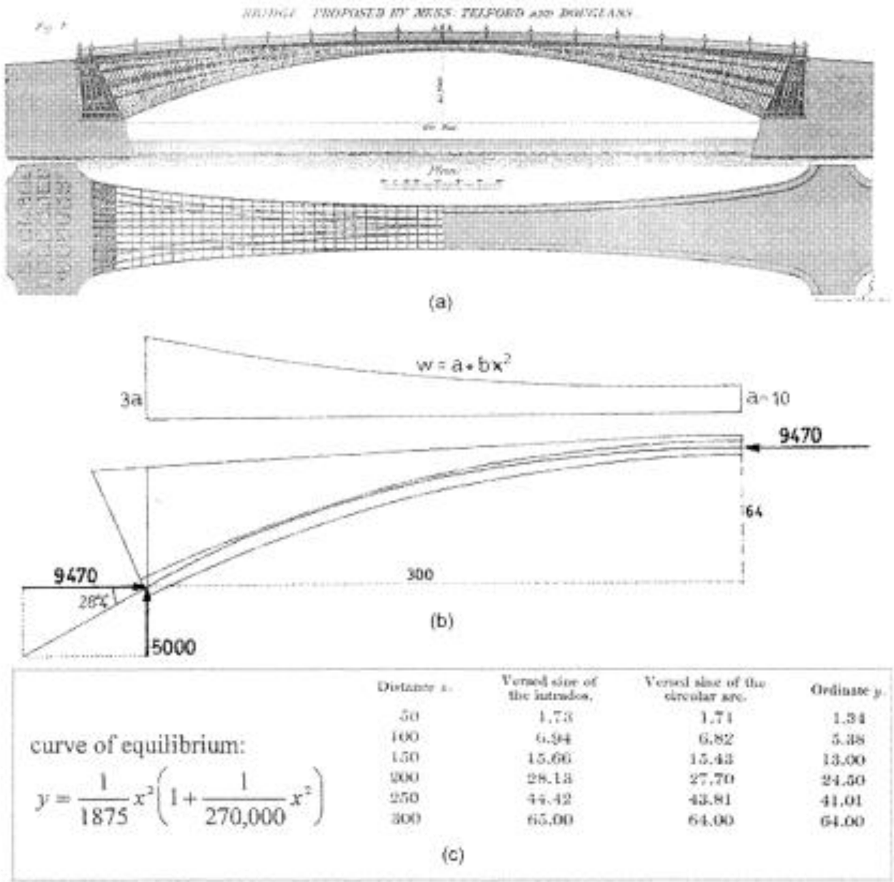

curve of equilibrium:

$$y = \frac{1}{1875}x^2\left(1 + \frac{1}{270,000}x^2\right)$$

Distance x.	Versed sine of the intrados.	Versed sine of the circular arc.	Ordinate y.
50	1.73	1.71	1.34
100	6.94	6.82	5.38
150	15.66	15.43	13.00
200	28.13	27.70	24.50
250	44.42	43.81	41.01
300	65.00	64.00	64.00

Figure 2.30: Young's (1817) analysis of Telford's design for an arch birdge of 183 m (a) original design presented by Telford (b) the equation of the thrust lines and the ordinates calculated by Young (1817) (c) Young's computations. Source: [11].

The next logical step in the thrustline theory was to handle the third prime task presented by Gerstner; the form of the true line of thrust in the service condition. Mosely (1843) presented a principle towards this end; "of all statically possible force systems in equilibrium, the one that prevails is the one in which the resistance is minimal". He further distinguished between the line of resistance (i.e. line of thrust) and the line of pressure (Figure 2.31), where line of resistance needs to be contained within the arch section and line of pressure is not constrained. Line of resistance is the path connecting the points where the thrust and the plane of joint intersects. In contrast, line of pressure is the envelope of thrust vectors at joint plane. Mosely claims the true thrust line of a semi-circular arch to pass through the intrados at springing and extrados at the crown. This merges the thrust line with the voussoir rotation theory, as what considered here is essentially a three hinged arch [2].

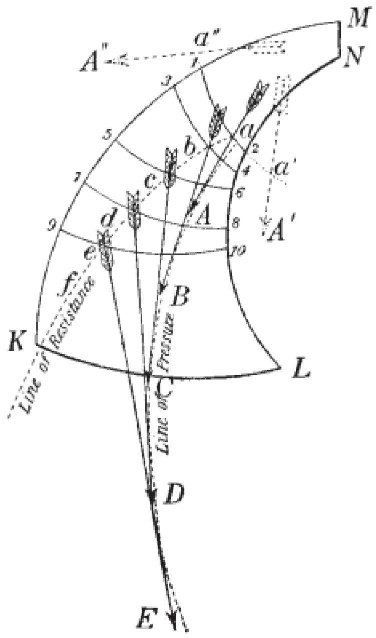

Figure 2.31: Moseley's distinction between line of thrust (line of resistance) and the direction of the pressure (line of pressure) in masonry arches. Source: [2]

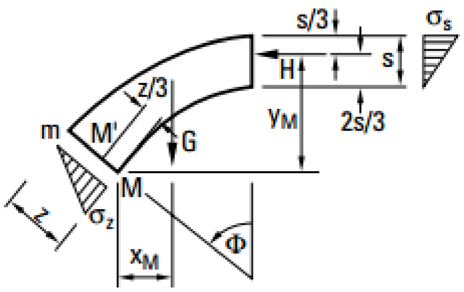

Figure 2.32: Stress analysis in masonry arches by Navier. Source: [2].

Both line of thrust and voussoir rotation theories are based purely on equilibrium and does not consider the material behaviour. Alfred Durand-Claye (1867) was the first to consider elements of elastic theory along with the traditional voussoir rotation theory.

Earlier in 1826, Navier has established an arch theory based on linear elastic theory (see Figure 2.32). He has devised general equations for masonry arches, but rarely can one find exact solutions to those. As such, Petit (1835) and Michon (1848) have computed tables to read out horizontal thrust and abutment thickness for masonry arches. Poncelet (1835) has devised a laborious but still efficient graphical method to solve Navier's theory of elastic arch

This search for the true line of thrust- through elastic theory or otherwise- was faced with much resistance as this endeavour seems to be purely academical, and no advantage in the progression of the engineering knowledge [2]; do we need to spend time to find the true line of thrust? A prime example is Bandhauer's (1831) alternative solution to elastic theory via an assumed stress distribution which gives stresses comparable to Navier's elastic theory (Figure 2.33).

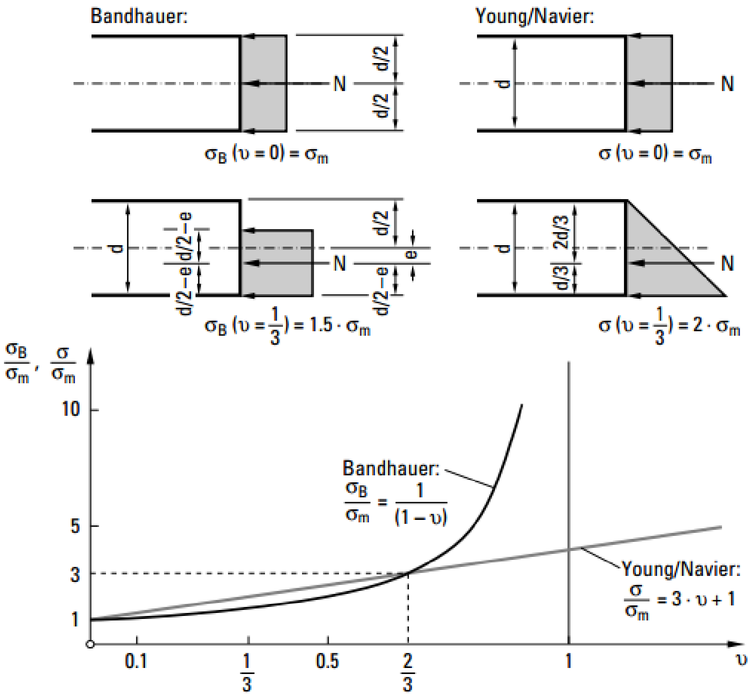

Figure 2.33: Stresses at the extreme fibres in the masonry arch cross-section according to Bandhauer and Young/Navier. Source: [2].

2.2.4. Elastic Theory

Ardant (1847), Bresse (1848) and Saavedra (1860) are evidence of the use of elastic theory for arches made of timber, iron and masonry respectively. Rankine's (1858) middle third rule for arches can be seen as an incorporation of the elastic theory to thrust line. Koblenz Bridge by Hermann Sternberg (1864) and Ponte Mosca in Turin by Castigliano (1879) are two cases of using the elastic theory to design and analyse a bridge [2].

Following Navier (1826), there were many developments associated with elastic theory in late 19th century. This include both theoretical exercises as well as practical usage of elastic theory in bridge design.

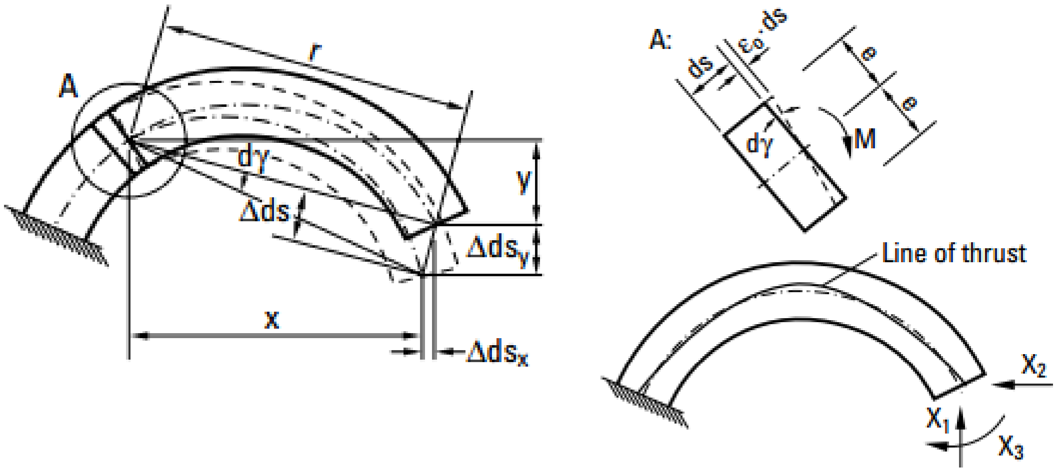

Figure 2.34: Winkler's determination of the position of the line of thrust in masonry arch using elastic theory. Source: [2].

A relatively autonomous elastic arch theory was developed by Weyrauch (1879) and this is significant for its departure from the loadbearing system analysis. Winkler (1879) considers an ideal state of the arch (i.e. rigid abutments, evenly and completely cured joints, etc.,) and incorporates elastic conditions to that and employed a minimization to find the position of the "correct line of thrust" for the "ideal arch" (Figure 2.34). This requirement of an ideal state is due to the deficiency in elastic analysis to capture the behaviour of a disrupted arch (i.e. abutments yielded, and hinges formed).

Among the critics of the elastic analysis were Heinrich Hasse (1982) who noted the elastic theory as “more laborious, more complicated and more unacceptable to practice than before” and George Fillmore Swain (1927) who noted the difference between the ideal and disrupted state of the voussoir arch and expressed that a complex solution does not necessarily mean a better solution.

This uncertainty on whether we need to know the true line of thrust led to a look back at pre-elastic masonry arch theories to reformulate the thrust line theory to a practical theory of arches. This ultimately resulted in the Heyman’s ultimate load theory for arches.

2.2.5. Graphic Statics

Graphic statics was a tool developed to aid engineers and it is a geometrical implementation of the mathematical theories developed at the time. This was a useful tool in the days before computers and on the other hand can be seen as the engineering science replacement for the rule of proportion of the classical methods.

Funicular polygon and the polygon of forces presented by Pierre Varignon (published posthumously in 1725) lays the foundation of the field of graphic statics (Figure 2.35). But not until *Die graphische Statik* by Karl Culmann in 1866 was a formal field of study formed.

Culmann (1864/1866) was the pioneer of graphic statics and graphical analysis and made it a formal and organized tool for engineers. Culmann in his publications presented a structural relationship between the funicular polygon and the polygon of forces through projection geometry, which was introduced by Jean-Victor Poncelet (1822).

The idea of reciprocal figures – i.e. interchangeability of funicular polygon and polygon of forces – too was presented by Culmann in 1864 (Figure 2.36). Working independently, James Clerk Maxwell also presented the same duality in 1864 and formed a formal theory of reciprocal figures through publications in 1867 and 1870 [2].

Rankine (1858) used funicular polygons to investigate statically determinate trusses and this solution correspond to the second prime task of thrustline theory. Cremona (1872) generalized the Maxwell theory for the case of plane frameworks. His procedural approach to the relevant diagrams requires no knowledge on projective geometry from the user.

Robert Henry Bow (1873) presented a catalogue of dual polygons of forces for truss frameworks, essentially making Cremona's procedural approach obsolete. However, graphic statics remained useful in the analysis and assessment of masonry vaults and domes.

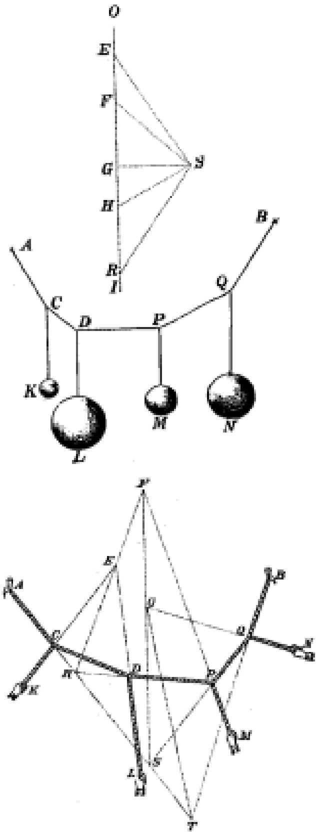

Figure 2.35: Funicular polygon and polygon of forces after Varignon. Source: [2].

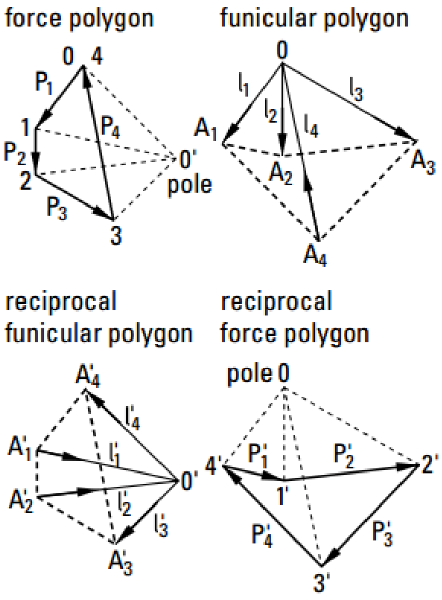

Figure 2.36: Duality of the funicular polygon and polygon of forces for plane force systems as presented by Culmann. Source: [2].

By the end of 19th century graphic analysis has been put to its full use, to determine both force and displacement condition (although not in masonry structures), without any trace of its foundation in projective geometry [2]. No significant advances were made in the field until a renewed interest in the subject in early 21st century – i.e. the current day.

2.2.6. Ultimate Load Theory

Theorems of limit analysis and the fundamental theorems were originally presented for reinforced concrete (Gvozdev 1936, translated 1960) and structural steelwork. First suggestion for its use in the analysis of voussoir arches was by Drucker (1953). However, Heyman (1966) was the first to provide a rigorous explanation of the applicability of ultimate load theory for masonry loadbearing structures in general.

Heyman borrowed Couplet’s assumptions (see Section 2.2.2), which are conservative or reasonable assumptions which can be checked. The first is the infinite strength of masonry, which is reasonable as it is found that the stress levels in masonry structures are generally an order - or two – of magnitude below crushing strength. The assumption of zero tensile strength is conservative as masonry has some tensile strength (≈ 10% crushing strength). The final assumption of infinite friction is reasonable considering the high friction coefficient of masonry (0.6 - 0.7). Both strength and the friction criteria can be checked at the end of the design.

Heymans safe theorem states that “if a set of internal forces in a masonry structure can be found that equilibrate the external loads, and which lie everywhere within the masonry, then the structure is safe – safe in the sense that it cannot collapse under those loads.”

This can be explained considering the behaviour of a masonry arch. Once the centering of a masonry arch is struck off the arch exerts a horizontal thrust on the abutments and the abutments yield. Cracks appear on intrados and extrados of the arch to permit this movement (Figure 2.37). It is important to note that these cracks are not dangerous and in fact these are essential to how the loadbearing structure respond to changes in the boundary conditions. These cracks behave as hinges and once three such hinges are formed the arch is statically determinate. However, formation of one more hinge will turn the arch into a kinematically permissible mechanism and will no longer be able to carry loads (Figure 2.38). This loading condition under which the fourth hinge is almost formed is the upper bound solution. The condition with three hinges is a lower bound solution: i.e. a safe solution.

The above mentioned crack pattern - where there are at least three hinges - fully defines the position of the line of thrust as it must pass through the hinge location- i.e. if the line of thrust touches the intrados or the extrados, a hinge forms at that point (see Figure 2.37). An uncracked arch of sufficient thickness can contain infinitely many lines of thrusts for a given loading condition, and any one of those is a valid equilibrium solution. However, one can find a 'limit arch' which contains only one possible line of thrust- i.e. the three hinged condition. The thickness of this arch would be the 'limit thickness'; for a semi-circular arch this would be 1/18 of the span. Following this line of argument, Heyman (1969) proposes the concept of a geometrical safety factor for arches– arch thickness to limit thickness ratio- and suggests a value of 2 under the most unfavourable loading condition. With this factor of safety, Heyman assures that the structure will remain safe for any small, future movements of the abutment.

The above completes the argument for an Engineer not needing to know the true line of thrust, as long as one can find a possible equilibrium solution. This is indeed the advantage of the limit analysis over elastic analysis, which can still give unsafe results.

It should be now clear that this approach is based on stability criterion and not the strength, hence safety of a masonry structure is a matter of geometry. Huerta (2006) shows that an arch of medium sandstone (density 20 kN/m^2 and crushing strength 20N/mm^2) will require a span of 640m to have both the strength and stability criterion reached at the same time, without a factor of safety. This is coming back to the validity of a proportional rule for masonry arches. None of the known -built or planned- masonry bridges come close to the limit of 640 m found above; the stone arch bridge of Fong-Huan in China (1972) spans 120m, the bridge over Adda in Trezzo (1370-1377) spans 72m, and Da Vinci's proposed one arch bridge over the Golden Horn in Istanbul (1500AD) spans 240m.

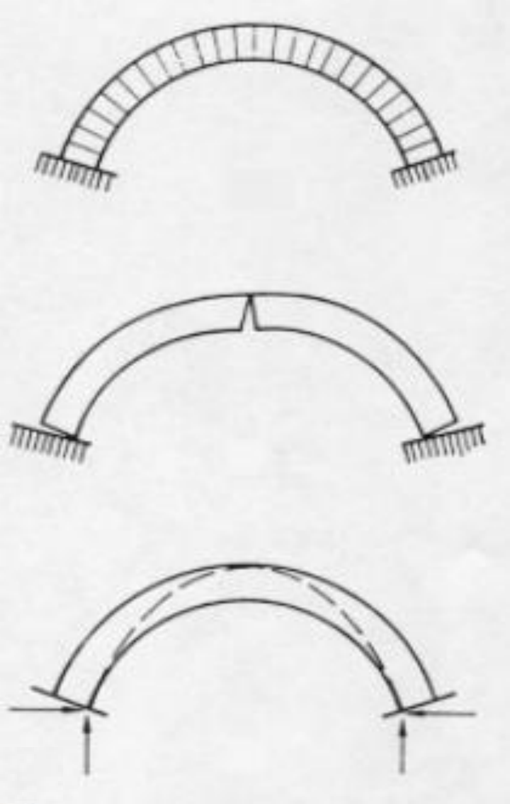

Figure 2.37: Crack formation in a masonry arch after striking the centering. Source: [2].

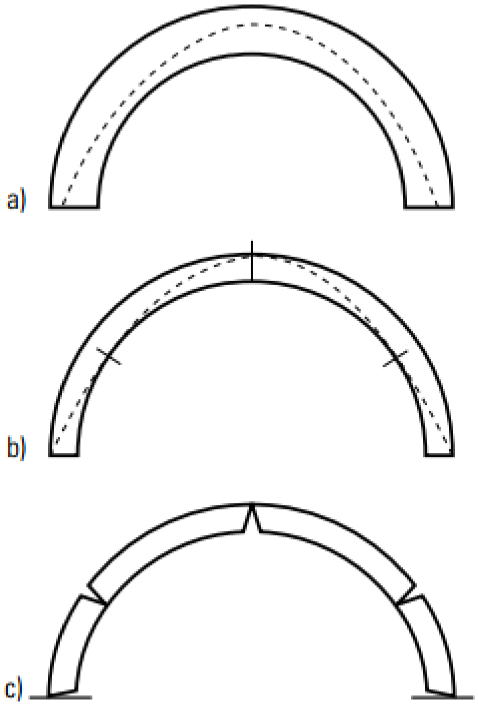

Figure 2.38: Failure of semi-circular arch subjected to a point load. Source: [2].

2.2.7. Finite Element Method (FEM) and Discrete Element Method

With the availability of the computational power of computers and complexity of structures, it was only a matter of time that arches too fold into the realm of FEM; Mark (1982) was the first to make an elastic analysis of a Gothic building.

Although one can carry out a purely academic or a preliminary study (Figure 2.39) of a masonry arch considering Finite Element Analysis under linear-elastic condition, there are many pitfalls in using it for the design process; e.g. no-tension and orthotropic material, presence of cracks, yielding of abutments, etc,.

Block et al. [12] clearly shows the inability of a Finite Element (FE) analysis to differentiate between a stable and an unstable arch geometries (see Figure 2.40). While FE analysis cannot say anything conclusive about the stability of the arch, limit state can clearly indicate instability of the form through the presentation of a line of thrust. However, with appropriate detailed input on material behaviours and support conditions, one can get more detailed information from FE analysis on problems such as crack genesis in a masonry arch [12].

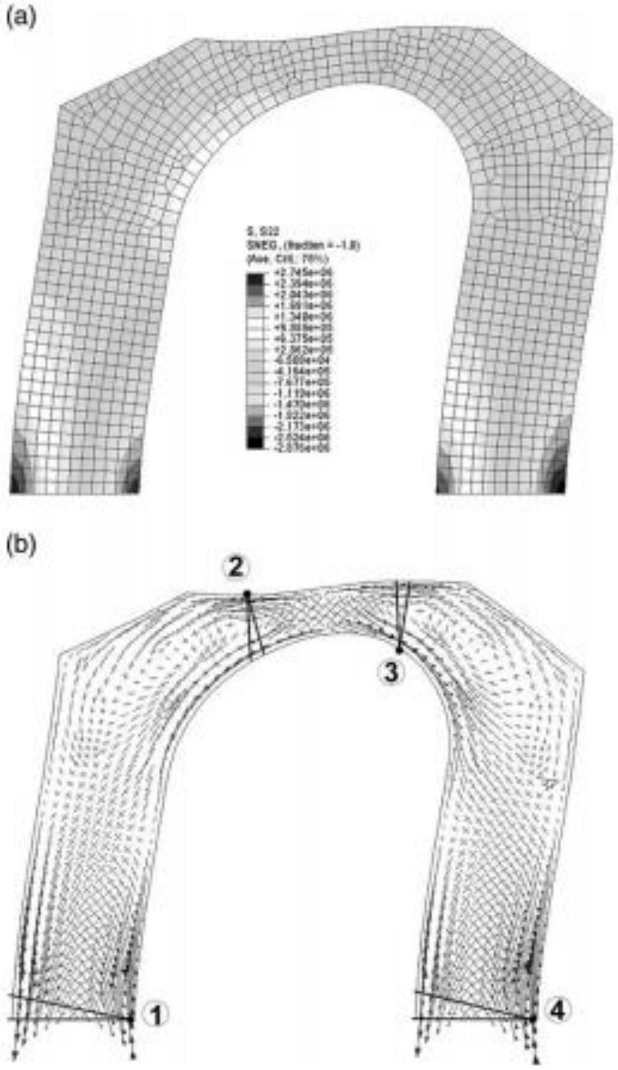

Figure 2.39: Finite Element Analysis to identify possible failure mechanisms: (a) vertical stresses (b) principal stresses with possible hinge positions. Source: [13].

Non-linear FEM analysis of masonry arches and domes can be classified under two categories; (i) macro modelling, and (ii) micro modelling. Macro modelling uses a material model based on average stresses and strains and is extensively used to analyse seismic response of historical structures. Micro modelling uses individual masonry units as the element and hence is the more accurate tool available but demands a lot of computational effort (see Figure 2.41). An intermediate homogenization solution can be realized by first analysing a micro model to set up the unit element of a macro model. However, Roca et al. [14] note the difficulty of using non-linear FEM for the analysis of masonry domes and vaults due to its curved two-dimensional spatial character.

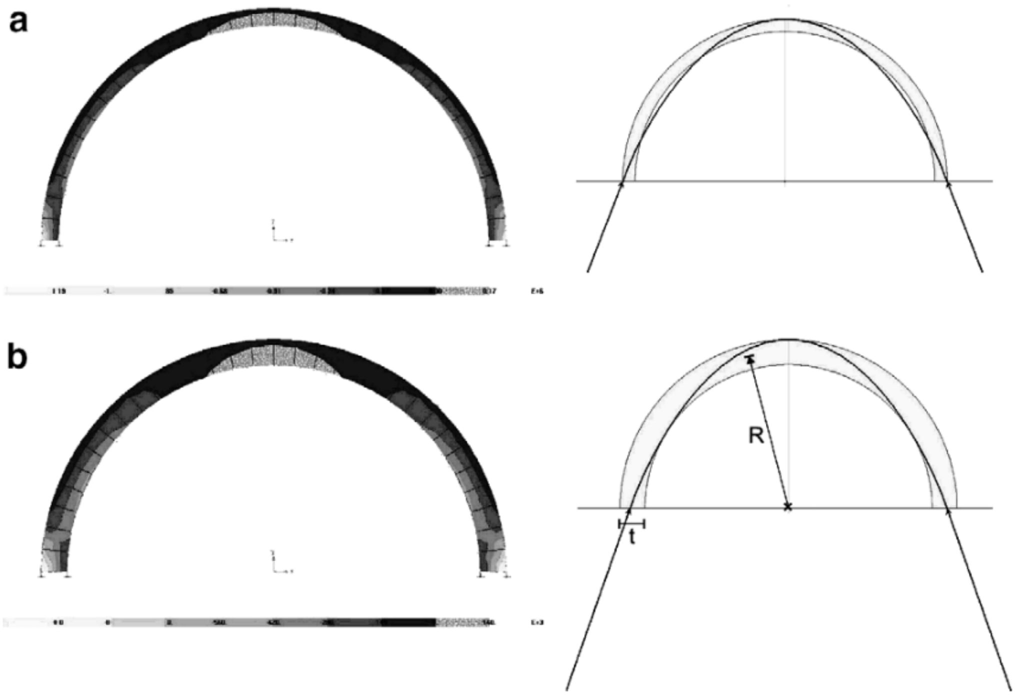

Figure 2.40: Comparison of elastic finite analysis against limit state analysis (i.e. thrustline analysis) for (a) an unstable and (b) a stable arch. Source: Block et al. [12].

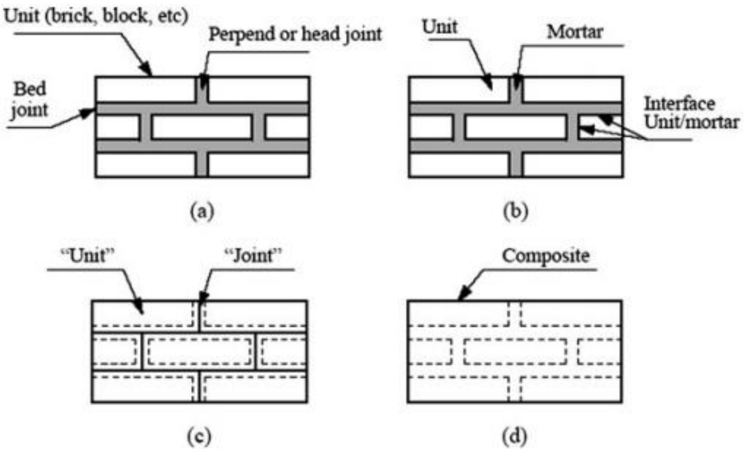

Figure 2.41: Modelling strategies for masonry structures; masonry sample (a) detailed, (b) simplified, (c) micro-modelling and (d) macro-modelling. Source: [14].

Discrete Element Method (DEM) which models material as an assemblage of distinct blocks was first introduced by Cundall and Hart (1971) and was first applied to the assessment of masonry structures by Pagnoni (1994). There are three types of DEM formulations, (i) Distinct element models, (ii) Discrete finite element methods, and (iii) discontinuous deformation analysis (DDA). Distinct element models are direct derivations from Cundall and Hart (1971) and in contrast discrete –FE models define contacts and discontinuities as bands of finite thickness. Mamaghani et al. (1999) was the first to implement discrete FEM on masonry structures (Figure 2.42). Discontinuous deformation analysis, first applied for masonry structures by Ma et al. (1996) has natural applications on regularly shaped masonry structures, but its application on complex structures is a controversial topic [14].

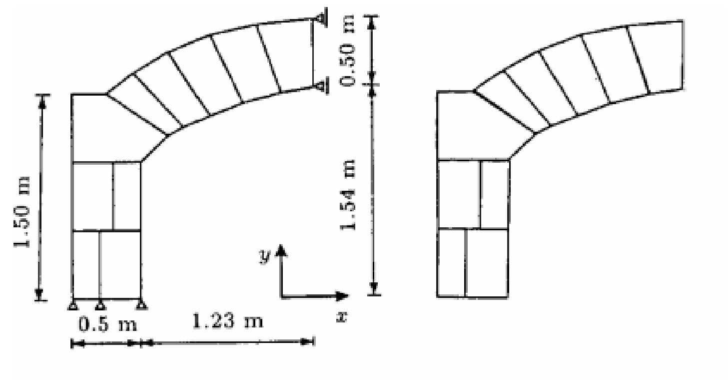

Initial configuration

Iteration no. 24

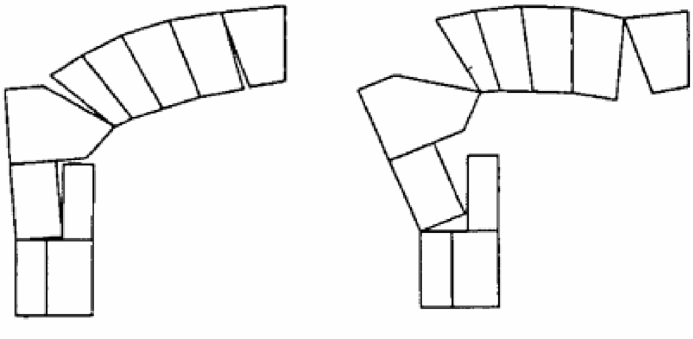

Iteration no. 27

Iteration no. 30

Figure 2.42: Failure mode of a masonry arch. Source: Mamaghani et. al. [15].

2.3. A Brief History of the Analysis of Domes and Vaults

Domes and vaults can be viewed as the three-dimensional manifestation of the arch. Although arches and barrel vaults are three dimensional structures, they have a uniform cross-section along one direction and the equilibrium is satisfied by satisfying equilibrium in that cross-section – a two-dimensional form.

As Huerta [3] notes the development of the theory of spatial masonry vaults is only roughly known. The first instance of a scientific basis being employed is the dome of St. Paul’s Cathedral in London (1675) where Christopher Wren was advised by Robert Hooke to use hanging chain models. In 1740s a stability analysis of St Peter in Rome was conducted by a group of experts which included Poleni, who followed the hanging chain approach of Hooke and Gregory [11] [2].

The first memoir dedicated to dome design was by Bouguer (1734) who studied stable forms for domes, ignoring friction – as was the case for arches of the day- but considering hoop forces [11]. Frézier (1737-1739) explicitly used slicing technique to decompose the vault to a series of arches and calculated the thrusts from the corresponding barrel vaults. Bosut (1774), Salimbeni (1787), Bérard (1810), Persy (1834), Kobell (1855) and Scheffler (1857) conducted purely mathematical research into domes, but these approaches were never used in practice [2].

However, graphic statics found better success in its application to spatial domes and vaults. Wittmann (1879) was the first to present an accurate graphical analysis for a three-dimensional masonry construction (Figure 2.43). Karl Mohrmann (1890) applied the strip method to analyse ribbed Gothic vaults. He imagined the thrust to follow the same path as a ball rolling on the extrados would. Mohrmann simplified the solution by presenting the thrust in a tabular format, considering material, load and geometrical proportions as the variables. Henry Turner Eddy (1878) presented a graphical method to determine the membrane stress condition of domes, which was later used for masonry domes by Föppl (1881).

From the early 20th century the analysis of spatial masonry forms was in view of assessing the safety of historical masonry structures. A renewed interest of design exploration came about in the late 20th century, mainly through a line of students of Professor Heyman at University of Cambridge.

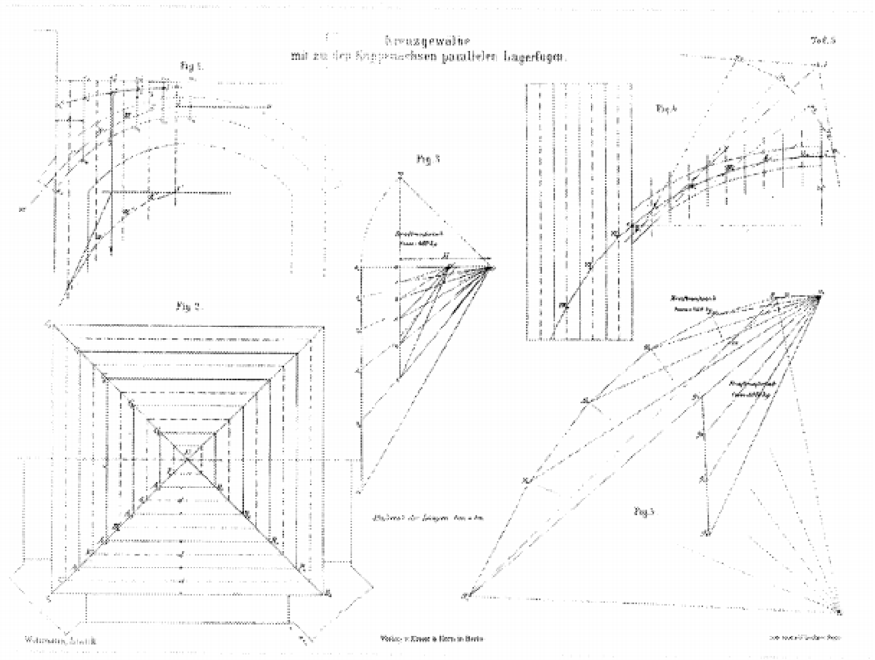

Figure 2.43: First correct graphical equilibrium analysis of a groin vault by Wittmann 1879. Source: [11].

Heyman (1977) applied his safe theorem to masonry vaults, finding a membrane solution which fits within the vault surface. In a similar line of thought, O'Dwyer (1991, 1999) proposed an equilibrium approach based on force networks, which was to be fully contained within the vault surfaces (Figure 2.44). However, the indeterminacy of the networks limits the application of this method. The current developments in this line of thought are further discussed in the Section 2.4.

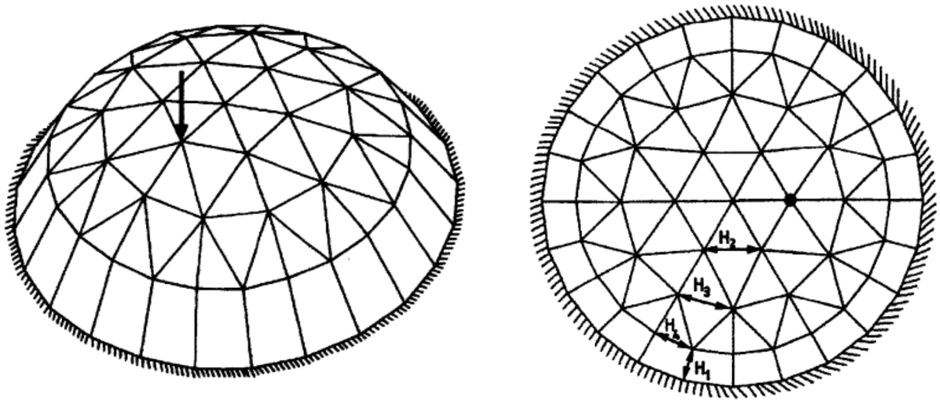

(a) (b)

Figure 2.44: (a) Optimized three-dimensional shape of the force network for a masonry dome and (b) the corresponding force network mesh. Source: [16].

With the advent of computers, many of the early techniques which were tedious or complex to handle manually were re-implemented. Smars (2000) developed a software to implement a pseudo-3D analysis. Even there handling complex geometries become complicated and the analysis would be limited to cross vaults and groin vaults.

Livesly (1978/1992) discretized the three-dimensional structure to an assembly of blocks and conducted a rigorous analysis of the loadbearing system. Whiting et al. (2009) expanded this to explore the limits of stability (Figure 2.45).

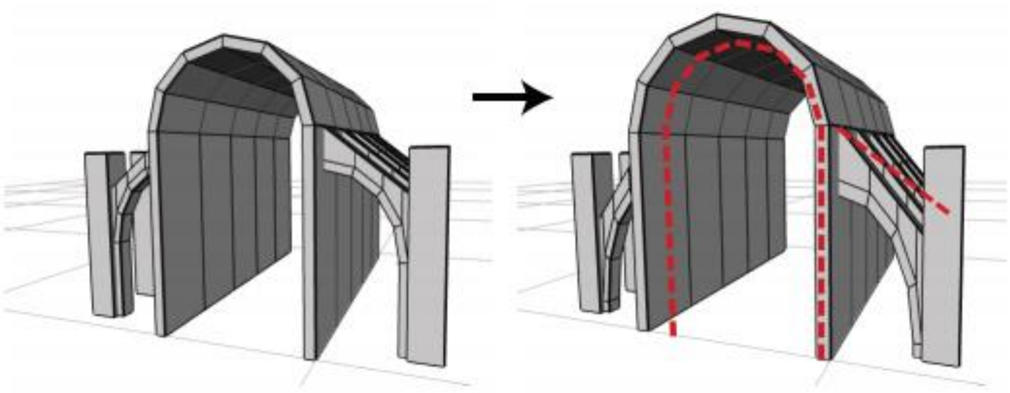

Figure 2.45: Interactive editing of parameters (e.g. span of the barrel vault) and real time stability analysis (e.g. angle of flying buttress required) of masonry structures. Source: [17].

Also there was a renewed interest in using physical models, pioneered by people like Antonio Gaudi- for the crypt of the church of Colonia Güell and La Sagrada Familia (Figure 2.47)-, Heinz Isler – tennis courts at Solothurn (Figure 47) - and Frei Otto– many concrete shells across Germany. These methods too were implemented in software using dynamic relaxation (Barnes 1999) and particle spring methodologies.

Figure 2.46: Heinz Isler's (a) physical model and (b) the as built tennis court roof at Solothurn, Switzerland.

(a) (b)

Figure 2.47: Physical hanging chain model of La Sagrada Familia.

2.3.1. Shells as a Continuum.

Shells are structures defined by curved surfaces and are thin in the direction perpendicular to the surface: i.e. a locally two-dimensional surface in three-dimensional space.

Shells show both arch and plate behaviour as they make use of both axial and bending stresses to resist external action. This plate behaviour can be expressed using the Airy stress function (Figure 2.48).

Membrane theory (Figure 2.49) is also used to analyse shells where a third equilibrium equation perpendicular to the surface is considered and the curvature of the element in the absence of bending resists transverse loading. The existence of a solution in membrane theory depends on the shape of the shell and the boundary conditions. Violation of them would result in inextensional deformation (i.e. instability mechanisms). If a shell can undergo inextensional deformation, it will have to rely on bending stiffness, in addition to membrane action to safely carry the external loading. In any case a shell needs to have some bending stiffness to prevent buckling under compression and this is further highlighted in thin shells achieved from the efficiency of shell structures.

Gauss's Remarkable Theorem – "Gaussian curvature of a surface does not change if one bends the surface without stretching or tearing" - and Cohen-Vossen Theory – "it is not possible to deform a closed convex shape without changing lengths on the surface" - provide guidelines on behaviour of shells and thus acts as guidelines on valid shapes for shells. However, plate theory, membrane theory and bending theory of shells do not always have exact solutions, especially when the shape of the shell cannot be expressed mathematically; i.e. free forms.

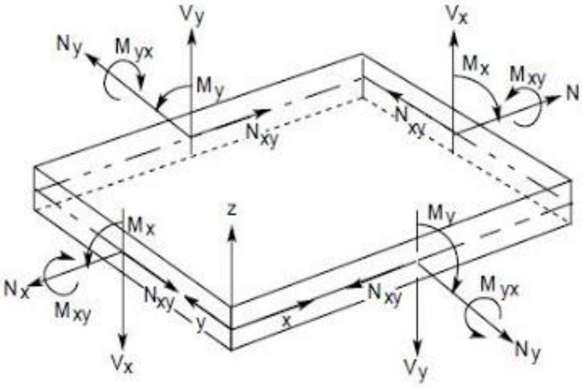

Figure 2.48: Load resistance action on a plate element.

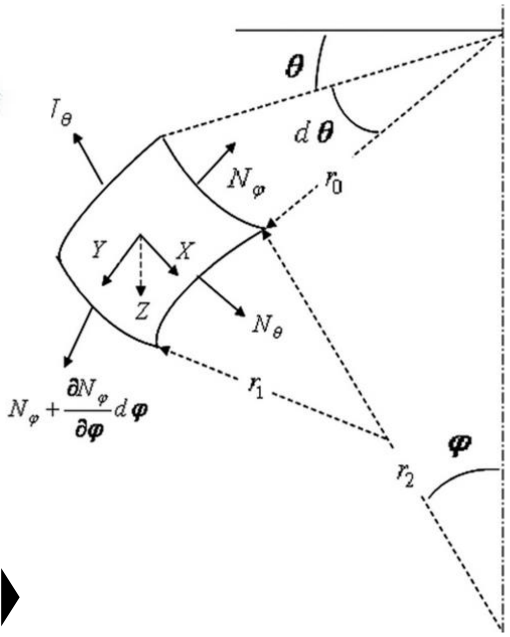

Figure 2.49: Load resistance action on a membrane element.

It is important to compare and contrast between the membrane action and the force networks giving funicular forms (i.e. the three-dimensional network of lines of thrust). Membrane action can carry any load given the material has sufficient strength in tension and compression. Note that this considers the elastic properties of the material. In contrast a force network does not consider material properties and is found to resist a given loading pattern. As strength is not the limiting criterion in a funicular form, the form is also scalable. This form-force relationship in a funicular means the design problem can be formulated to either find a funicular load or a funicular form. This leads to the need for generalized rules on discretization of a shell to a force network.

A force network matching the actual membrane forces would ideally give an optimum solution for a force network.

The importance of both the tools should be acknowledged as one would be better under one circumstance whilst the other in another; funicular solution would be preferred for the design of a grid-shell structure and membrane theory for a reinforced concrete dome. However, a domical shell made from a no-tension material such as masonry would require a funicular solution. Similarly, a funicular solution is advantageous for the form exploration of free-form shells.

2.4. The Current State of Form Finding of Free Form Surfaces

The availability of advanced tools – mathematics and computers- allowed the move from geometrical shells to the free-form shells. There is a renewed interest in these free-from structures and Mapungubwe National Park visitor centre (Figure 2.50) and MLK Jr Park Vault, Texas are to name but a few outcomes of this move.

Figure 2.50: Mapungubwe National Park visitor centre. Source: Ramage et al. [18]

All the developments discussed previously have lent a hand to the subject of form finding of free-form surfaces, as conceived today. It is interesting to summarise the current methodologies and ongoing developments with reference to the influence from earlier developments. This is presented in a graphical form (see Figure 2.51) and the following discussion is based on the same.

The current form finding methods can be broadly categorized into two groups: Computational methods and physical models. Computational methods can be further sub categorized into upper bound and lower bound analysis, in the context of limit analysis. Although, upper bound analysis can be an effective tool in analysis of structures which can be readily simplified to two-dimensional structures (e.g. arches), identifying an appropriate mechanism and parametrizing such a mechanism is not simple for a complex three-dimensional surface. This essentially leaves lower bound equilibrium analysis and physical models as the two main methods of analysing compressively self-supporting structures.

The equilibrium methods follow from the line of thrust idea from Hooke and Gregory, later developed by Gestner, Mery and Mosely and the influential developments by Young and rediscovery and reformulated by Heyman. Parallel to these concepts the field of graphic statics has grown as a tool for analysis and has significantly influenced the current day developments.

Thrust Network Analysis (TNA) developed by Block and Ochsendorf [19] is a computational method based on Heyman's safe theorem and force density method by Hans-Jörg Schek (1974). This methodology makes use of other allied developments in structural analysis, including reciprocal figure (J C Maxwell 1864) and matrix analysis of indeterminate frameworks (Pellegrino and Calladine 1986) and graphic statics. Subsequent improvements and optimization were done to the Thrust Network Analysis, borrowing ideas from other allied fields. For an example Liu et al. [20] used power diagrams by F Aurenhammer (1987) to make improvements to parametrization of dual diagrams. The current improvements to Thrust Network Analysis relates to physical realization of a structure in terms of construction and optimization therein.

A parallel development in equilibrium analysis is the membrane analysis based on the polyhedral stress functions developed by Airy (1863). Although this is a powerful analytical tool there are shortcomings when dealing with complex surfaces in 3D, with mathematically complex geometries and discontinuities. Membrane analysis has also been improved, making use of power of computers and borrowing ideas from discrete differential geometry and numerical homogenization theory to overcome its shortcomings.

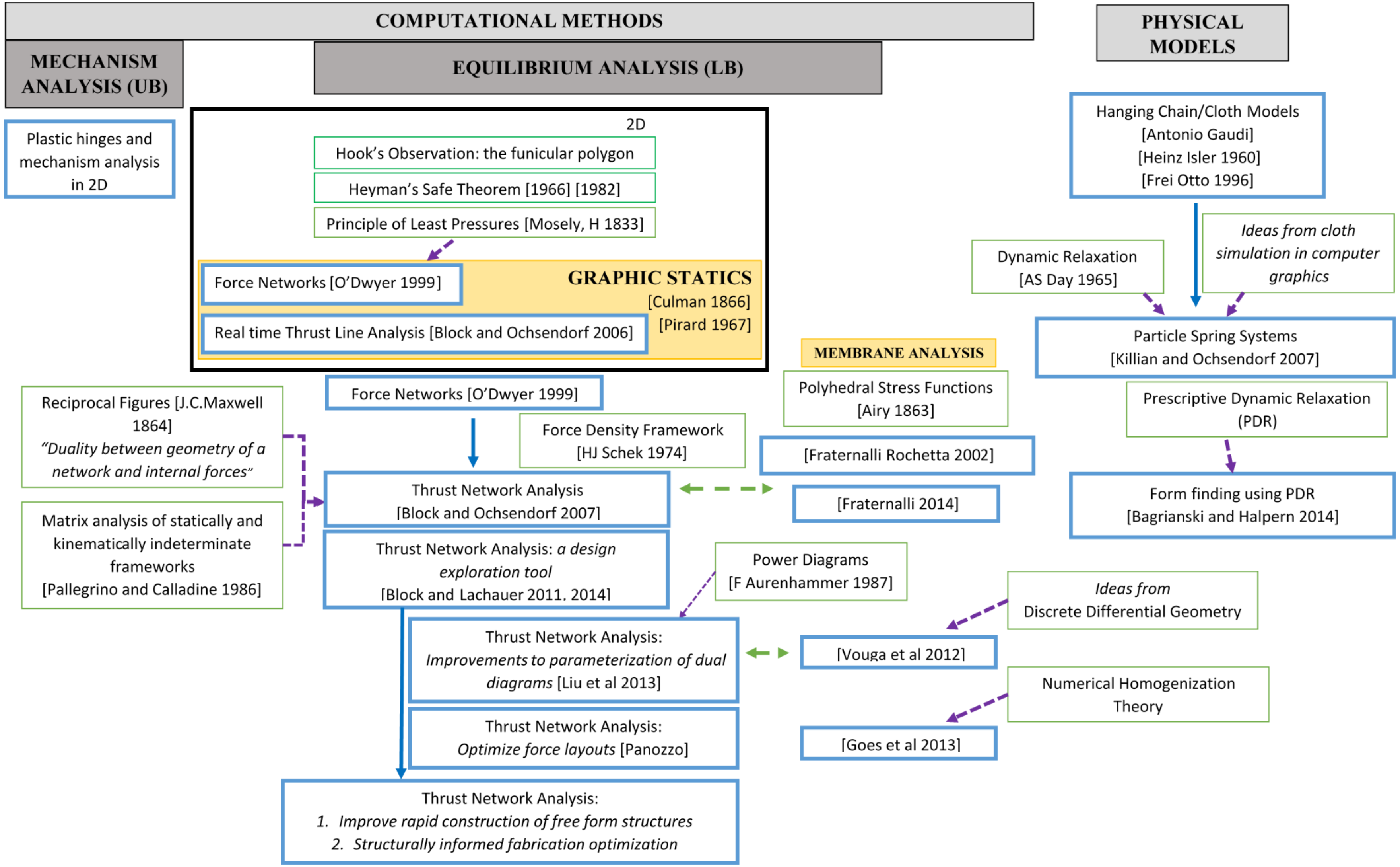

Figure 2.51: A graphical representation of the current form finding methodologies and inheritance from earlier findings and techniques.

Antonio Gaudi, in late 1800s, extensively used Physical models for form finding of masonry structures, which are compressively self-supporting. Heinz Isler in 1960s and Frei Otto in 1990s are a few prominent users of physical models in form finding of free form shells. The basis of physical models is Hook's observation of the duality between the catenary and the arch. However, Ney & Adriaenssens [21] note shortcomings in using a form active cable net to find the form of a form passive compression only structure. They note the lack of stability and robustness information from the cable net. Block [22] notes the separation of force and form systems and the non-intuitive nature of form exploration with cable networks (i.e. the change in the overall form due to a change in the length of one link is not easily predicted) as shortcomings of this system.

Physical models were implemented in computers based on the dynamic relaxation method presented by Alistair S Day (1965). Contemporary developments of software tools via this route includes particle spring systems (Figure 2.52) by Killian and Ochsendorf [23] and form finding using prescriptive dynamic relaxation by Bagrianski and Halpern [1]. Roca et al. [24] implemented a hanging chain model (i.e. funicular modelling) based on anti-funicular principle.

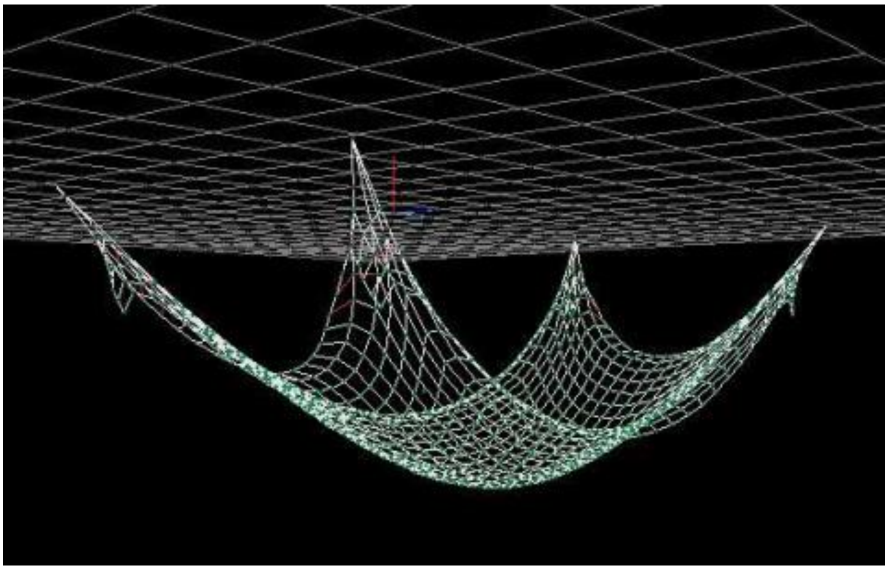

Figure 2.52: Particle Spring Model for form finding of a shell. Source: Killian and Ochsendorf [23].

At this point it is prudent to differentiate between pure structural analysis and form finding. A structural analysis tool such as line of thrust or membrane analysis would allow for the analysis of a structure to find the design forces and stresses of the structure under a given loading. Form finding for a compressively self-supporting structure is an extension of this process to a repetitive process where the structure is analysed under a given set of loads at each step and the structure is modified at each step if the specified constraints are not met. The constraints can be both structural – e.g. no tension conditions- and architectural – e.g. shape or depth.

Thrust Network Analysis - following force networks - and dynamic relaxation methods - following physical models - are the most prominent tools in form finding of compressively self-supporting structures. Adriaenssens et al. [25] show the strengths of these methods in specific problems; Force Density Method for unstrained timber grid-shells, Thrust Network Analysis for unreinforced masonry shells, Dynamic Relaxation for strained grid-shells and Particle Spring System for thin concrete shells.

They categorize the two former methods as Geometric Stiffness Methods as those methods are material independent. The latter two falls under Dynamic Equilibrium Methods. These two types are further discussed in Section 2.4.1 and 2.4.2.

2.4.1. Geometric Stiffness Methods

Force Density Method, also known as ‘Stuttgart Direct Approach’ was first introduced by Hans-Jörg Schek in 1974. The idea of force densities does not have an intuitive physical meaning, its function is to linearize the equilibrium equation of the force network. In terms of form exploration, changing the ratio of force densities to nodal load changes the shape of the force network, and in extension the shape of the equilibrium surface.

Thrust Network Analysis presented by Philippe Block and John Ochsendorf in 2007 [19] is a direct extension of the Force Density Method. Here the duality between form and forces is used to change the force densities intuitively to generate different forms. In using graphic statics to manipulate the dual diagram – i.e. the force diagram – the external loading is limited to a single direction – i.e. the gravity direction- to allow for the decoupling of horizontal and vertical equilibrium. A more involved discussion of the implementation and force exploration using Thrust Network Analysis is presented in Chapter 4.

2.4.2. Dynamic Equilibrium Methods

In dynamic equilibrium methods, the motion of the structure is followed through time under applied loads. In Dynamic Relaxation a flat grid of members connected at nodes are allowed to deform under gravity. At the end of each time step the residual forces are determined and the motion under the residual forces are calculated in the subsequent step. Viscous or kinematic damping are introduced for the system to converge to an equilibrium solution.

Particle spring system is different from Dynamic Relaxation as this considers a set of lumped mass nodes connected by massless springs, but otherwise follow a similar idea. The integration scheme is more involved than in Dynamic Relaxation and either an explicit or an implicit integration scheme could be used, with the latter being the more reliable method.

Dynamic relaxation method requires a wider range of inputs, but in contrast to Geometric Stiffness methods the variables used have a physical meaning, related to elasticity or damping. Also, the dynamic methods are numerically superior as the mass matrix is a diagonal matrix giving a simpler inversion, whereas the matrix to be inverted in Geometric Stiffness methods is not a diagonal matrix hence requires a more involved inversion process. On the other hand, Dynamic methods require iterations and convergence issues need to be dealt with.

However, Veenendaal & Block [26] note that a closer inspection of equilibrium equation from both Dynamic Equilibrium and Geometric Stiffness methods above shows that the methods are theoretically interchangeable.

3. IMPLEMENTATION OF THRUST NETWORK ANALYSIS

The original implementation of the Thrust Network Analysis (TNA) by Block and Ochsendorf [19] is presented Section 3.1. Two issues are identified in view of improving computational efficiency and versatility in usage of TNA. They are discussed in Section 3.2. The current implementation of TNA is discussed in Section 3.3.

3.1. Thrust Network Analysis

Thrust Network Analysis was presented by Philippe Block and John Ochsendorf [19] and is a graphic static approach to form finding of compressively self-supporting surfaces in three-dimensional space. This method is unique in that it is not only an analysis tool, but also a form exploration tool.

TNA is based on the ideas of (i) line of thrust, (ii) duality between form and forces, and (iii) force densities. The line of thrust idea comes from Heyman's safe theorem for the stability of masonry arches and is extended to the three dimensional free-form compression only shells. The duality between the force and form diagrams has long been used in graphic statics and is essential for the form exploration capabilities in TNA. Note that the form diagram is considered the primal and its dual is the force diagram. (The properties of the dual are denoted using the star superscript.) The idea of force densities is from Schek [27]and is used to linearize the equilibrium equation.

Block et al. [28] present the methodology in a flow diagram (see Figure 3.1) and note the decoupling of the horizontal and vertical equilibrium in this methodology. It should be noted that the above can be done when the external loadings are in the gravity (i.e. vertical) direction only, and this decoupling gives the form finding advantages to the TNA methodology.

The following section expands upon the methodology presented in Figure 3.1 with reference to the original implementation presented in the PhD thesis of Philippe Block [22] and the subsequent improvements at Block Research Group at ETH, Zurich and elsewhere. This discussion is complemented by an example given in Annex A.

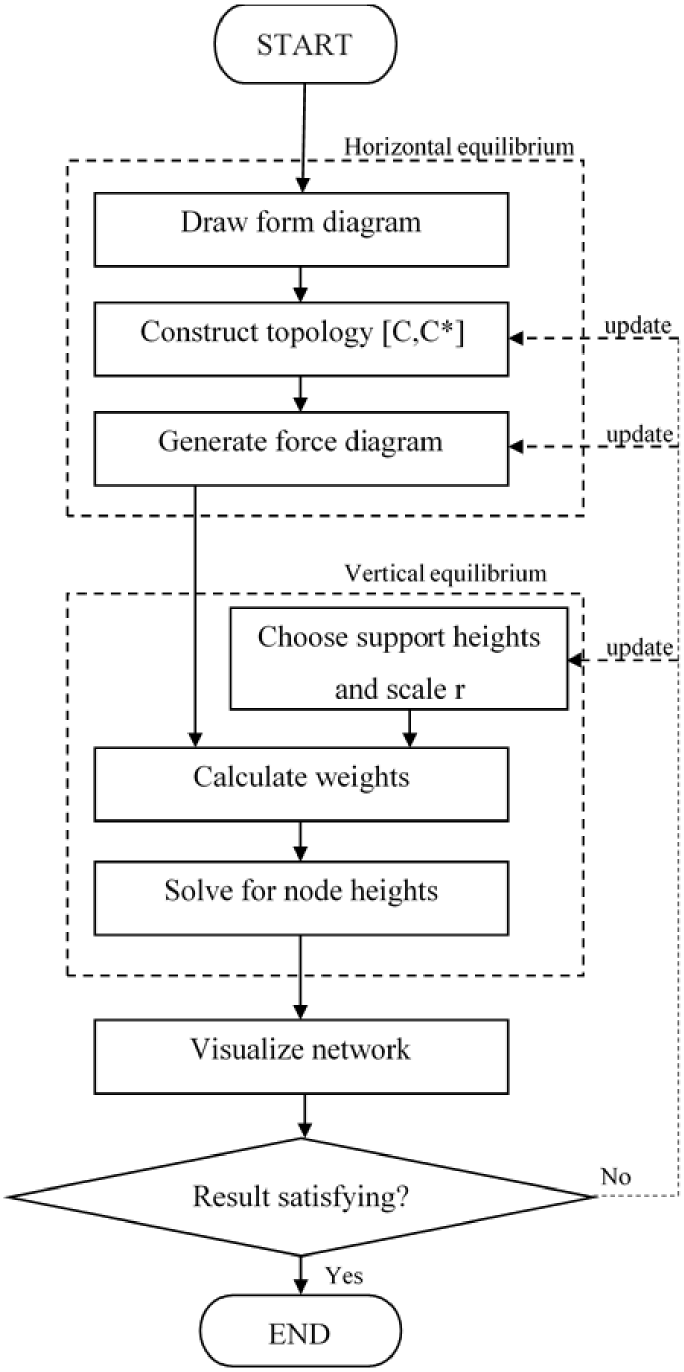

Figure 3.1: Flow chart of the Thrust Network Analysis process. Reproduced from [25].

Draw Form Diagram:

The thrust network is the extension to three-dimensional surfaces of the concept of line of thrust. The topology of the thrust network influences the final solution achieved. Hence it is important to have a proper strategy in transforming a given surface to a thrust network, where individual thrust lines best represent the flow of forces.

The force diagram (primal grid) is a two-dimensional projection of the thrust network and needs to be a plane graph. Note that a plane graph is a particular non-crossing embedding of a planar graph in a plane, and it can be shown that a graph would have geometric dual if and only if that graph is a planar graph [29].

Furthermore, to guarantee a compression (or tension) only solution it is required that the force diagram is planar [30]. Force diagram is the geometric dual of the form diagram. Whiteley et al. [30] show that a geometric dual of a planar graph is a planar graph. However, it is possible to draw a non-planar embedding of a planar graph. We will later show that we can ensure that the force diagram is a plane graph, and thus the solution is compression only. This is done by adjusting the independent branches of the force diagram. Whitney [31] further shows that a three connected graph has a unique embedding in a plane, as such a triangulated thrust network (form diagram) would have a three connected force diagram (dual diagram of form diagram) and thus a unique equilibrium solution.

Construct Topology:

The topology of the form and force diagrams are represented by a branch-node adjacency matrix (referred to as the adjacency matrix in the remainder of the thesis), which is an idea borrowed from graph theory. Adjacency matrix of the form diagrams can be directly constructed from the connectivity of the form diagram, and the adjacency matrix of the force diagram can be constructed considering the duality between the form and force diagrams. Properties of form and force diagrams (e.g. adjacency matrix, nodal coordinates) are distinguished using an asterisk superscript to denote the force diagram.

The thrust network can be considered a collection of branches connected at nodes, with each branch having a start and an end node (i.e. a directional graph). Then each row and column of the branch-node adjacency matrix represent a branch and a node of the thrust network: i.e. the branch-node adjacency matrix is of dimensions $m \times n$ where m is the number of branches and n the number of nodes in the thrust network. An element in the branch node matrix (c_{ij}) would be either 1, -1 or 0, based on the definition in equation 3.1.

$$c_{ij} = \begin{cases} 1; branch\ i\ starts\ at\ node\ j \\ -1; branch\ i\ ends\ at\ node\ j \\ 0; otherwise \end{cases} \tag{3.1}$$

The original and current implementation of the Thrust Network Analysis by the Block Research Group relies on a half edge data structure constructed during the definition of the form diagram to generate the adjacency matrix of the force diagram. Alternatively, the adjacency matrix of the force diagram can be construct manually from the form diagram.

In this thesis an automated procedure is proposed for the generation of the adjacency matrix of the dual diagram with adjacency matrix of the form diagram as an input. This new procedure decouples the construction of the adjacency matrix for the form and force diagram, and thus allows different options for the generation of thrust network and the form diagram (e.g. manual drawing, free CAD tools).

Generate Force Diagram:

As Block et al. [28] present there are four ways to generate the force diagram;

1. Manual construction following the rules of graphic statics
2. Automatic generation using an optimization problem
3. Computation using algebraic methods
4. Obtain iteratively by enforcing reciprocal constraints on form and force diagrams

The manual approach is only feasible with simple and/or small networks. Second and third procedures provide an important understanding of the reciprocal behaviour and form and force diagrams and this understanding is very important in carrying out form exploration with Thrust Network Analysis. The optimization problem is first presented as given in the PhD thesis of Philippe Block and then this is converted to an algebraic problem.

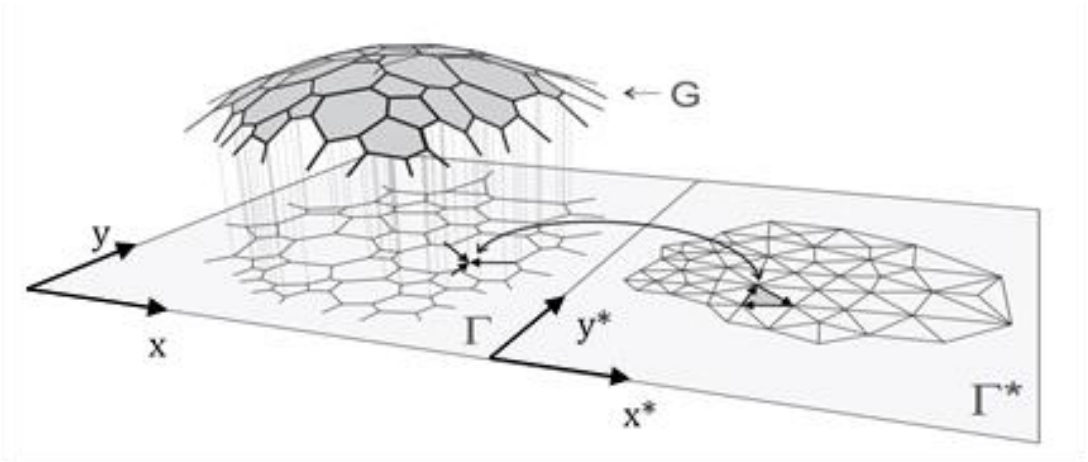

Figure 3.2: Representation of the thrust network for a compression-only shell (G) its projection to the horizontal plane giving the form diagram (Γ) and the dual of the form diagram as the force diagram (Γ^*). The image is adapted from Block and Ochsendorf [19].

The formulation of the linear optimization problem is based on the following observations.

i. Branch vectors in primal and dual grids are parallel and have the same direction

$$u^* = Ut \tag{3.2}$$

$$v^* = Vt \tag{3.3}$$

In equations 3.2 and 3.3, U, V and u^*, v^* correspond to the branch lengths along the x-y and $x*$-$y*$ directions in the form and force diagram, respectively (see Figure 3.2). These lengths are obtained by multiplying the adjacency matrix (C or C^*) by nodal coordinate vectors of the corresponding diagram; e.g. $u = Cx$, $u^* = C^*x^*$ and $U = diag(u)$ where x, y and x^*, y^* are nodal coordinates of the form and force diagram respectively.

ii. The equilibrium of the compressive branch forces coming together at a node of the force diagram is represented by a closed polygon in the force diagram.

$$C_i^T u^* = 0 \tag{3.4}$$

$$C_i^T v^* = 0 \tag{3.5}$$

; where $C = [C_i \quad C_b]$

In equation 3.4 and 3.5 C_i corresponds to the columns of the adjacency matrix corresponding to internal nodes. Equilibrium is satisfied at internal nodes for the chosen thrust network discretization. At supports the equilibrium will be satisfied by the support reaction but the direction of the support reaction is not restricted, hence guaranteeing equilibrium.

The resulting linear optimization problem can be summarized as follows;

Constraints:

$$A_{eq} = \begin{bmatrix} \multicolumn{2}{c}{I_{2m}} & -U \\ & & -V \\ C_i^T & 0 & \\ 0 & C_i^T & 0 \end{bmatrix}, \; b_{eq} = [0], \; x = \begin{bmatrix} u^* \\ v^* \\ t \end{bmatrix} \tag{3.6}$$

Cost function:

$$\min_t \sum_i t_i \quad \mathit{with} \;\; t_i \geq \frac{d}{l_i} \tag{3.7}$$

; where $\sum_i t_i = C^T x = [0 \quad 0 \quad 1^T m]$

Bounds:

$$\boldsymbol{lb} = \begin{bmatrix} -\infty \\ -\infty \\ d/l \end{bmatrix}, ub = [\,] \tag{3.8}$$

d is a positive scalar, l is branch length vector and m is the number of members in the thrust network. Minimization of t_i with a lower bound would result in a solution where thrust forces in all members $(t_i l_i)$ end up being closer to the value of d. The value of d is irrelevant as the solution is scalable.

After solving the linear optimization problem, the following minimization operations are done to extract the nodal coordinates of the dual grid. Note that there is no specified position for the dual grid in the two-dimensional space. Hence an arbitrary base point (x^0, y^0) needs to be given a priori. This force diagram should be considered the starting dual grid from which form exploration will commence.

$$\min_{x^*} x_1^* \;\; s.t. \begin{cases} C^* x^* = u^* \\ x_1^* = x^0 \end{cases} \tag{3.9}$$

$$\min_{y^*} y_1^* \;\; s.t. \begin{cases} C^* y^* = v^* \\ y_1^* = y^0 \end{cases} \tag{3.10}$$

The original implementation of the Thrust Network Analysis by Block and Ochsendorf [19] present the above as the linear optimization problem. This is computationally inefficient as opposed to an algebraic solution. In fact, they themselves notes it as a bottleneck in computational efficiency.

Block and Lachauer [32] present an algebraic solution as follow. They first reform the horizontal equilibrium equation by combining equations 3.1 to 3.4, resulting in equation 3.11.

$$Aq = \begin{bmatrix} C_i^T U \\ C_i^T V \end{bmatrix} q = 0 \tag{3.11}$$

It is evident that the solution for q is in the null space of A [2].Vector q is the vector of '*force densities'*, which is defined as the axial force in the member as a fraction of the member length. Note that vector t in equations 3.2, 3.3 and 3.6 is the same force density vector q in equation 3.11.

An important point to note here is that the vector q contains both independent and dependent elements. This notion of independent and dependent force densities (q_{ind} and q_{dep}) is important for the form exploration capabilities of Thrust Network Analysis. Mele and Block [33] present form and force diagrams with branches corresponding to independent force densities (Figure 3.3), and changing of those will change the force densities dependent on that and this in turn would alter the form of the structure; i.e. q_{ind} are the form exploration parameters. This relationship between form and force (e.g. a higher thrust density would give a shallower form) is explained in detail in Block's PhD thesis [22].

The number of independent force densities is equal to the dimension of the null space of *A*. The branches corresponding to the independent force densities can be identified

---

[2] Null space of matrix A is the collection of all vectors x, such that Ax=0.

by either observation of the force diagram or linear algebraically determining the linearly independent rows of the null space of *A* (by way of carrying out a row reduction using Gauss-Jordan elimination).

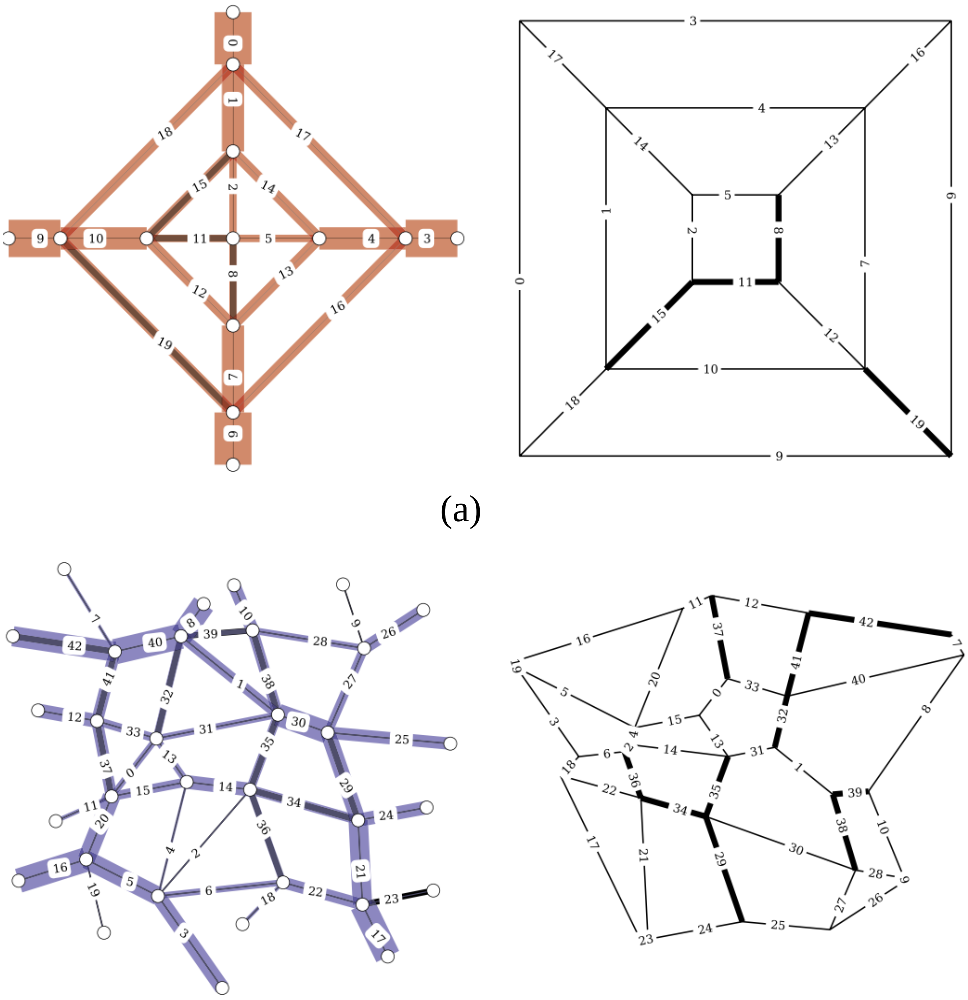

(a)

(b)

Figure 3.3: Form (left) and force (right) diagrams for self-stressed compression only (a) regular and (b) random networks, with thick edges in force diagram indicating a set of independent thrust forces. Source: Mele and Block [33].

Once the independent force densities (q_{ind}) are selected, dependent force densities (q_{dep}) can be determined from the equation 3.12, which is reproduced from Block and Lachauer [32].

$$q_{dep} = -{A_d}^{+} A_{ind} q_{ind} \tag{3.12}$$

In equation 3.12, A_d is the columns of A corresponding to the dependent force densities and similarly A_{ind} is the collection of columns of A corresponding to the independent force densities. ${A_d}^+$ $(= \left({A_d}^T A_d\right)^{-1} {A_d}^T)$ indicates the Moore-Penrose pseudo-inverse of A_d [34]. Note that to ensure a compression only solution all q need to be positive (or all negative).

Calculate weights:

Nodal loads are calculated based on the tributary areas of each node in the target form, as obtained by Voronoi tessellation. The target form is defined either by (i) the intrados and extrados or (ii) the centreline of the target shape and the thickness of the shell.

Solve for node heights / realized structure

Block [22] presents the following linear optimization problem (equations 3.13-3.15) to solve for nodal heights by imposing equilibrium in vertical direction.

Constraints:

$$A_{eq} = [C_i^T (L_H^{-1} L_H^*) C_i \quad p_z],\ b_{eq} = [0],\ x = \begin{bmatrix} z \\ r \end{bmatrix} \tag{3.13}$$

Cost function:

$$\min_x \ C^T x = [0 \quad \pm 1] \begin{bmatrix} z \\ r \end{bmatrix} \tag{3.14}$$

Bounds:

$$\boldsymbol{lb} = \begin{bmatrix} z^{LB} \\ -\infty \end{bmatrix}, ub = \begin{bmatrix} z^{UB} \\ +\infty \end{bmatrix} \tag{3.15}$$

Equation 3.13 satisfies force equilibrium in vertical direction at every internal node, where p_z correspond to the loading at each node – i.e. the self-weight calculated in previous step. Thus note that the equilibrium form is found under self-weight loading only. L_H(or ${L_H}^*$) is the diagonal matrix containing the horizontal lengths of the branches of form (or force) diagram, r is a scaling parameter in vertical direction (i.e. height direction), z is the nodal height vector with superscripts LB and UB corresponding to the intrados and extrados of the shell.

In contrast to exploring forms by varying the vector q_{ind} in the horizontal equilibrium solution, vertical equilibrium solution uses the scaling parameter r which changes the overall height of the structure in the direction of the vertical equilibrium. Changing of this scaling parameter allows us to find a solution within the bounds of intrados and extrados, along with the extreme cases of deepest, shallowest and best-fit to mid depth solutions.

Best fit solution

Block and Lachauer [32] reform the above form finding process to find the best-fit solution to at target surface (equations 3.16-3.18). The problem was formulated as a least-squares best fit to the mid-surface (z_i^M) of the target shell. They have implemented an optimization which minimizes the difference between the target nodal heights and realized nodal heights (equation 3.18). The two constraints correspond to (i) satisfying vertical force equilibrium (equation 3.16) and (ii) guaranteeing a compression only solution (equation 3.17).

Constraints:

$$D(q_{id})z(q_{id}) - p_z = 0\,; where\ D = \ C_i^t Q C_i \tag{3.16}$$

$$q = \begin{bmatrix} q_d \\ q_{id} \end{bmatrix} > 0 \tag{3.17}$$

Cost function:

$$\min_{q_{id}} f(z_i) = \left\| z_i(q_{id}) - z_i^M \right\|^2 \tag{3.18}$$

For the above non-linear minimization problem in equations 3.16-3.18, they use an interior-point method. Note that q_{id} is the variable of the minimization problem and z_i is implemented as a black-box function of input variable q_{id}.

Block and Laucher [32] note the above optimization problem to be non-linear and non-convex. A good starting point is important for the optimization due to the non-convexity of the problem. They employ a quadratic programming problem with a condition to minimize the horizontal force components to generate a good starting point. A simpler starting point using Voronoi diagrams is used in the current implementation, but the generality of this procedure is not yet verified.

Horizontal loading

Marmo and Rosati [35] extend the Thrust Network Analysis to simultaneous consideration of horizontal and vertical loads, but in doing so eliminate the force diagram. This essentially eliminates the form steering capacity inherent to the Thrust Network Analysis and obtains the deepest or shallowest solution under the given loading. However, they retain the overall scaling parameter r within the new formation and it would be interesting to investigate how the form change with r, in their formulation.

3.2. Improvements to Block and Ochsendorf (2007) Implementation

In the current implementation, two improvements are proposed to the Block and Ochsendorf (2007) implementation. The first is to the linear optimization problems in the methodology. The original authors too have noted this as a bottle-neck in computations. The reformulation of the problem as a linear algebraic problem was identified as an improvement. The original start and commencement of our work was in 2014 and Block and Laucher [32] have beaten us to the finish line as they too have recognized the linear algebraic solution and presented a more extensive discussion on it. However, while ceding that this is no longer an original work, we would claim that ours is an independent development from theirs. In fact, Block and Laucher [32] use the linear algebraic solution for the first linear optimization problem only. In contrast we are using that for the second optimisation problem, taking advantage of the fact that Moore-Penrose pseudo inverse gives the least-squares solution to a problem. In Section 3.2.1 this linear algebraic solution to the second optimization process is presented.

The second improvement is to the generation of force network, which was implemented by the original authors of the TNA using a half edge data structure which was created as the thrust network is drawn in the CAD interface. Not only does this implementation takes a lot of data storage, but it also limits the ability of the user to use alternative drafting tools (e.g. manual drafting and manual input, using alternative

CAD tools). It was decided to use tools in graph theory in developing the dual graph. The motive was to both make the generation of the force network independent of the definition of the primal grid, and to make use of the strengths in the more robust field of graph theory to make interpretations on the equilibrium structure based on the characteristics of the dual graph.

3.2.1. Linear Algebraic Solution

A linear algebraic solution was implemented to solve for nodal heights in the Thrust Network Analysis. It is a step by step process as opposed to the cyclic nature in the linear optimization problem. Furthermore, since the current implementation was done in S [36] and the solution deals with matrices, there is the added advantage of making use of GNU Octave’s strong suit of handling matrices.

The linear optimization problem is converted to a linear algebraic problem using the null space of the matrix A_{eq} (equation 3.6). As b_{eq} is always a zero vector, the solution x will be in the null space (i.e. kernel) of A_{eq} (equation 3.19-3.21). In equation 3.20, ψ is the null space of A_{eq} and a possible solution for x can be generated using the coefficient vector α (equation 3.21). This essentially changes the variable of the problem from x to α.

$$A_{eq}x = b_{eq} = [0] \tag{3.19}$$

$$\psi = \ker\left(A_{eq}\right) \tag{3.20}$$

$$x = \psi\alpha \tag{3.21}$$

Part of the solution vector x has a reasonable estimate – i.e. the nodal heights of the target surface. The null space matrix ψ will be partitioned in its row space to those corresponding to the known and unknown parts of x (equation 3.22). Note that this partitioning does not affect the coefficients vector α (equation 3.22). Moore-Penrose pseudoinverse is then used to find α (equation 3.24). Ones the coefficients vector α_{sol} is determined the solution vector x can be obtained (equation 3.25).

$$x = \begin{bmatrix} x_k = z^M \\ x_u = r \end{bmatrix} \tag{3.22}$$

$$x_k = \psi_k \alpha \tag{3.23}$$

$$\alpha_{sol} = [\psi_k]^{-} x_k \tag{3.24}$$

$$x = \psi \alpha_{sol} \tag{3.25}$$

Moore-Penrose pseudoinverse gives the least-squares solution to the target solution (z^M) [37]. This is essentially the linear optimization solution, achieved through direct matrix operations.

3.2.2. Generation of Force Diagram with Graph Theory

Generating the branch-node adjacency matrix of the force diagram is fundamentally the problem of finding the vector space of all chordless cycles of the form diagram – i.e. the cycle basis of the form diagram with all elements of the basis being planar. Most of the existing solutions are computationally expensive solutions, especially so when the form diagram is very large.

Marcel Wild [38] solution was identified as an optimal solution upon which the current implementation is based. Taking advantage of the fact that the primal grid has a known embedding, Marcel Wild [38] solution is further improved to give efficiency even with large networks.

Marcel Wild [38] solution is based on the fact that for a chordless cycle each node (of the network) should have either two members of the cycle connected to it or none at all. With that an iterative process is implemented, further making use of principle of exclusion for rapid convergence to a solution.

Simple cycles only

Only simple cycles should be included in the above cycle basis. Simple cycles can be defined as a closed walk with no repetition in edges or vertices, except for the starting and closing vertices. As such the process needs to eliminate the generation of cycles such as shown in Figure 3.4. However, the Marcel Wild process would eliminate such generations by allowing only two edges to be connected to a given vertex.

No proper cycle packings

However, the Marcel Wild [38] implementation might generate a proper cycle packing as a cycle basis. A proper cycle packing is a collection of two or more cycles which do not share any vertices (see Figure 3.5).

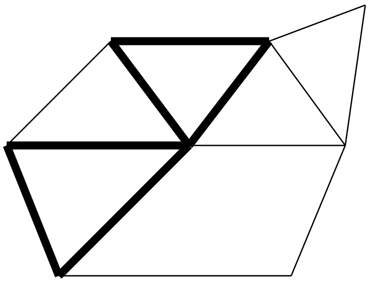

Figure 3.4: A non-simple cycle.

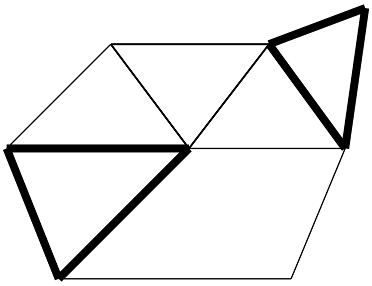

Figure 3.5: A proper cycle packing.

Generation of such cycle packings are eliminated by limiting the number of edges allowed in a cycle. Thrust networks commonly defined would have either triangles (three vertices) or quadrilaterals (four vertices) as the smallest chordless planar cycles. As such limiting the number of edges to the size of the largest chordless planar cycle would eliminate proper cycle packings. This is checked at each iteration of the procedure to eliminate unnecessary future operations in the process.

Chordless cycles only

The cycle basis should only contain chordless cycles (see Figure 3.6). A chordless cycle is a cycle where the set of edges in the graph which are not in the cycle but are connected to two vertices of the cycle, is empty. This too can be eliminated by limiting the number of edges to three in a triangulated grid. If the force network has polygons of higher order, chordless cycles need to be checked explicitly.

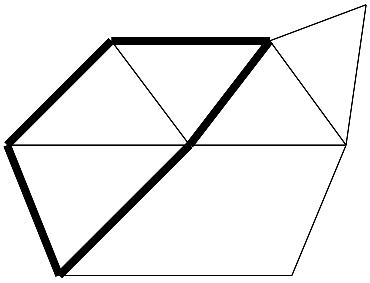

Figure 3.6: A cycle with chords.

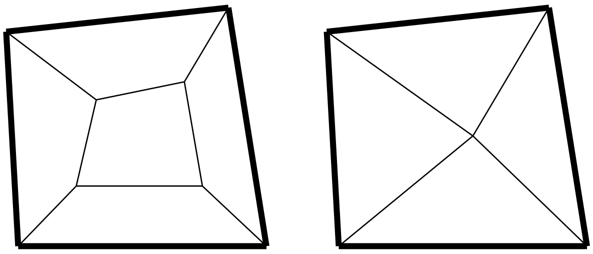

Figure 3.7: Quadrilateral enclosing quadrilaterals or triangles.

A further complex situation from above is the existence of a cycles enclosed in cycles. This can be characterized by a path between two nodes of a cycle, where the path is not part of the cycle and is inside the cycle (see Figure 3.7). It should be obvious this definition is considering a particular embedding of the graph - thus the notion of 'inside' the cycle. This too need to be checked explicitly.

Split and stitch

One of the major drawbacks in algorithms finding cycle spaces is the time inefficiency as the network expands. A split and stitch procedure – an idea from audio/video editing – is used to break down the problem and thus improve time efficiency. The idea is that the nodes in space can be separated into disjoint groups and a chordless cycle would not be present connecting nodes of non-adjacent blocks of nodes. The large network is split into non-overlapping blocks of nodes, and cycle spaces are generated locally within the block. Then the adjacent blocks are stitched together along the border to find the cycles broken by the splitting (see Figure 3.8). Finally, the indexing of nodes and cycles are changed from local to global node numbering to arrive at the final chordless cycle space. This cycle space is the member-node adjacency matrix of the force network.

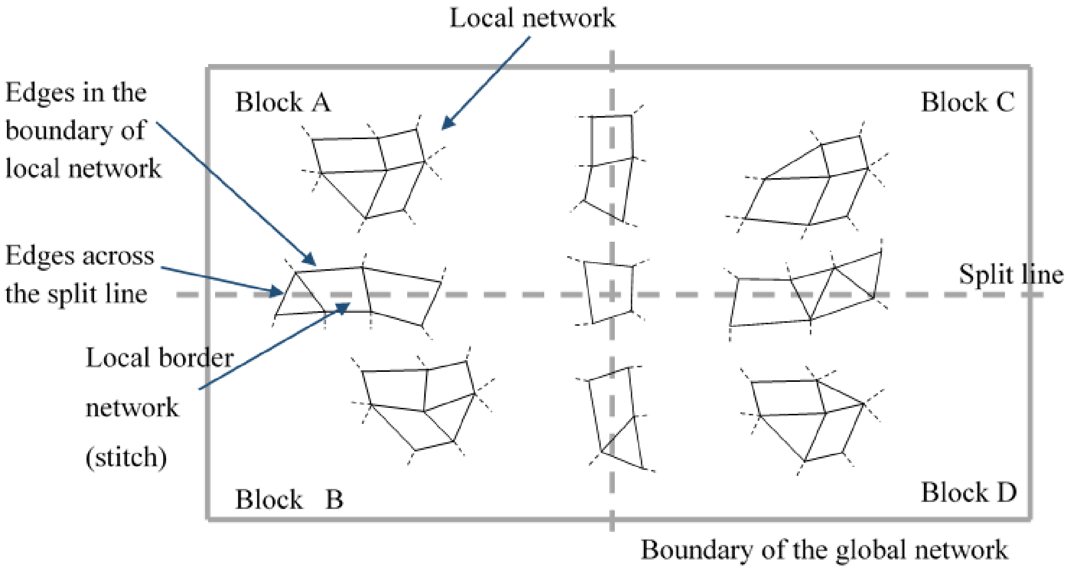

Figure 3.8: An example of a network being partitioned for the split and stitch procedure.

In the current implementation splitting was done in a rectangular grid, assuming the nodes of the form diagram to be distributed evenly in a rectangular space. This is not generally an optimal way of splitting but is simple and works well with the example used in Section 3.3.

To further optimize the procedure different sizes of the split are trialled and an optimum split size is decided. Note that the splitting is based on the total number of nodes (of the form diagram) and the average number of nodes expected in each block (target nodes). However, the actual average number of nodes in the blocks after splitting (realized nodes) would be different from the number of target nodes, as the nodes are not evenly distributed in space.

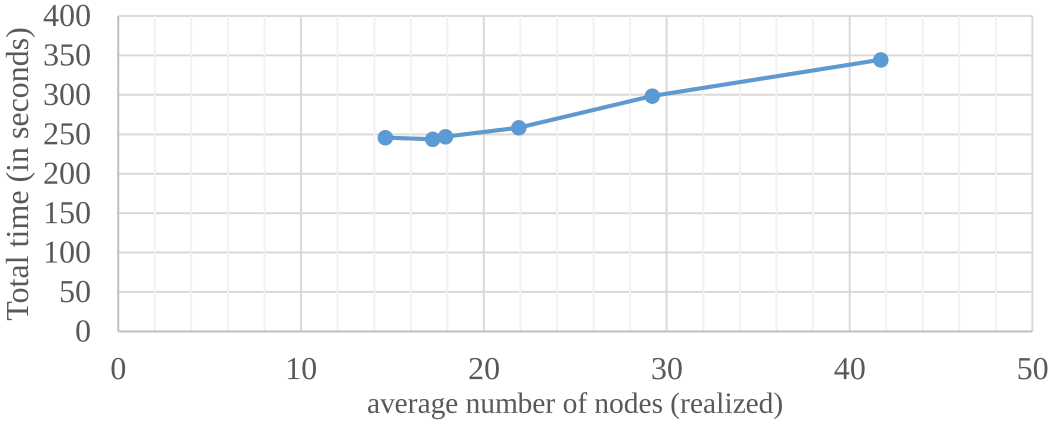

Figure 3.9: Total time spent in generating the dual network against the average number of nodes in each block (local network).

It is evident from the iterative process that the computation time is dependent on the number of nodes. The computation time would decrease as the number of nodes in each block decreases. However, when the number of nodes in each local group is very low, that too become computationally inefficient due to the overheads involved with evaluating the cycle space of a block and stitching of adjacent blocks. As a preliminary study, a sample network was used to study the change of the total time consumed in the split and stitch process as the number of realized nodes changes (see Figure 3.9).

It was observed that an average number of 18 nodes realized would give an optimum time in the process. This optimum number can vary with the nature of the form diagram (e.g. triangulated, quadrilateral, etc.), distribution of nodes and the numbering of nodes.

3.3. Current Implementation

The new implementation of the Thrust Network Analysis was carried out in GNU Octave software package. Unlike in the original implementation of the Thrust Network Analysis by Block and Ochsendorf [19], the definition of the thrust network and the analysis are made independent, allowing for user expertise to dictate the tools used for the definition of target shape and the shape of the thrust network.

The current implementation is built around five functions and are discussed separately. These should be read with reference to Section 3.1 and Figure 3.11. The categorization is to both simplify the code and to make real-time updates in the GUI more efficient. Note that only specific points of interest are noted here.

The process is discussed with a form finding exercise. The target shape is as shown Figure 3.10(a), where the shell is to be supported along all four edges. The thrust network discretization of the target surface is as shown in Figure 3.10(b), where the discretization is a simple quadrilateral mesh. The thrust network is of 26 boundary nodes, 42 internal nodes and 97 branches (in black in Figure 3.10(b)). The boundary of the thrust network is indicated in blue lines in Figure 3.10(b) and note that these are not thrust network branches.

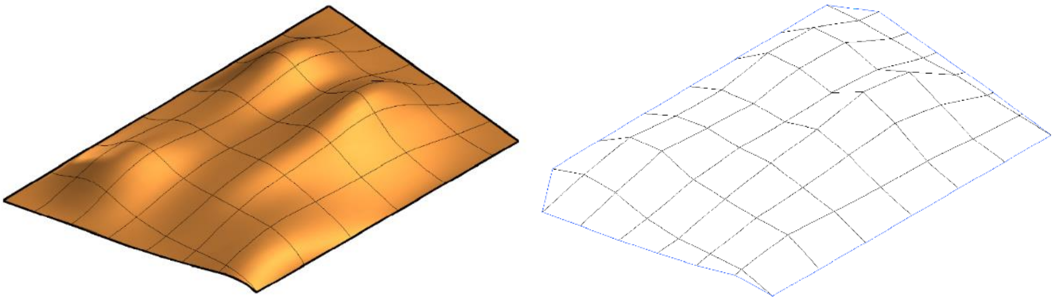

(a) (b)

Figure 3.10: (a) Target free-form surface and (b) its thrust network discretization for sample implementations of thrust network analysis.

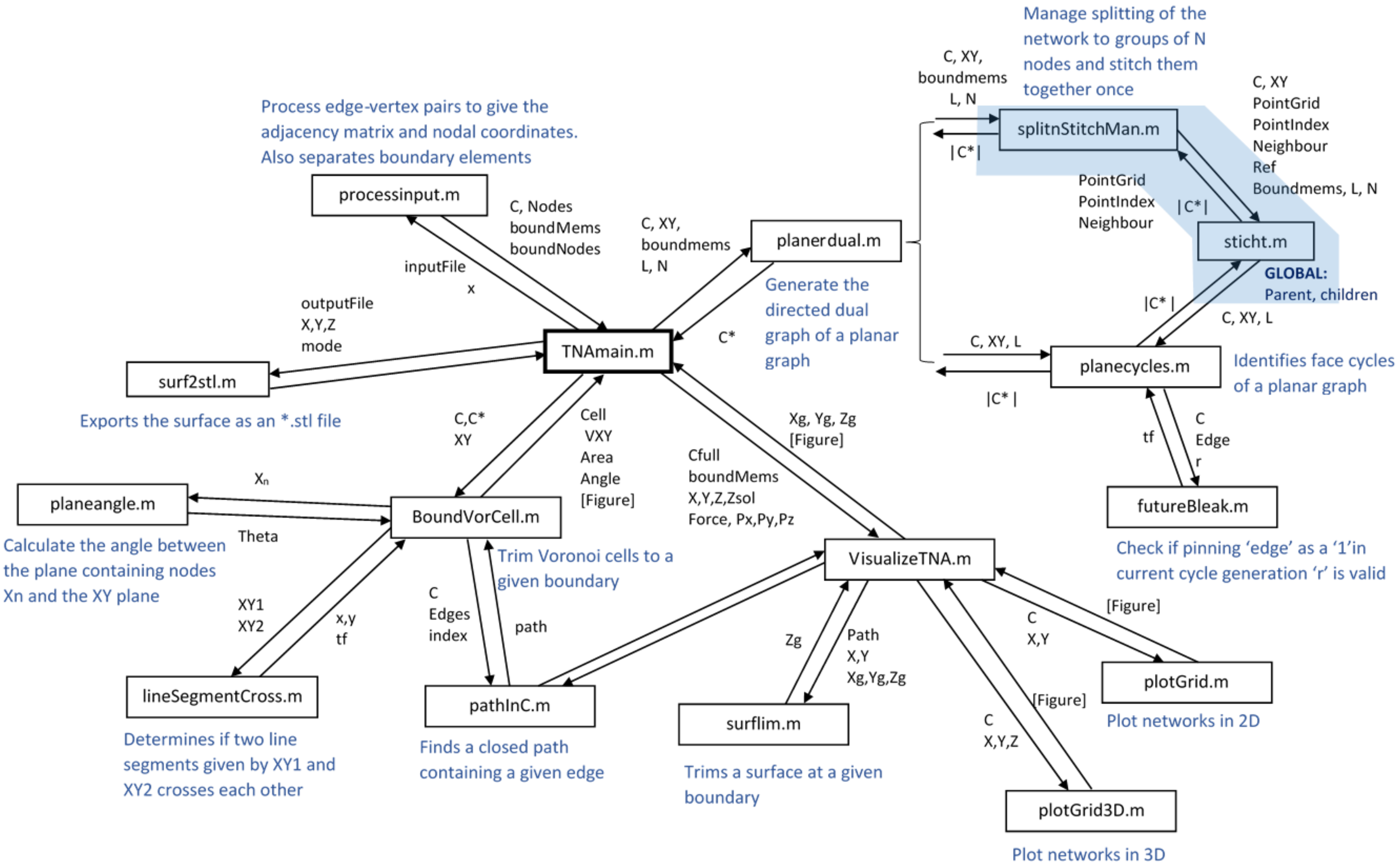

Figure 3.11: Call-diagram indicating the function calls in the software implementation in GNU Octave.

3.3.1. connectivityTNA

This function takes the definition of the thrust network (a list of member start and end nodes) as the input and generates the adjacency matrices for both the form and force diagrams as the primary output. As secondary output it generates the nodal load vector and corresponding lengths of the Voronoi dual of the thrust network. The latter is used as a starting point for the force network in Section 3.3.3.

In the current implementation the input is required as a list of nodal pairs (i.e. two sets of x, y, z nodal coordinates). With this input it is straightforward to generate the adjacency matrix of the form (primal) diagram. Generation of the adjacency matrix of the force (dual) diagram is done as discussed in Section 3.2.2.

Nodal load vectors should ideally be generated while solving for the vertical equilibrium as the actual form taken by the shell influences the nodal loading – scaling in vertical direction would stretch some parts of the shell more than the others. However, as we are starting with a target form and even after further form adjustments, we would most likely end up with a shape closer to the target shape, we would generate a constant nodal load vector based on the target surface. It is advantageous to do that at this stage to avoid unnecessary duplication of pre-processing of input data.

Voronoi cells are generated using the built-in Voronoi diagram functions in GNU Octave. Necessary adjustments are made to the built-in function such that the Voronoi cells are terminated at the boundary of the shell (see Figure 3.12).

A Voronoi cell is represented by an ordered list representing its vertices. The Voronoi cell vertices list was updated if the cell cuts across the network boundary. It is evident from Figure 3.12 that the Voronoi cells requiring updating are Voronoi cells corresponding to (i) boundary nodes (e.g.- brown cells) and (ii) interior nodes connected to a boundary node via a branch (e.g.- purple cells). Note that cells of boundary nodes always need to be updated but is not the case for interior nodes (e.g.- red interior cell does not need updating while purple interior cells need updating).

The Voronoi cell edges cutting across the network boundary can be categorized into three groups based on the origin of the Voronoi cells sharing the cell edge that cut across the network boundary; (i) two boundary nodes (e.g. - boundary between brown and pink cells in Figure 3.12), (ii) boundary node and an internal node (e.g. - boundary between orange and purple cells in Figure 3.12), (iii) two internal nodes. In case (i), the intersection point (and hence the new vertex for the Voronoi cell vertices list) would be the mid-point between the corresponding boundary nodes. In both other cases the intersection points need to be determined by solving equations of the corresponding line segments.

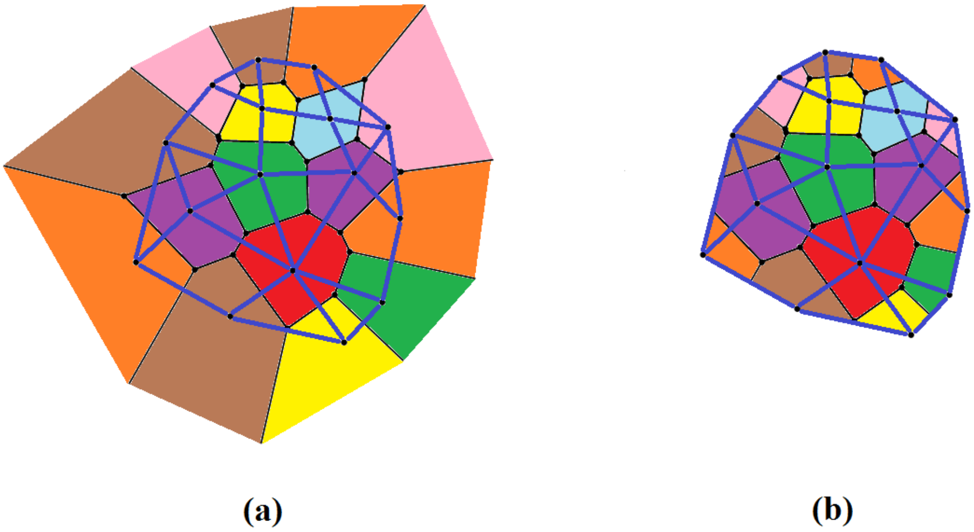

Figure 3.12: (a) Inifinity bound Voronoi diagram and (b) finitely bounded Voronoi diagram. Corresponding thrust network indicated in blue lines.

Once the new vertices for the corresponding Voronoi cells are determined the Voronoi cell lists can be updated by removing all the Voronoi vertices outside the network boundary and replacing them with the corresponding new vertices found earlier and the boundary nodes themselves, where necessary.

This process was implemented as an iterative process evaluating Voronoi cells corresponding to the boundary nodes, one at a time. This process eliminates the need to go through any internal nodes, since each update of new vertex is incorporated to the two cells sharing the vertex, and thus automatically updating any Voronoi cells corresponding to interior nodes.

3.3.2. horzeqTNA

"horzeqTNA" function solves for the horizontal equilibrium of the thrust network and identifies the independent force densities and the relationship between the independent and dependent force densities (see equation 3.12).

The major operation in this function is finding the null space of the horizontal equilibrium matrix A (see equation 3.11). This matrix is of dimensions $2n_i$ x m, where n_i is the number of internal nodes in the thrust network (and form diagram) and m is the number of branches in it. Hence as the network grows the matrix A grows and the memory requirement for the null operation grows. However, it could be noted that the matrix A is sparse (i.e. most of the elements are zeros) as the adjacency matrix C is sparse. A matrix in the current example is of size 84 x 97 and only have 264 non-zero elements (3.2% of total elements of the matrix).

Matrices which are known to be sparse can be defined in sparse format to eliminate redundant and trivial numerical operations (e.g. add to zero, multiply by zero) and would significantly reduce the time and memory requirements. In sparse format, only the non-zero elements are recorded in triplets indicating the row index, column index and the corresponding value.

The in-built null function in GNU Octave uses singular value decomposition (SVD) to generate the null space and would generate dense matrices in the process and thus using sparse format would be computationally inefficient. Hence LU decomposition and QR decomposition with sparse matrix format is used to make the process of finding the null space much more efficient, in terms of memory requirement and run-time.

LU Decomposition

A given matrix can be decomposed into the multiplication of a lower triangle matrix (L) and an upper triangle (U); $A = LU$. The decomposition can be done using Gaussian elimination in row space, without changing column space and thus preserving the null space. It is noted that LU decomposition is a viable approach to find the null space in exact arithmetic. However, implementation of this with floating point arithmetic will result in inaccuracies due to accumulation of numerical errors. The advantage lies in L and U being sparse if A is sparse.

The null space can be generated from the non-pivot columns of the row reduced echelon form of *U*. The null space of *A* shall be given as in equation 3.26 where U_1 is invertible upper triangle with non-zero pivots on the diagonal.

$$null(A) = \begin{bmatrix} {U_1}^{-1}U_2 \\ -I \end{bmatrix}; where\ U = \begin{bmatrix} U_1 & U_2 \\ 0 & 0 \end{bmatrix} \tag{3.26}$$

It can be easily shown that the above is indeed the null space of A:

$$\begin{aligned} &Let, x = \begin{bmatrix} {U_1}^{-1}U_2 \\ -I \end{bmatrix} \\ &Ax = LUx \\ &\quad = L\begin{bmatrix} U_1 & U_2 \\ 0 & 0 \end{bmatrix}\begin{bmatrix} {U_1}^{-1}U_2 \\ -I \end{bmatrix} \\ &\quad = L\begin{bmatrix} U_1{U_1}^{-1}U_2 - U_2 \\ 0 \end{bmatrix} \\ &\quad = L\begin{bmatrix} 0 \\ 0 \end{bmatrix} \\ &\quad = 0 \end{aligned} \tag{3.27}$$

The built-in LU decomposition function in GNU Octave does not generate a U matrix of the form mentioned in equation 3.26. A MATLAB function written by Kowal Pawel [39] is adapted to compute the null space from LU decomposition. This code is based on the paper by Gotsman and Toledo [40] on the computation of null spaces using sparse LU factorization with partial pivoting of the input matrix.

QR Decomposition

A given matrix can be decomposed into the multiplication of an orthogonal matrix (Q) and an upper triangle matrix (R); *A* = *QR*. The decomposition can be done using Gram-Schmidt process, Givens rotations or Householder reflections. If A is of *m* rows, *n* columns and rank r, Q and R can be partitioned as in equations 3.28 and 3.29.

$$Q = \begin{bmatrix} \underset{m\times r}{Q_1} & \underset{m\times(m-r)}{Q_2} \end{bmatrix} \tag{3.28}$$

$$R = \begin{bmatrix} \underset{r\times n}{R_1} \\ \underset{(m-r)\times n}{0} \end{bmatrix} \tag{3.29}$$

Considering orthogonality of Q ($Q^T Q = I$) it can be shown that Q_2 is the null space of A^T (equation 3.30).

$$\begin{bmatrix} R_1 \\ 0 \end{bmatrix} = R = Q^T A = \begin{bmatrix} {Q_1}^T \\ {Q_2}^T \end{bmatrix} A = \begin{bmatrix} {Q_1}^T A \\ {Q_2}^T A \end{bmatrix}$$

$$\Rightarrow {Q_2}^T A = 0$$

$$\Rightarrow A^T Q_2 = 0 \tag{3.30}$$

The null space was generated from QR decomposition adapting a MATLAB function written by John D'Errico [41].

The above three methods are evaluated under time and memory efficiency. Time efficiency is evaluated considering the time spent in the execution of code segment generating the null space. Memory efficiency is measured by considering the number of non-zero elements in the matrices generated in the decomposition method used.

Table 3.1 presents a summary of this evaluation. Using QR decomposition was computationally faster but would require considerably larger memory, especially for larger networks- a network with 876 nodes, 2512 members and 1637 faces gave out of memory errors for both QR and SVD decomposition methods. Note that all three methods resulted in the same final thrust network.

The examples used by Gotsman and Toledo [40] show LU decomposition to be faster than QR decomposition, but they attribute the inefficiency to the built-in LU and QR functions: the MATLAB version they used has a state-of-the-art sparse LU factorization but an older sparse QR. Gotsman and Toledo [40] also note the possibility of LU based algorithms failing due to scaling and overflow problems (i.e. overflow of floating points). The same issue was faced in the current example and was avoided by adjusting the zero tolerance to a larger value – 1.0e-5 instead of the computed value of 2.2145e-013.

Table 3.1: Comparison of time and memory efficiency of SVD, LU and QR decomposition in computing the null space of a sparse matrix.

	SVD	LU	QR
Operation time (sec.)	0.012	0.007	0.004
Memory usage (number of non-zero elements)	S - 7056 (100%)* V – 84 (1%)* D – 9409 (100%)*	L – 90 (1.3%) U – 258 (3.2%)	Q - 5782 (61%)* R - 2290 (28%)

*not defined as sparse matrices

3.3.3. optimqTNA

“optimqTNA” function carries out the optimization process presented under ‘best fit solution’ in Section 3.1. The optimization problem at hand is a general non-linear constrained optimization (i.e. an inequality constraint of non-negative force densities is used) and can be optimized using sequential quadratic programming, Lagrangian methods or interior point methods [42]. As the target is to achieve a closest fit solution a gradient based approach is deemed appropriate as this would rapidly converge to a local minimum.

Sequential quadratic programming was selected, and it is the only in-built non-linear optimization function in GNU Octave. A black-box function is implemented to calculate the objective; squared error of the realized nodal locations of the thrust network with respect to the target geometry. Due to convergence problems non-negative constraint was not strictly applied and a small negative thrust in the order of 1/1000th of the largest thrust observed in the same iteration was allowed.

The gradient and Hessian matrices were numerically calculated within the built-in function in GNU Octave. However, Hiroki Tamai [43] has used analytical derivatives in optimization of problems involving force density method and notes the usage of analytical derivatives to be faster than numerical determination of derivatives (i.e. gradient and Hessian).

The performance of the optimization procedure is studied by considering the rate of convergence. Figure 3.13 present the progression of the optimization procedure and it is clear that the process rapidly converges to a local minimum. The optimum was reached at around the 30th iteration and the process continued as the convergence criteria was not met (default tolerance of *sqrt (eps)* = 1.4901e-008). The process terminated at 52nd iteration as the step size became very small. Figure 3.14 depicts the variation of the independent thrust densities as the optimization progressed. This shows that a stable value for force densities were reached at around 40th iteration. It is further interesting to note that while one independent force density reached a higher value than the initial estimate, all the rest reached a lower value than the initial estimate.

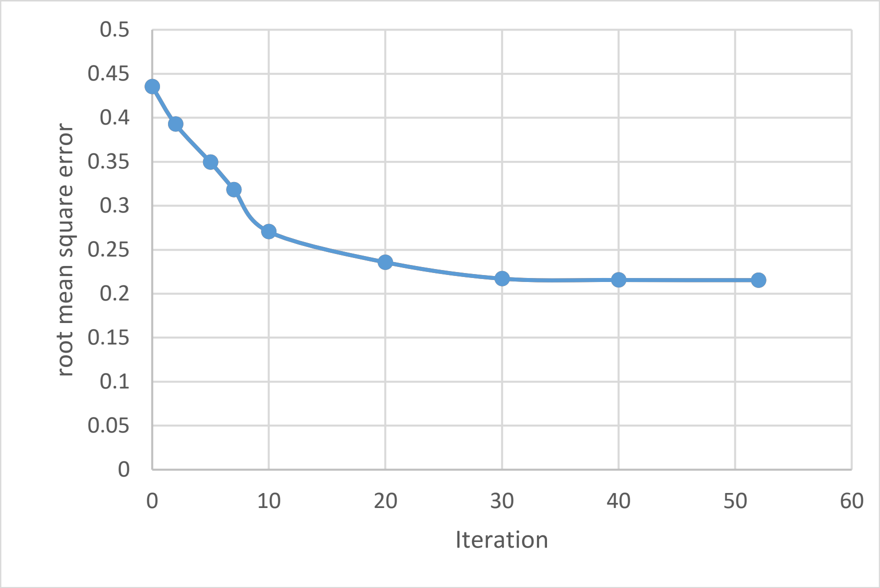

Figure 3.13: Error vs iteration plot for the optimization process to determine optimum force densities.

The initial target thrust densities influence the final solution as the sequential quadratic programming converges to a local minimum. The Voronoi dual lengths were used as the initial trial values for the thrust densities. Although this works with the regular quadrilateral thrust network used in the current example, there is no guarantee that (i) a dual Voronoi edge exist for every of branch of the thrust network, and/or (ii) the Voronoi dual lengths gives a close enough solution to the target to ensure convergence.

A more general approach is considering the centroidal dual of the form diagram [44]. Note that the branches of the centroidal dual are not necessarily perpendicular to the corresponding branches of the thrust network. As such the lengths extracted from the centroidal dual -in general- would not satisfy equilibrium. However, this was shown to work well as a starting point for the optimization problem and showed results consistent with the Voronoi dual approach.

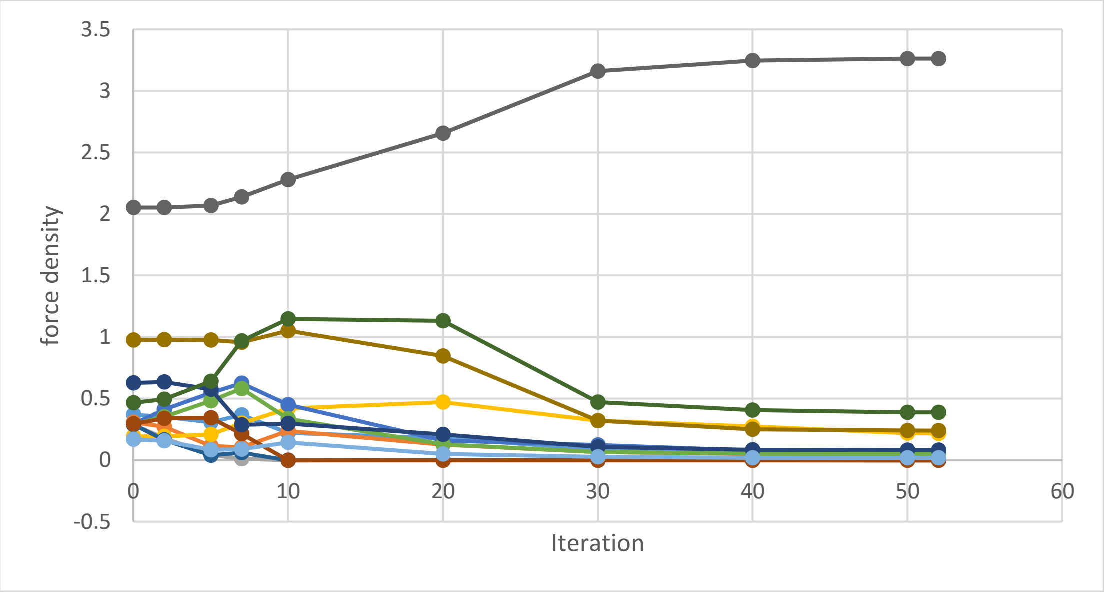

Figure 3.14: Variation of independent force densities as the optimization process progresses.

3.3.4. forcenetTNA

Once an appropriate set of force densities are selected “forcenetTNA” generates the force (dual) diagram. The process is straightforward, and a separate function is implemented to make it easier to update the thrust network if the user wishes to deviate from the optimum solution (determined in Section 3.3.3) for reasons such as better aesthetics or practical restrictions.

3.3.5. Solving for Vertical Equilibrium

The thrust network is now solved for horizontal equilibrium. In fact, it is solved for the vertical equilibrium as well when the optimum force densities were determined. However, solving for vertical equilibrium is implemented as a separate function to allow the user to deviate from the optimum solutions found earlier.

"optimScale" function solves for the vertical equilibrium and determines the optimum vertical scale which gives the closest fit thrust network to the target surface. This function is implemented so that the optimum scale can be determined under the set of independent force densities chosen by the user. "solheightTNA" determines the nodal heights under the force network (based on the optimum or chosen independent force densities) and the vertical scale factor (optimum or chosen). Both these implementations are straightforward implementations of the process noted in Section 3.2.2.

The graphical user interface of this implementation in GNU Octave is as shown in Figure 3.15.

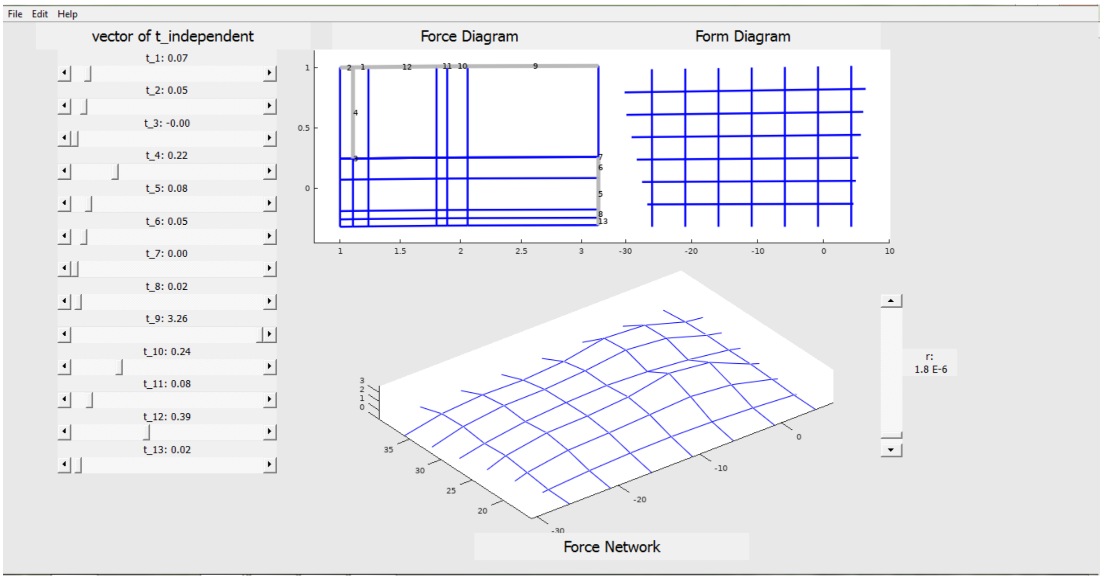

t_1: 0.07
t_2: 0.05
t_3: -0.00
t_4: 0.22
t_5: 0.08
t_6: 0.05
t_7: 0.00
t_8: 0.02
t_9: 3.26
t_10: 0.24
t_11: 0.08
t_12: 0.39
t_13: 0.02

r:
1.8 E-6

Figure 3.15: Current implementation of thrust network analysis for form finding and exploration of compression only structures, implemented in GNU Octave.

4. HORIZONTAL LOADING ON COMPRESSIVELY SELF-SUPPORTING FORMS

Seismic and wind action are considered the primary horizontal action on compressively self-supporting forms. The loading patterns used and the existing analysis techniques are first summarized. The application of these horizontal actions is first studied for simple arches and then extended to free-form compression-only structures. The aim of this study is not necessarily to introduce new analysis techniques but to introduce techniques to incorporate feedback on seismic and wind loading capacities of a structure at the form exploration stages. This is primarily to avoid costly rework to the initial schemes at later stages of design.

4.1. Seismic Loading

Safety of masonry structures under seismic action can be evaluated using either quasi-static or dynamic analysis. Quasi-static methods either ignore the dynamic effects entirely or compensate for them with a quasi-static loading. Although approximate, quasi-static analysis is a powerful and a practical approach for a preliminary assessment. As such quasi-static analysis is an appropriate tool to be merged with the form finding process to give feedback on seismic capacity while conducting a form exploration exercise.

In quasi-static analysis a constant horizontal acceleration is applied to the structure, along with the gravitational acceleration to account for the dead loading. This conservatively ignores the short period of application observed under a real seismic motion. Conversely, this ignores the possibility of resonant amplification and as such this method is appropriate when the elastic resonance is expected to have a relatively small effect. If the resonance effects play a larger role the horizontal force application should be distributed along the height of the structure with preference towards the top of the structure. The latter distribution can account for the amplification due to dynamic resonance effects [45].

4.1.1. Limit Analysis

As was discussed in Chapter 3, limit analysis is the most efficient way to assess the safety of an unreinforced masonry structure and remains the case under seismic loading as well. Tilt analysis is the most common practice of integrating gravity and quasi-static seismic loading in the assessment of masonry structures [46] [47].

Tilt analysis can be simply explained considering the stability of a masonry arch. Consider the original configuration of the arch given in Figure 4.1(a). The tilted arch in Figure 4.1(b) shows the original arch being tilted by an angle λ which is achieved by rotating the base line of the arch about an axis perpendicular to the plane. Now, in the tilted configuration the arch experiences a reduced acceleration in the original gravity direction (a_v) and an increased acceleration in the original horizontal direction (a_h). The tangent value of the tilt angle is equal to the ratio between the horizontal and gravitational acceleration.

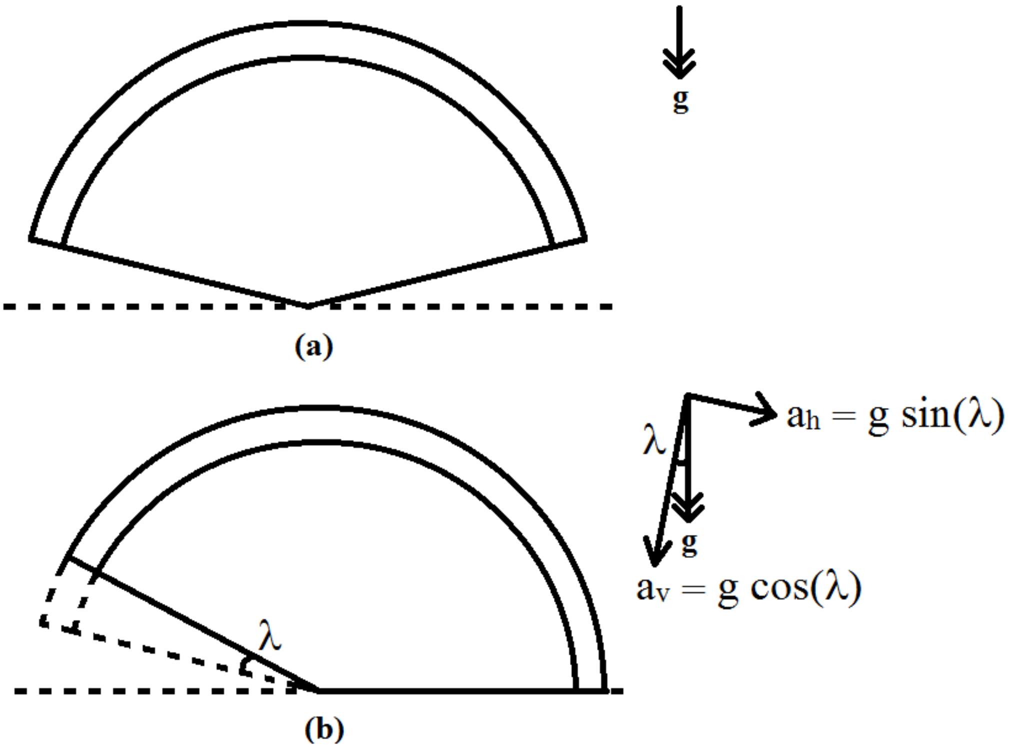

Figure 4.1: (a) Original and (b) tilted arch as considered in tilt analysis used with physical models.

Huerta [46] uses this method with a physical model and a hanging chain to conduct an approximate analysis. The shortcoming of this physical modelling is the reduction of the acceleration in gravity direction as the maximum resultant acceleration possible with a physical model is the gravitational acceleration.

A computational model can overcome this by prescribing the accelerations as required. Furthermore, it is the usual practice to prescribe the quasi-static loading as the force due to a horizontal acceleration given as some proportion of gravitational acceleration. This simplifies the tangent of the tilt angle as the value of the above proportion.

Ochsendorf [47] conducts an in-depth study on the stability of circular arches with an obtuse angle of embrace. The study considers the seismic loading capacity (characterised by the tilt angle) under varying thickness to radius ratios and angles of embrace. He considers the changes in the collapse mode with the above variations as well.

DeJong [45] conducted tilt analysis on a buttressed barrel vault with and without side isles and observed the change of seismic capacity with changing geometric parameters. He too observed the changes in the mechanisms with the changes in geometrical parameters.

Similarly, DeJong [45] and Ochsendorf [47] observed that the collapse mechanism changes with the geometrical configuration of the structure and in turn influences the seismic capacity of the structure. De Luca et al. [13] take a different approach and used a linear FEM to determine the appropriate collapse mechanism and conducted limit analysis on the mechanism found.

Michiels & Adriaenssens [48] used a procedure based on tilt analysis for the form finding of masonry arches, with consideration to in-plane earthquake loading. They further show that the arch profile determined by their procedure is more material efficient than a circular or a catenary arch, although other issues related to construction need to be addressed.

4.1.2. Three-dimensional Forms

Although straightforward, there was no evidence of titlt analysis being used in the analysis of unreinforced masonry structures under seismic loading. Michiels et al. [49] present a methodology based on dynamic relaxation. A complexity arising in the analysis of a non-symmetric three dimensional surface is the determination of the critical direction of loading.

The solution by Michiels et al. [49] results in shells of significant thickness. They note the possibility of constructing double shells with structural unity between the two shells. This brings about further issues relating to construction, and also the mechanism of shear force transfer between the two shells and requires extensive future work.

4.1.3. Thin Shell Concrete

It is important to note the influence of the availability of tension capacity in the earthquake resistance of shell structures. As Michiels and Adriaenssens [50] note, the high geometric stiffness and low mass of thin concrete shells results in high fundamental freequencies which are well above the driving freequencies of realistic seismic action. The high geometric stiffness is valid only if the structure remains within the elastic response and no tensile cracking occurs during the seismic response. They further explore the significane of geometric parameters on fundamental freequency and buckling behaviour of the shell.

4.2. Wind Loading

Wind loads are not the most critical loading encountered by early compressively self-supporting masonry structures, as corroborated by the lack of any evidence of collapse of masonry structures due to wind action. Coccia et al. [51] evaluated a Gothic Cathedral under wind loading based on limit analysis and determined a wind loading of 30m/s as the critical wind loading. However, the design based on gravity loads was sufficient, since the expected fierce wind speed with a 50-year return period was of 26 m/s. However, 3 second gust wind speeds suggested in codes of practices are much higher. The critical wind speed with a 50-year return period for Sri Lanka is given as 54 m/s, for the worst-case post-disaster structures in zone 1 [52]. Later studies have reaffirmed the usage of these high values for design of structures in Sri Lanka [53].

4.2.1. Wind Pressure Coefficients

Wind load on structures are calculated based on two sets of parameters; one on geometry and permeability of the structure and the other on the wind condition. Wind loading (equation 4.1) is dependent on q - the dynamic wind pressure based on the wind speed, adjusted for topography conditions, placement (immersion) of the structure with respect to the wind and probability of such a wind condition- and C_{pe}-

the external pressure coefficient which is based on the geometry of the structure- and C_{pi} - the internal pressure coefficient which depends on the permeability of the structure. The pressure coefficients (C_p) and the corresponding surface area (A) depend on whether the analysis is a global analysis of the structure or a local analysis of an element. Also, note that the wind force calculated (F_{wind}) acts perpendicular to the surface.

$$\mathrm{F_{wind}} = (\mathrm{C_{pe}} - \mathrm{C_{pi}})\mathrm{qA} \tag{4.1}$$

The variation of pressure coefficients along arched roofs (barrel vaults) and hemispherical domes were studied by various researchers (see Table 4.1).

4.2.1.1. Arched Roofs

The typical pattern of pressure variations for arched roofs as observed by Johnson et al. [54] is indicated in Figure 4.2. A peak positive pressure is observed in the windward front and pressures drop thereafter reaching a negative pressure peak near the crown of the arch – towards the windward side. The negative pressure drops off and flow separation occurs around 120^0 (see Figure 4.2.) and a small constant negative pressure is observed thereafter, due to wake suctions.

Table 4.1: Reference wind loading studies on curved profiles.

Author/ Year	Roof Geometry	Test type	Ground condition	Rise/Span
Johnson, G.L; Surry, D; Ng, W.K [54]	Arched Roofs	Wind tunnel Full scale model	Open country, suburban	0.27, 0.3, 0.37, 0.5
Abrahm et. al. [55]	Arched roofs	Wind tunnel	Open country, suburban	0.29
Blackmore, P. A; Tsokri, E [56]	Arched roofs	Wind tunnel	Open country	0.05, 0.1, 0.3, 0.5
Toy, N; Moss, W.D; Savory, E [57]	Hemispherical Dome	Wind tunnel	(Smooth and rough	0.5

			boundary flow)	
Taylor, T. J [58]	Hemispherical Dome	Wind tunnel	(Turbulent boundary flow)	1.0, 0.5, 0.3
Chang, C.N; Fu, C.L; Lin, Y.Y [59]	Hemispherical Dome	Wind tunnel	(Smooth flow) and suburban	0.5
Letchford, C.W; Sarkar, P.P [60]	Parabolic Dome	Wind tunnel	Open country	0.31
Rodrigues, A.M; Tomé, Ana; Gómes, M.G [61]	Free form	Computational Model	Open country	-

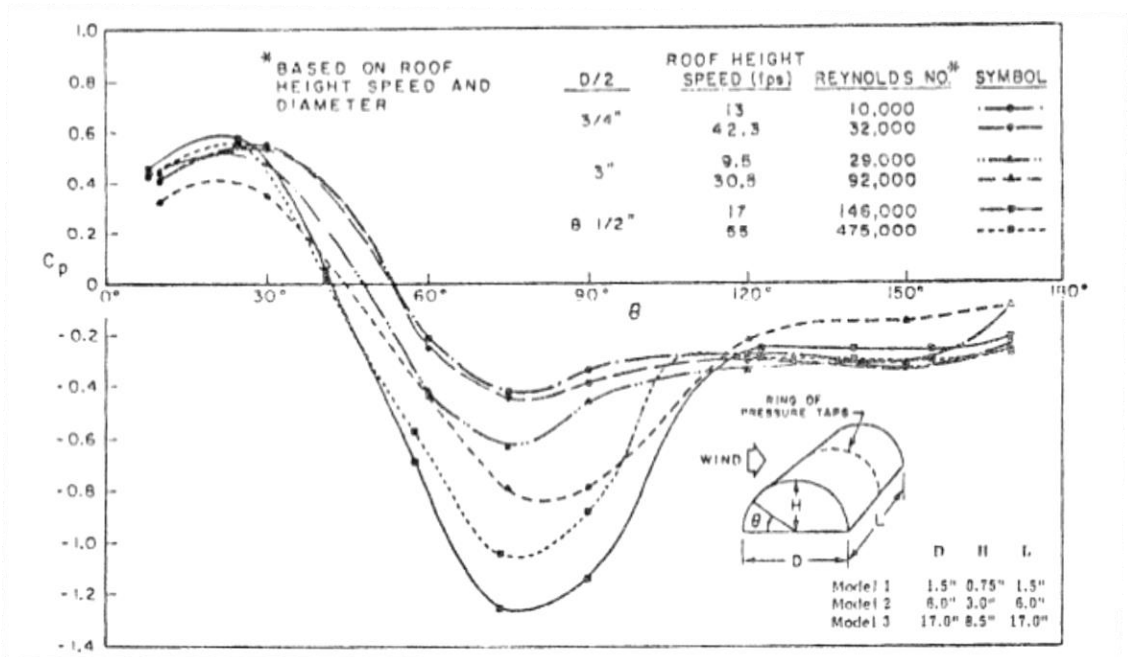

Figure 4.2: Circumferential pressure distribution on arch-roof models at various Reynolds numbers. Source: Figure 4 from Johnson et. al [54].

Abrahm et al. [55] additionally provide distributions of pressure coefficients for longitudinal (i.e. perpendicular to the plane of the arch) and quartering (diagonal) winds. Pressure coefficients due to longitudinal winds show a symmetrical pressure distribution with a single peak in the middle. The highest pressure is observed near the edge, and by the time it reaches a third of the length of the roof, pressure drops to almost zero. Quartering winds shows a behaviour similar to cross winds (i.e. parallel to the plane of the arch) in the windward half and shows higher negative pressures in the leeward half.

Johnson et al. [54] observe that the windward pressure, point of flow separation and wake suctions (i.e. leeward pressures) are Reynolds number independent, but the pressure peak near the crown is strongly Reynolds number dependent for $10^3 < Re < 475 \times 10^3$. However, for full scale tests ($10^4 < Re < 10^8$) the negative pressure peak is found to be Reynolds number insensitive and is consistent with the wind tunnel tests for $Re > 1.5 \times 10^5$.

Abrahm et al. [55] study the effect of side walls and conclude that the existence of side walls increases the suction values of mean pressure coefficients in all cases; and the magnitude of the increment increases with the sidewall height to span ratio.

Blackmore and Tsokri [56] have carried out an extensive study to determine the effects of different geometrical ratios (wall height to span -h/d, rise to span -f/d, and plan profile -L/b) on the area averaged pressure values. They conclude that the flow shows three-dimensional flow near the end sections and two-dimensional flow in the central section. By extension, shorter buildings (i.e. small L/b) would show overall three-dimensional flow behaviour. For a wind parallel to the eaves, the suctions near the windward edge decrease with rise to span ratio and suctions in the leeward end increase, but with a lower sensitivity.

4.2.1.2. Domical Roofs

Hemispherical domes are expected to show a pressure coefficient distribution in three-dimensions due to its doubly curved shape. Pressure distribution along the centre meridian (i.e. meridian parallel to wind direction) of the hemispherical roof is compatible with that of an arched roof, with similar pressure peaks and flow separation points. However, they show almost parallel isobaric lines (i.e. a two-dimensional behaviour) with some circular isobaric lines near the windward front and the crown (see Figure 4.3).

Cheng et al. [59] observe the negative peak pressure at dome apex to increase and the negative pressure in the wake region to decrease with increasing Reynolds number, when pressure distribution along the centre meridian is considered. However, the mean pressure coefficient contours are insensitive to Reynolds number beyond Reynolds number of 2 x 10^5 for smooth flow and 1 x 10^5 for turbulent flow. Taylor [58] notes that the pressure distribution is Reynolds number insensitive when Reynolds Number is greater than 1.7 x 10^5 for the turbulence intensity of natural winds (>15%). Maher [62] notes that surface roughness of the dome to be promoting a turbulent boundary layer, resulting in earlier separation of flow, which in turn results in reduced suction at the top of the dome and at the point of separation, and higher suction overall in the wake- i.e. reduced uplift and increased drag.

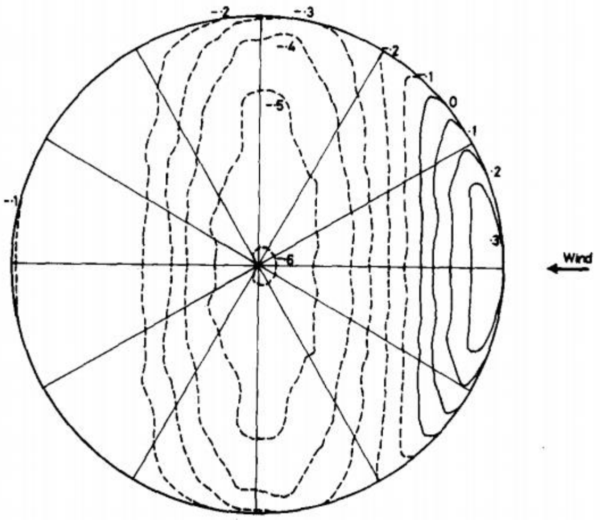

Figure 4.3: Isobaric lines over a rough hemispherical dome in a rough boundary layer. Source: Fig 5 from Toy et. al [57].

Taylor [58] studies the variation of pressure coefficients with changing height to diameter ratios (h/D) of spherical domes. It is observed that the pressure coefficients – both positive and negative- along the centre meridian decrease in absolute value as the height to diameter ratios decrease. Furthermore, the wind pressures along the meridian perpendicular to the wind direction show larger variations as h/D decreases, indicating a three-dimensional pressure variation.

Letchford and Sarkar [60] study the behaviour of parabolic domes under simulated atmospheric boundary layer in a wind tunnel. They indicate mean pressure coefficients compatible with spherical domes of corresponding rise to span ratios at the windward front and reduced suctions at the crown and the leeward front.

4.2.1.3. Free Form Structures

Rodrigues et al. [61] carried out a computational study on the wind loading on a free-form structure (Figure 4.4). The three-dimensional Computational Fluid Dynamic simulation was carried out with a hybrid structured-unstructured grid and the RNG k-ε turbulence model with non-equilibrium wall functions.

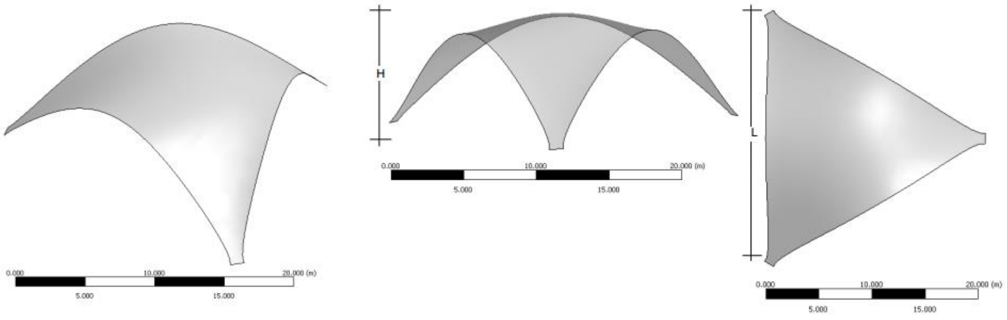

(a) isometric-view (b) front-view (c) top-view

Figure 4.4: Free form shell structure studied under wind loading. Source: Fig 1 from Rodrigues et al. [61].

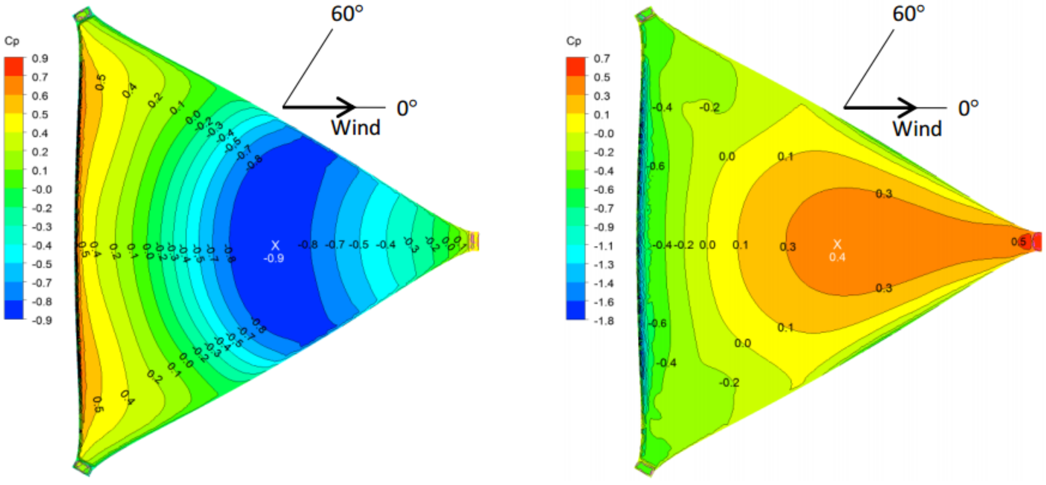

(a) Outer shell surface (b) Inner shell surface

Figure 4.5: Pressure coefficient contours for a wind incidence angle of 0°. Source: Fig 9 from Rodrigues et al. [61].

The structure was tested under two wind directions and the pressure coefficient distribution on the outer and inner surfaces are as given in Figure 4.5 and Figure 4.6.

The pressure coefficient pattern shows a variation similar to barrel vaults and domes with a high positive pressure at the windward front, peak suction at the crown and flow separation and hence low suctions along the leeward front. Note the presence of side bands in both inner and outer surfaces under the 60° wind direction.

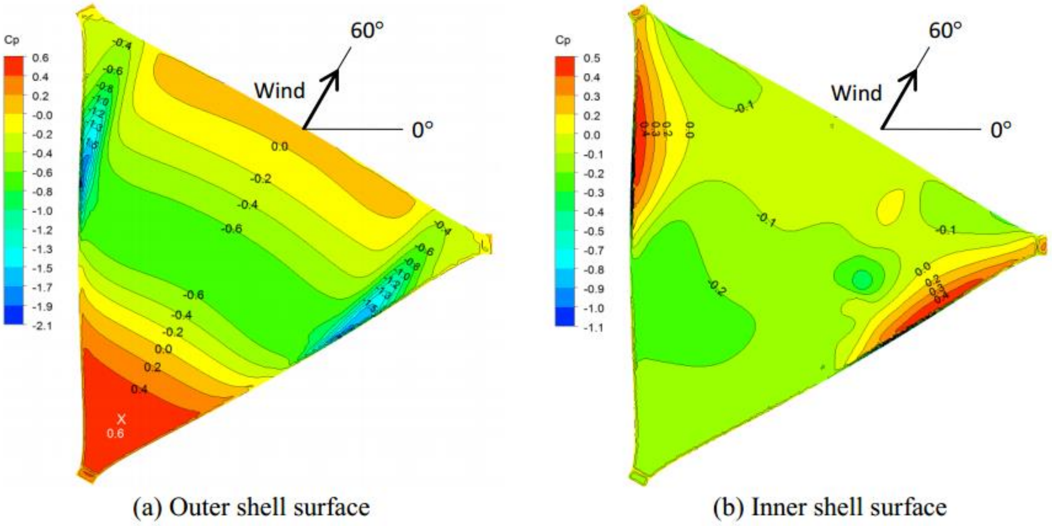

(a) Outer shell surface (b) Inner shell surface

Figure 4.6: Pressure coefficient contours for a wind incidence angle of 60°. Source: Fig 9 from Rodrigues et al. [61].

4.2.1.4. Recommendations in Codes of Practice

Both Eurocode (EN 1991-1-4:2005) and ASCE 7-02 provide guidelines on wind loading on arches and domes. Both guidelines consider wind loading on arches to be in three zones; windward quarter, centre half and leeward quarter. The pressure values are given as linear relationships with rise to span ratios. Eurocode recognizes the effect of sidewalls on the pressure at windward quarter and provides pressure coefficients for h = 0 and h/d > 0.5 with the option to interpolate intermediate values. Although ASCE guidelines recognize the difference between a roof on an elevated structure and that springing from the ground, they do not consider the effect of the wall height.

For spherical domes both the codes provide identical pressure coefficient variations with span to rise and support cylinder height to span ratios. Pressure coefficients are given for the windward tip, crown of the dome and the leeward tip, with isobaric lines perpendicular to the wind direction. Intermediate values are allowed to be interpolated.

4.2.2. Force Distributions

Forces exerted on arched roofs and domical roofs can be calculated by incorporating the pressure coefficients presented in Section 4.2.1.1 and 4.2.1.2 into equation 4.1. It should be noted that these forces act perpendicular to the roof surface and hence give rise to a horizontal and a vertical force distribution.

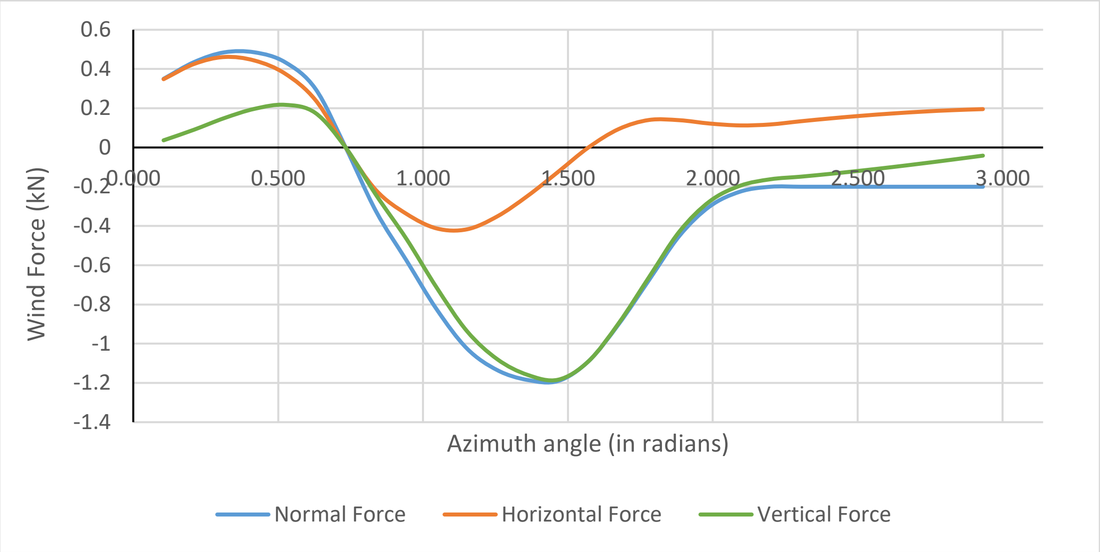

Figure 4.7: Separation of pressure coefficients, and hence the forces, to horizontal and vertical components.

Considering the typical pressure coefficient distribution observed in the central region of an arched roof and the central meridian of a domical roof, the normal, horizontal and vertical force distributions are as indicated as in Figure 4.7.

4.3. Feedback to Form Exploration on Horizontal Load Carrying Capacity

Considering the example of a two-dimensional arch under seismic loading we will first explore the possibility of providing feedback to the form exploration process on horizontal load carrying capacity of a compression only form. Using quasi static analysis to simulate seismic loading will result in a parallel set of loading from combined gravity and quasi-static seismic loading. This allows for the use of thrust network analysis, while maintaining its form exploration properties.

4.3.1. Seismic Analysis of a Two-dimensional Arch

It is assumed that the gravity loading is applied uniformly along the direction of the span, as opposed to uniformly along the arch. The latter would be a more accurate representation of the actual loading of an arch of uniform thickness, but the difference can be ignored for a preliminary form exploration exercise and for the range of rise to span ratios considered.

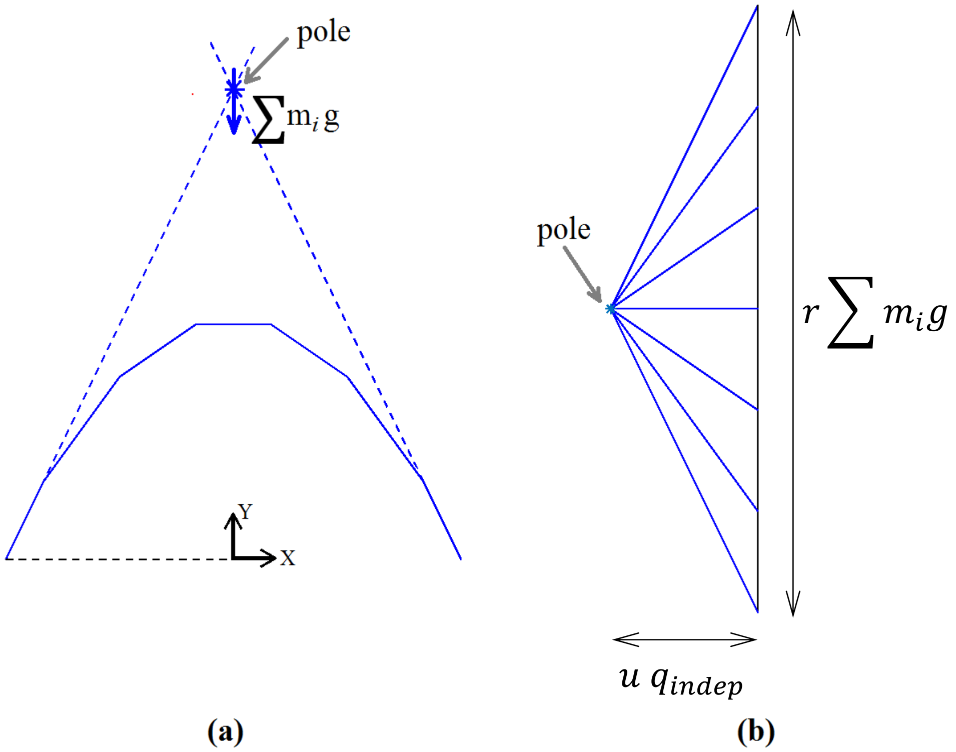

Figure 4.8: (a) Form and (b) force diagram for a compression only arch.

The form diagram for the arch (see Figure 4.8a) is made up of m members and n nodes with n_i ($[n-2]$) internal nodes. The corresponding force diagram is as shown in Figure 4.8b. Figure 4.8 clearly identifies the form exploration parameters r and q_{indep}, identified in Chapter 3 for the general case of three-dimensional forms. Note that this force diagram represents both horizontal and vertical forces as opposed to only horizontal forces in the form diagram mentioned in Chapter 3. It is possible to show the vertical forces also as the arch is considered a two-dimensional form and not a three-dimensional form. Furthermore, there is only one value in vector q_{indep} – thus inconsequential as a form finding parameter.

Tilt analysis and closest fit form

As discussed in Section 4.1, it is common to represent the quasi static seismic loading as an acceleration coefficient – a multiplier to gravitational acceleration ([47], [45]).

Now each element –mass m_i - in the arch would be subjected to a horizontal acceleration $a_v g$ (from seismic loading) and a vertical acceleration g (from gravity) and the resultant loading on the arch would be parallel to each other and would be in the direction of the resultant acceleration (i.e. vector sum of gravity and seismic acceleration – see Figure 4.9).

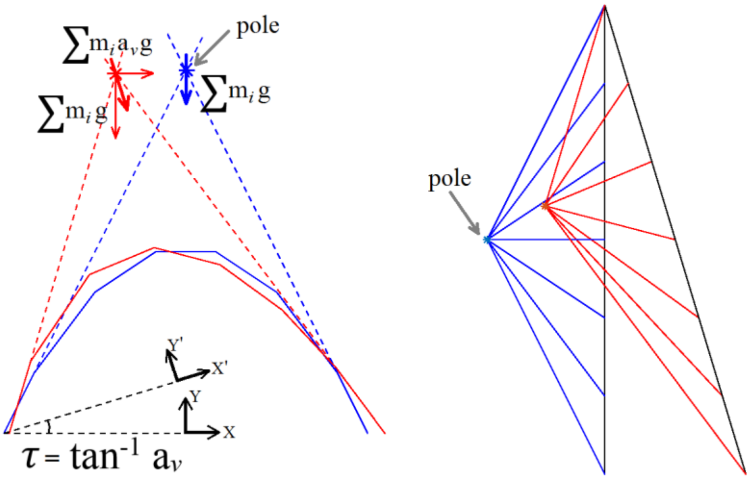

(a) **(b)**

Figure 4.9: (a) Thrust line for a gravity loading uniformly distributed load along the X -direction (blue) and gravity loading combined with horizontal loading due to a horizontal acceleration of a_v with (b) corresponding force diagrams.

To keep the advantages of the thrust network analysis the axis system is rotated by an angle τ (equation 4.2) such that the loading is parallel to Y' axis and perpendicular to the X' axis (see Figure 4.9). Nodal coordinates were converted to the new axis system using equation 4.3. Both horizontal and vertical equilibrium are solved for in the X'-Y' axis system and the solution is then returned to the original system of axis using the inverse relationship of equation 4.3.

$$\tau = \tan^{-1} a_v \tag{4.2}$$

$$\begin{bmatrix} X' \\ Y' \end{bmatrix} = \begin{bmatrix} \cos\tau & \sin\tau \\ -\sin\tau & \cos\tau \end{bmatrix} \begin{bmatrix} X \\ Y \end{bmatrix} \tag{4.3}$$

As mentioned earlier the user will carry out the form exploration exercise under gravity loading only and seismic analysis will provide feedback. Hence, instead of allowing for form exploration under combined gravity and seismic loading (using parameter r), vertical equilibrium equation 3.13 is solved using Moore-Penrose pseudoinverse to find the closest-fit form of the thrust line (under combined gravity and seismic loading) to the form of the thrust line found under gravity only loading condition. This solution shall be referred to as the closest fit thrust line in the remainder of this thesis.

The set of possible values for $\begin{bmatrix} z \\ r \end{bmatrix}$while satisfying equilibrium will be in the null space of $[D \quad p_z]$ (equation 4.4a). From this infinitely many possibilities, one solution can be obtained by multiplying the basis vectors of the null space by a coefficient vector α (equation 4.4b). Since we have a set of known values (z_{target}) for the height of the nodal locations (i.e. the form found by manipulation under gravity loading only) we can attempt to find α_{sol} which is closest-fit to our target form (equation 4.4d). It is evident that the first $n-1$ rows of the null space vector (ψ_{n-1}) do not give a square matrix and as such an inverse does not exist. We can use the Moore-Penrose pseudo-inverse instead [34]. It can be proved that the result from Moore-Penrose pseudo inverse gives the least squares solution for a system of linear equations [37] . Now the closest fit $\begin{bmatrix} z \\ r \end{bmatrix}$can be found as the corresponding coefficient vector (α_{sol}) is known.

$$\psi = \text{null}([D \quad p_z]) \tag{4.4a}$$

$$\begin{bmatrix} z \\ r \end{bmatrix} = \psi\alpha \tag{4.4b}$$

$$z_{target} = \psi_{n-1}\alpha \tag{4.4c}$$

$$\alpha_{sol} = [\psi_{n-1}]^{-} z_{target} \tag{4.4d}$$

$$\begin{bmatrix} z_{sol} \\ r_{sol} \end{bmatrix} = \psi\alpha_{sol} \tag{4.4e}$$

Corrections to the least squares form fitting

As the above procedure is done in the X'-Y' axis system the above error minimization is done in Y' direction (see Figure 4.10). The optimal solution will be given by minimizing the error in the direction of the arch thickness. This can be done by introducing a weights matrix to the Moore-Penrose pseudo-inverse (i.e. weighted least squares approach).

At an internal node, it can be shown that the error in Y'direction (e) is related to the error in thickness direction (e_t) as given in equation 4.5. The parameters used are as shown in Figure 4.10. For 1st and nth nodes (i.e. the boundary nodes) $[\theta_i + \Delta\theta_i]$ shall be taken as $\theta_1$and θ_m, respectively.

$$e_t = e\cos(\tau - [\theta_i + \Delta\theta_i]) \tag{4.5}$$

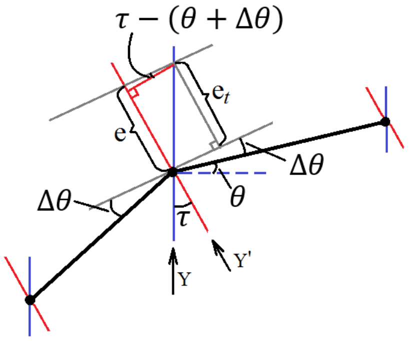

Figure 4.10: Correction of the error in least squares minimization to the direction of the thickness.

Moore-Penrose pseudo inverse with weight function is as in equation 4.6 where superscript '+' represents the pseudo-inverse, and matrix W is the weight function (matrix). The diagonal elements of the weight matrix w_{ii} is as given in equation 4.7. All the off-diagonal elements are set to zero. A close observation shows that changes to the position of first interior nodes (2nd and n-1th) will influence the thickness at the springing. However, this relationship is non-linear, but because of the preliminary nature of the form finding exercise, this effect is ignored.

$$A^+ = (AWA^T)^{-1}A^T\mathrm{W} \tag{4.6}$$

$$w_{ii} = \cos(\tau - [\theta_i + \Delta\theta_i]) \tag{4.7}$$

Observations

An arch of 8m span subjected to a uniformly distributed loading of 1kN/m was considered for the following study. The results are invariant of the span and the loading intensity. The choice of the number of members (m) is important as the accuracy of the catenary form increases with the number of elements. The arch was discretized to 30 members noting that beyond $m = 20$ the significance of m diminishes (2%

difference in pole location for $m = 10$ and 15, with the same being 0.4% between $m = 20$ and 25, and 0.1% between $m = 30$ and 35).

Two distinct patterns were observed of the closest-fit thrust line when the horizontal acceleration was increased gradually. Under least squares fitting the closest-fit thrust line had two regions of minimum error, around a third the way between the springing and the crown of the arch. And a region of maximum error was observed between the above minimum regions and the crown of the arch (see Figure 4.11). This observation is consistent with the optimum arch profile proposed by Michiels and Adriaenssens [48].

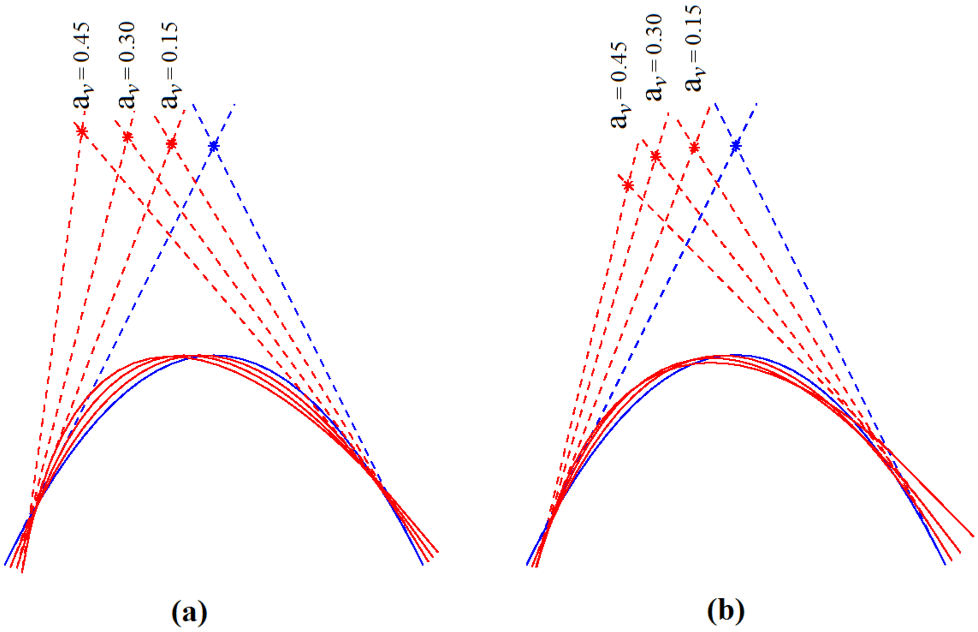

Figure 4.11: Thrust lines under quasi-static seismic loading with (a) least squares approximation and (b) weighted least squares approximation to correct the error measurement.

Under the weighted least squares method, the maximum error region was observed near the springing. There is a constructional advantage in this as the arch can be built of a smaller uniform thickness with a bulked-up region near the springing (see Figure 4.12). It should be noted that the thrust lines shown in Figure 4.12 does not correspond to the arch profile indicated in the figure – it is only a proposed arch profile based on the thrustline. The bulking shown can be further optimized since the increased loading due to thickening will deflect the thrust line inwards allowing for a further reduction in the thickness. This optimization is not carried out in the current study as the load distribution assumed in this preliminary form exploration is only approximate and any optimization based on the same is not realistic. It should be noted that at lower rise to span ratios the least squares results give maximum errors near supports and as such that too could benefit from bulked springing.

It was further observed that least squares solution gives the minimum thickness (out of the two methods) at higher rise to span ratios combined with higher horizontal acceleration (i.e. rise/span > 0.45 and ag > 0.25) while at lower rise to span ratios and/or lower horizontal accelerations weighted least squares gives the minimum thickness.

Comparison of area of arch cross-sections obtained by having a uniform arch or a bulked springing was compared with results from Michiels and Adriaenssens [48]. With respect to material demand, the proposed arch profile in [48] is superior to the uniform arch with bulked springing presented here but is inferior in practicality of construction due to the varying arch thickness. It should be noted that what Michiels and Adriaenssens [48] present is a design procedure whereas the current presentation is a feedback procedure on form exploration.

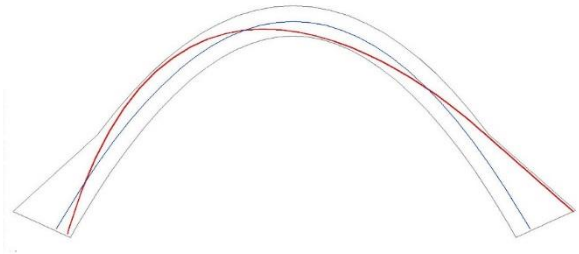

Figure 4.12: Proposed form for a uniform arch profile with bulked springings. Blue thrust line is under gravity loading and red thrust line is under combined gravity and seismic loading.

Presentation of feedback to the form exploration procedure

The procedure presented in above was implemented with a graphical user interface (GUI) in GNU Octave software package (see Figure 4.13). It allows form exploration with the rise to span ratio of the arch while giving as feedback the minimum thickness requirement for a selected horizontal acceleration coefficient and a minimization procedure (least squares or weighted least squares).

Considering the general nature of the results, it is possible to summarize them in a graphical format. Miciels and Adriaenssens [48] denote the point of the force diagram where all the thrust forces meet as the pole of the force diagram (Figure 4.9b). Similarly, a pole can be defined for a form diagram as the point where the lines of action of the support reactions meet (Figure 4.9a). The resultant of the external loading will also pass through this pole.

A plot was generated based on the poles (of the form diagram) of thrust lines for an arch under uniformly distributed loading with varying rise to span ratios and their corresponding closest-fit thrust lines under varying horizontal accelerations (see Figure 4.14). The contours correspond to the minimum thickness requirement for an arch of uniform thickness and unit half-span. The minimum thickness requirement presented here is the smallest of thickness requirements given by least squares and weighted least squares solutions.

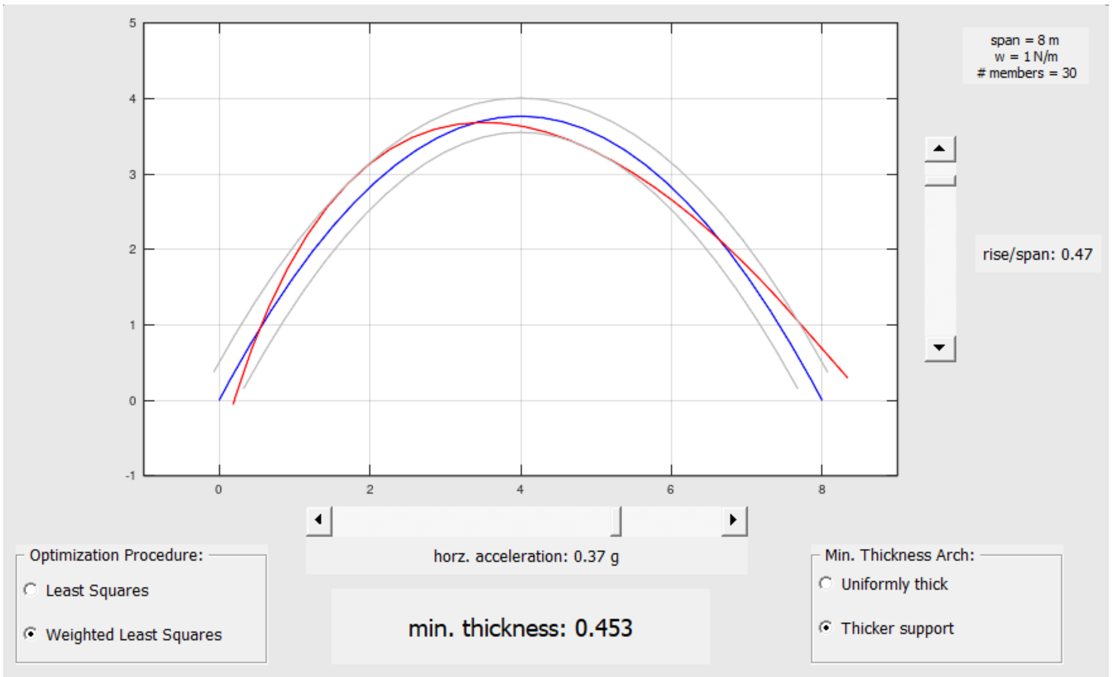

span = 8 m
w = 1 N/m
# members = 30

rise/span: 0.47

Optimization Procedure:
○ Least Squares
● Weighted Least Squares

horz. acceleration: 0.37 g

min. thickness: 0.453

Min. Thickness Arch:
○ Uniformly thick
● Thicker support

Figure 4.13: GUI of GNU Octave implementation of feedback procedure for form-finding of arches.

The limiting horizontal acceleration ($a_{v,lim}$) for each rise to span ratio was determined considering the tilt angle (τ) and the slopes of the support reaction under gravity loading. Tilting the arch to the corresponding limiting tilt angle would make the longitudinal axis of the voussoirs at the springing stand vertical.

This plot can also be extended to be used as part of a graphic static procedure by introducing a horizontal line corresponding to a unit half-span.

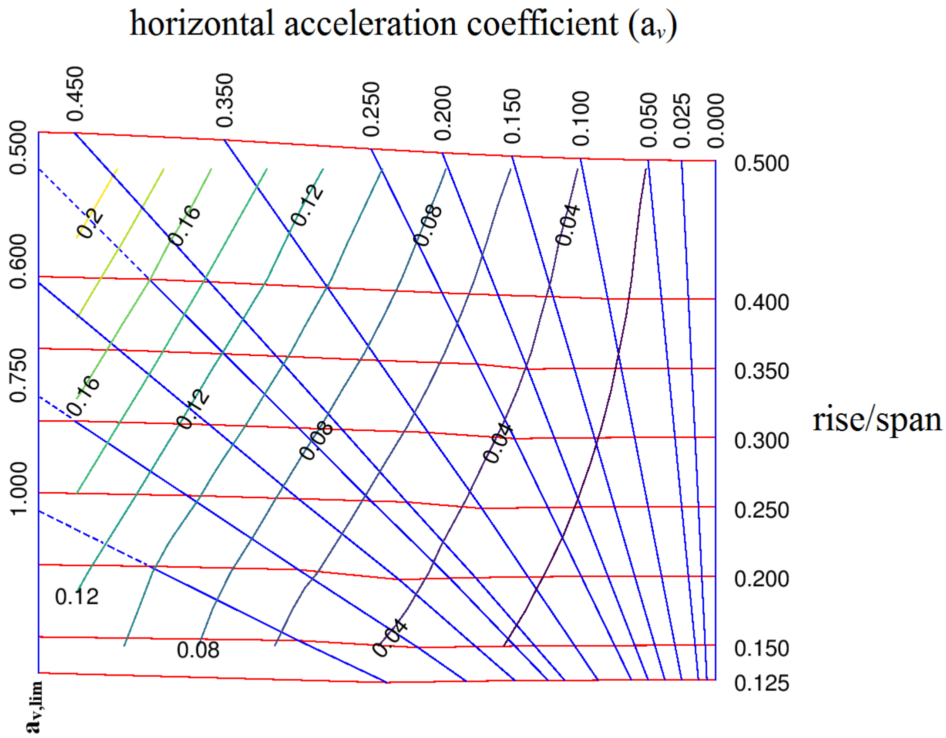

Figure 4.14: Minimum thickness contours under varying rise to span ratios and horizontal acceleration coefficients. Magnitude of contours correspond to an arch of unit half span.

4.3.2. Seismic Analysis of Three-dimensional Forms

A similar procedure as employed for the two-dimensional arch was carried out on a three-dimensional free-form roof supported on four edges (see Figure 4.16). The procedure needs some adjustment with the presence of the additional spatial dimension.

The three-dimensional form (given that the form diagram has more than one state of self-stress) has the parameter q_{indep} as another form exploration parameter. Hence a non-linear optimization procedure (equation 4.8) was employed to find the optimal choice of q_{indep} that would give the closest fit form with the smallest maximum error (i.e. the local thickness of the shell).

$$\min_{q_{indep}} Z_{err} \ s.t. \{q > 0\, ; where\ Z_{err} = \begin{cases} \max\left(\left|z_i - z_{target,i}\right|\right) \\ \sqrt{mean((z_i - z_{target,i})^2)} \end{cases} \qquad (4.8)$$

The objective of the minimization procedure can be set as the minimization of the maximum absolute error or root mean squares error. The former would be preferred in the case of a shell of uniform thickness and latter if the shell thickness is allowed to vary. Furthermore, as discussed earlier for arches, this error could be either in the loading direction (least squares solution) or in the thickness direction (weighted least squares solution).

The code was implemented in GNU Octave open-source computation platform, and the Sequential Quadratic Programming (SQP) tool available in the program was used for the optimization problem. This is the only optimization tool available in the software package and it worked well for the test case. The extended implementation of TNA with feedback on earthquake loading capacity is given in Figure 4.15.

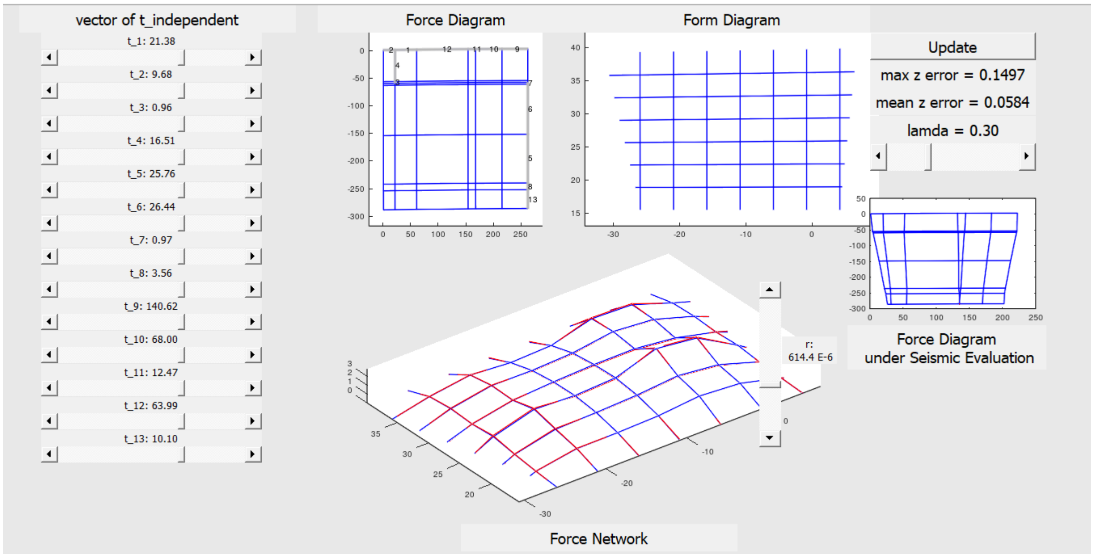

t_1: 21.38
t_2: 9.68
t_3: 0.96
t_4: 16.51
t_5: 25.76
t_6: 26.44
t_7: 0.97
t_8: 3.56
t_9: 140.62
t_10: 68.00
t_11: 12.47
t_12: 63.99
t_13: 10.10

max z error = 0.1497
mean z error = 0.0584
lamda = 0.30

Figure 4.15: GUI of TNA implementation for 3D free-form structures with feedback on seismic loading capacity.

In the current example the target free-form is discretized to a thrust network of 97 members connected at 42 nodes. Thirteen (13) modes of self-stress were identified, which result in thirteen (13) independent elements in t. The quasi static seismic loading considered correspond to a horizontal acceleration coefficient of 0.3 in the direction indicated in Figure 4.16b. The corresponding thrust networks under gravity and the combined loadings are given in Figure 4.16b.

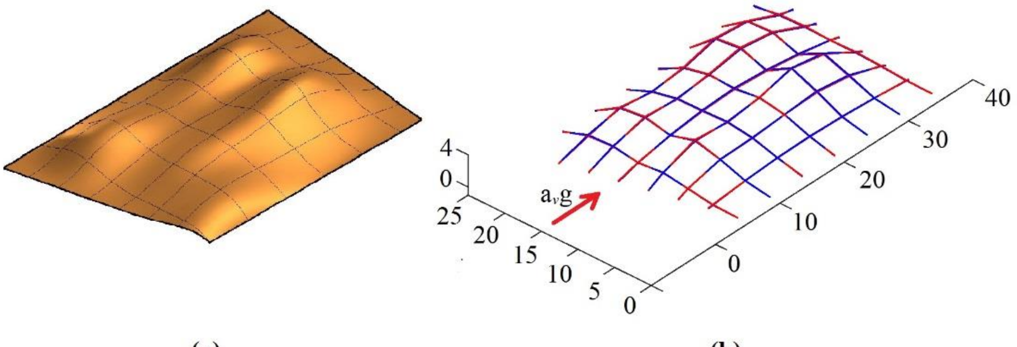

(a) **(b)**

Figure 4.16: (a) Target free form supported at all four edges and (b) the corresponding thrust network under gravity loading (blue) and combined gravity and quasi-static seismic loading (red).

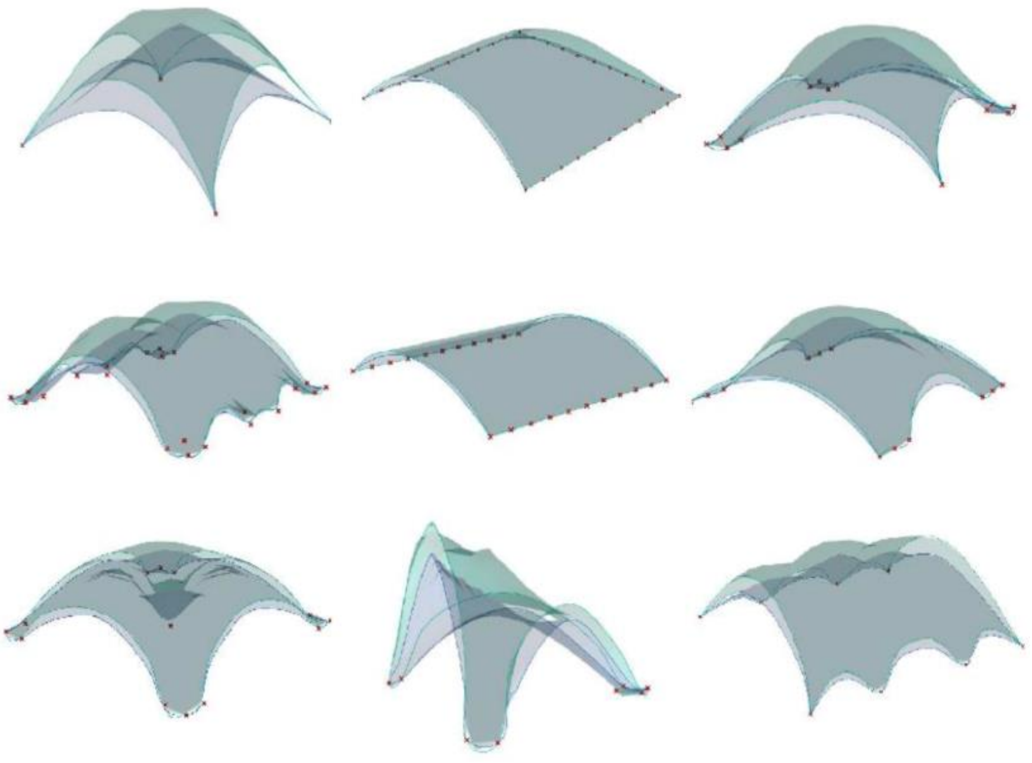

Figure 4.17: Envelope of thrust networks for a compression-only shell subjected to a horizontal acceleration of 0.3g. Source: [49]

The maximum Z_{err} for this example was 0.29 m which in comparison to the maximum span of 37 m and maximum rise of 3.8 m is very small (0.7% and 7% respectively). These thicknesses are negligible in comparison to the forms found by Michiels et al. [49] using dynamic relaxation method (see Figure 4.17). The advantage of having thicker supports under this method can also be seen, whereas in [49] the larger thicknesses are observed away from the supports.

Plots similar to that presented in Figure 4.14 can be developed for three dimensional forms. These can be useful for geometric shapes (e.g.: spherical domes, barrel vaults) but their usefulness for free-forms are questionable. The plots in effect would be three dimensional as horizontal acceleration should be considered from all horizontal directions (except for spherical domes, where axisymmetry would allow for summarizing the results in a two-dimensional plot).

4.3.3. Wind Analysis of Two-dimensional Arches

As discussed in section 4.2.1 wind loads act perpendicular to the surface. Thus, tilt analysis is not a viable option in analysing compression only forms under wind loading. Instead, a process which simultaneously updates the form and force diagram was implemented to analyse the two-dimensional arch under wind loading. A least squares minimization is implemented to determine the closest fit thrust line under the wind loading.

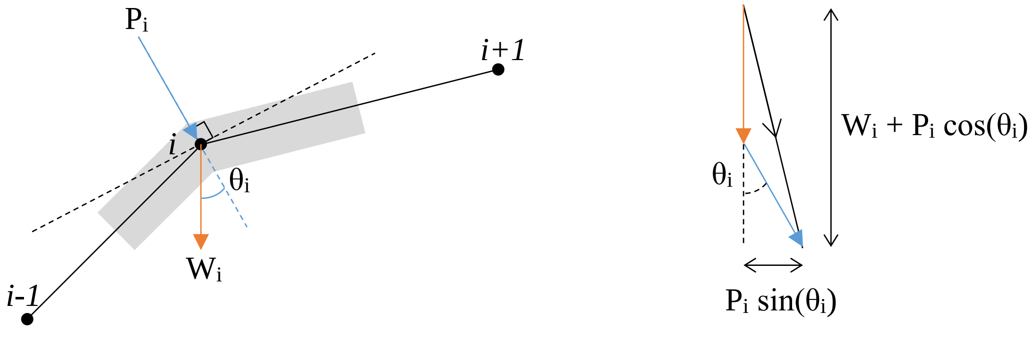

(a) Form Diagram (b) Force Diagram

Figure 4.18: Partial form and force diagrams indicating the gravity and wind loading on one element of the block.

The process implemented is as follows: First, the external forces on the arch were calculated at nodal locations (i.e. on the form diagram). The external forces include gravity loading (W) and wind loading (P) lumped at nodal points (see Figure 4.18). As evident from Figure 4.18 the wind load is applied perpendicular to the average slope trajectory of the two form branches connecting the corresponding node.

Then, using the forces and their directions determined in step 1, the base of the force diagram was drawn (i.e. represent all the external loads in the force diagram). A position for the pole of the force diagram was assumed. This is equivalent to assuming a scaler ‘r’ for the force diagram. And thus, the force diagram was completed with the assumed scaler ‘r’.

Next, the form diagram was completed considering (i) the duality between force and form diagram, and (ii) the lines of action of the external loading on nodes. This amounts to determining the new nodal points for the line of thrust under the combined gravity and wind loading. The new nodal point should be on the line of action of the combined gravity and wind loading on the node and the directions of thrusts on the node should is given by the force diagram completed in 3 above.

The least squares error of the nodal locations under combined gravity and wind loading was calculated, with reference to that under gravity loading only. Currently this is implemented as an unweighted least squares problem, without considering the error in thickness direction. This has shown to work well with the optimization procedure in step 6. However, the final output of thickness demand is calculated based on error between the two thrust lines (gravity only and gravity with wind) in the thickness direction.

The above steps were repeated with a new scalar *r* until the least squares error is minimized. The scaler r corresponding to the minimum error was used to determine the line of thrust and the minimum thickness requirement. ‘fminsearch’ MATLAB [63] tool was used for the optimization in the current implementation. As was obvious from the force and form diagrams, there is always a least squares solution and it is a straight forward optimization and ‘fminsearch’ works well with this simple optimization problem.

The above procedure was tested under a uniform wind pressure ‘p’ acting perpendicular to the arch of span ‘L’ and rise ‘R’. Figure 4.19 and Figure 4.20 show the force and form diagrams under a uniform wind pressure, with varying scaling factors: Figure 4.20 gives the closest fit solution to the thrust line under gravity loading only.

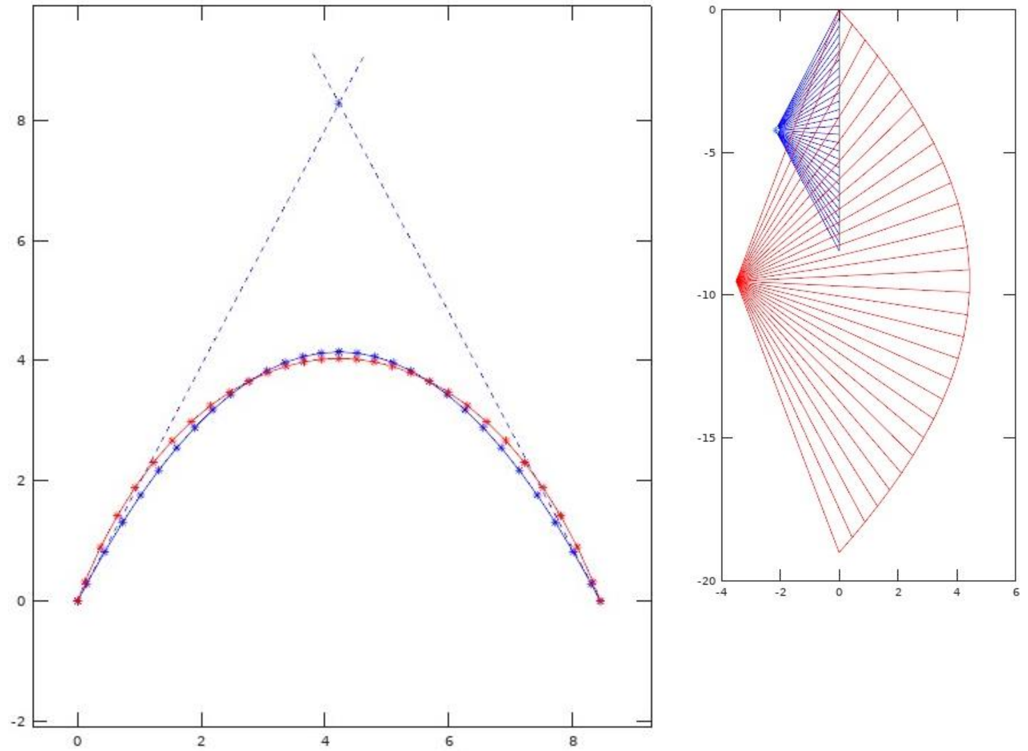

Figure 4.19: Form and Force diagrams under combined gravity loading ‘W’ and uniform wind pressure ‘p’. Scalar r =1, arch span ‘L’, rise ‘R’. Diagrams in blue indicate gravity load only condition, while diagrams in red indicate combined gravity and wind load condition.

An arch of 8.1 m span, 4.0 m rise, 1.0 m width and 0.3m thickness was analysed under a typical wind loading pattern as observed in section 4.2.1. The selected dimensions for a masonry arch results in an approximate self-weight of 6 kN per meter length of span. The wind condition considered (see Figure 4.21) is a design wind speed of 55 ms^{-1} (considering west coast of Sri Lanka [64]), giving a dynamic wind pressure of approximately 1.85 kN/m^{2}, in accordance to BS 6399-2 [65]. Figure 4.22 presents the force and form diagrams under gravity and combined gravity and wind loading. The closest-fit form diagram (i.e. combined gravity and wind loading) is indicated in red.

For the above-mentioned arch, design wind speeds of 30 ms^{-1} and 55 ms^{-1} demand a minimum thickness of 50mm and 220mm, respectively. Both maximum thickness demands are within the assumed arch thicknesses of 300mm and is at the windward front. The arch would perform satisfactorily for a seismic loading of 0.25g magnitude, acting along the plane of arch. Note that this analysis starts with an assumed thickness of the arch and the purpose of this tool is to give feedback to drive the form exploration process. We next discuss below how an invalid solution would occur and how to drive the form exploration process to rectify the lack of stability under wind loading.

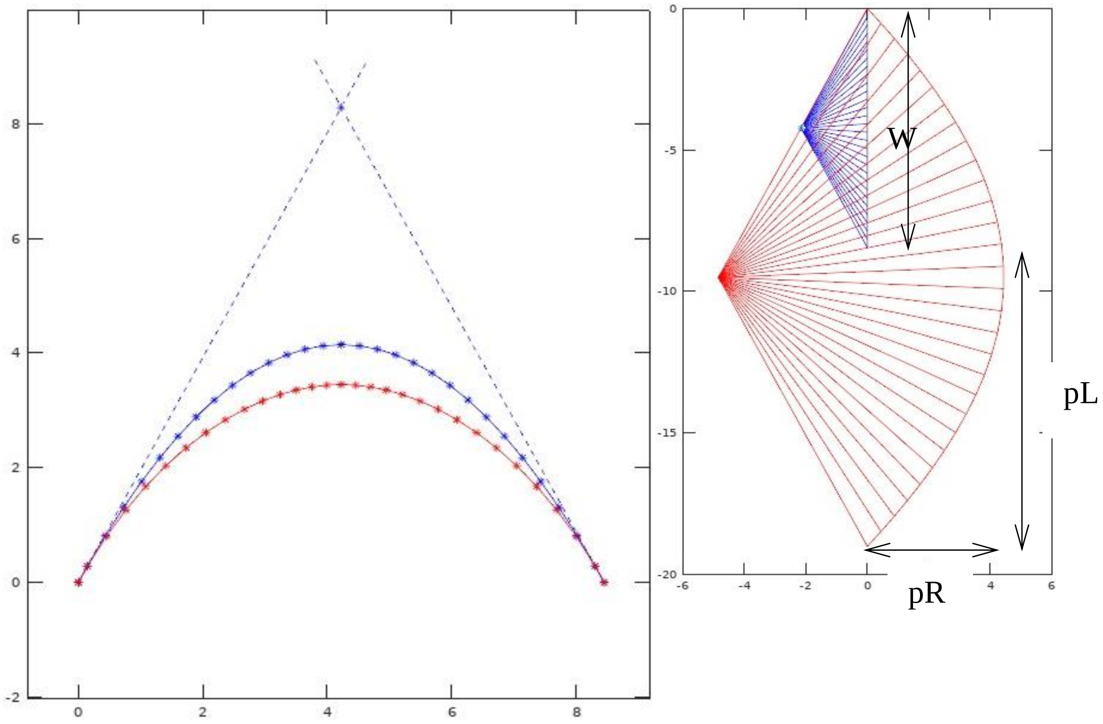

Figure 4.20: Form and Force diagrams under combined gravity and uniform pressure loading. Scalar r =0.31 giving the least squares error. Diagrams in blue indicate gravity load only condition, while diagrams in red indicate combined gravity and wind load condition.

A key observation of this study is that not all the possible scaling factors – r – give a valid compression only solution. This is due to the nodal loads – combined gravity and wind- not being parallel to each other, and thus their lines of actions intersect (see red dashed lines in Figure 4.23). This could result in some candidate thrust lines violating the compression only condition of the thrust line, even if the thrust line is within the arch cross-section.

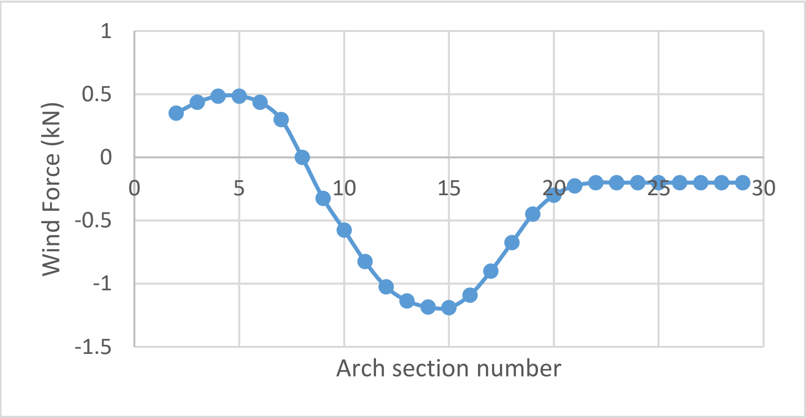

Figure 4.21: Nodal wind loads for the arch in Figure 4.22, considering a design wind speed of 55ms^{-1}.

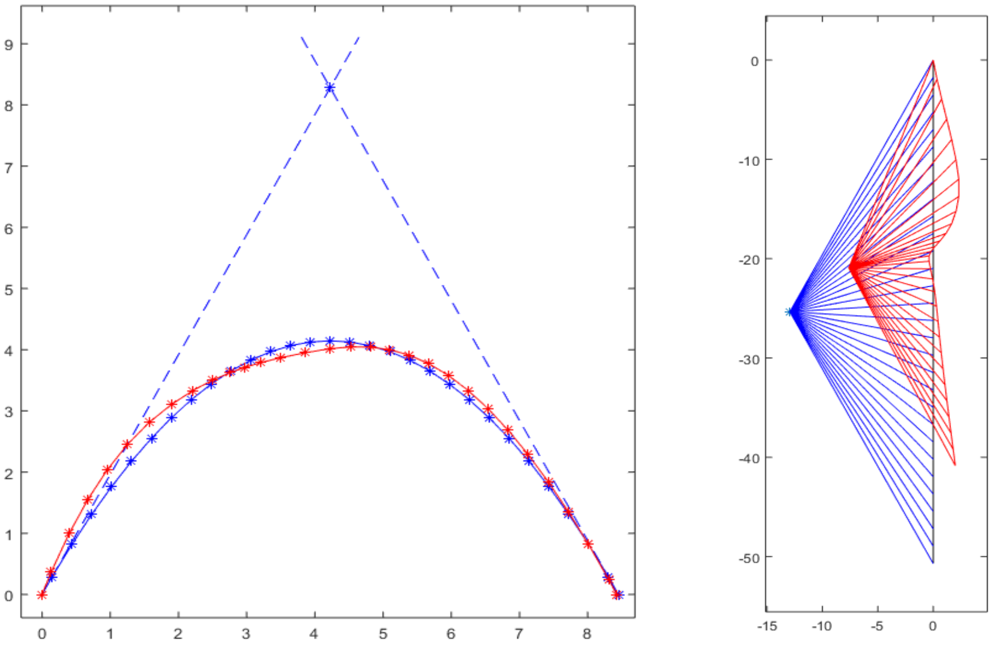

Figure 4.22: Form and Force diagrams under combined gravity and a typical wind pressure loading. Scalar r =2.36 giving the least squares error. Diagrams in blue indicate gravity load only condition, while diagrams in red indicate combined gravity and wind load condition.

The inset Figure 4.23 show a series of consecutive nodes on thrust line III. It shows that the block representing node *i* will be 'pushed' (i.e. a compressive force) from the block representing node *i+1* and will be 'pulled' (i.e. a tensile force) by the block representing node *i-1*. However, the interface between the two blocks *i* and *i-1* is not capable of exerting a tension and thus would likely lead to the collapse of the arch by the displacement of the block representing node *i*. However, an experimental observation would be required to definitely identify the associated collapse mechanism.

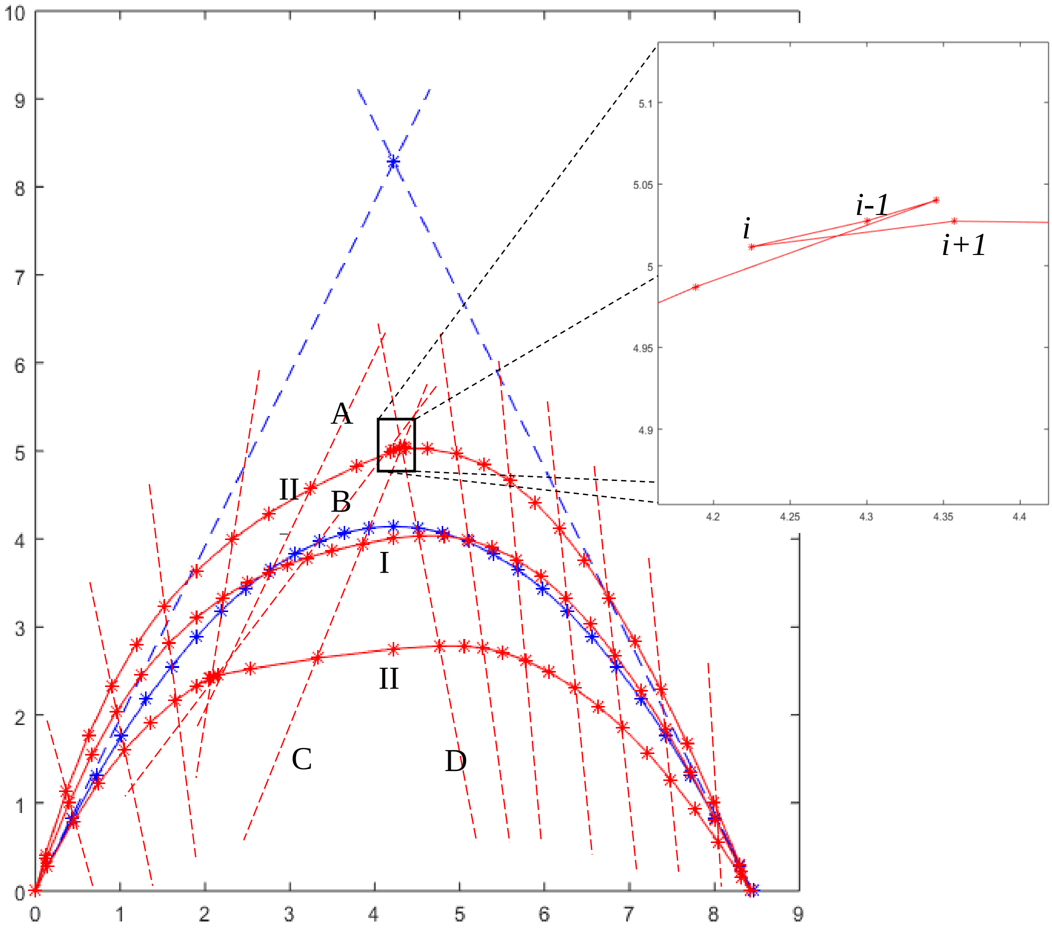

Figure 4.23: Candidate thrust lines (in red) for an arch under combined gravity and wind loading, with corresponding gravity only thrust line (in blue).

A closer observation of Figure 4.23 shows that such ‘looping’ thrust lines will occur if any node of the thrust line lies outside of the region where no two lines of action of nodal loads intersect. Thrust line III is just above the point where lines of action C and D have crossed and thrust line II is just below the point where lines of action A and B have crossed. Both lines of thrust II and III have loops and are thus invalid. Thrust line I is within the region where no lines of actions are intersecting and is indeed a valid thrust line.

This could result in the closest fit solution being invalid at higher wind loads, and in some cases no valid solution exists- e.g. a design wind speed of 75ms^{-1} for the arch considered earlier. In such cases a safe solution can be achieved by increasing the arch thickness and hence increasing the gravity loading on the structure – e.g. increase the thickness of the arch to 0.45m to be safe at a 75ms^{-1} wind.

5. CONCLUSIONS AND RECOMMENDATIONS

5.1. Conclusions

1. A rich tradition of building compression-only forms as an efficient structural system has been observed from as early as 3000BC to date. Evidence of this tradition can be observed across the world, including in Sri Lanka. Analysis of arches, vaults and domes have seen many improvements through the years with Maxwell's observation and Heyman's safe theorem being seminal works. Thrust Network Analysis presented by Block and Ochsendorf (2007) is identified as a key tool in form-finding and form-exploration of compression only forms, used today. This is considering its versatility and wide-spread use by fellow researchers in the 'shell structures' community.
2. Thrust Network Analysis was implemented in GNU Octave and MATLAB platforms with improvements to the original implementation by Block and Ochsendorf (2007). The process was extended to give feedback on the lateral load carrying capacities of compression-only structures.
3. Real-time feedback can be provided to the form exploration process on the thickness requirements of compression-only forms (arches to free form shells) under quasi-static seismic loading. The proposed procedure employs Thrust Network Analysis with Moore-Penrose pseudo-inverse to find the least squares closest-fit form. For forms which could be defined geometrically (e.g. parabolic arch) the minimum thickness requirement can be summarized in a graphical format, which can be used as a general solution.
4. The proposed procedure finds an arch or a shell of uniform thickness by looking for a least-squares closest-fit. The material demand on the realized form can be further reduced by relaxing the uniform thickness requirement to allow for bulking near the springing, while maintaining uniform thickness elsewhere.
5. A procedure was implemented to analyze two-dimensional compression only forms under wind loading. The procedure is capable of informing the suitability of the arch geometry (i.e. the sufficiency of thickness) and density to safely carry a given wind loading. The closest-fit thrust line generated in the process

indicate the validity of the closest-fit thrust line under combined gravity and wind loading, and if any changes are required to the geometry (i.e. increase thickness) or material (i.e. increase density).

5.2. Recommendations

The following recommendations can be made to build up on the findings presented in this thesis.

1. Physical model testing should be done to verify the suitability of the procedures presented here for providing feedback on the lateral load carrying capacities of compression-only forms.
2. The three-dimensional case of feedback on seismic loading would require further improvements to the discretization of the thrust network to improve the usefulness of the feedback given. This would be done using the COMPAS platform developed by Block Research Group at ETH, Zurich.
3. Extending the wind loading case from two-dimensional to three-dimensional case is not straight forward. A careful examination of the procedure for the two-dimensional case, along with a robust solving strategy would be required.
4. The possibility of a simplified presentation of wind load carrying capacities of compression-only shells should be explored. This may take the form of linear combinations of general solutions mimicking the idea of eigenshells.

REFERENCES

[1] S. Bagrianski and A. B. Halpern, “Form-finding of compressive structures using Prescriptive Dynamic Relaxation,” *Computers and Structures,* vol. 132, p. 65–74, 2014.

[2] K.-E. Kurrer, The History of the Theory of Structures, Berlin: Ernst and Sohn, 2008.

[3] S. Huerta, “Galileo was Wrong: The Geometrical Design of Masonry Arches,” *Nexus Network Journal,* vol. 8, pp. 25-52, 2006.

[4] M. Shaer, “A Secret Tunnel Found in Mexico May Finally Solve the Mysteries of Teotihuacán,” 2016. [Online]. Available: https://www.smithsonianmag.com/history/discovery-secret-tunnel-mexico-solve-mysteries-teotihuacan-180959070/. [Accessed 11 November 2017].

[5] N. Joseph, Science and Civilization in China: Volume 4, Physics and Physical Technology, Part 3, Civil Engineering and Nautics, Taipei: Caves Books, 1986.

[6] M. M. Motlagh, “www.sasanika.org,” 2011. [Online]. Available: https://www.sasanika.org/wp-content/uploads/e-sasanika-Arch-2-Mazhari-Motlagh.pdf. [Accessed 2017].

[7] D. Gamalath, Buddha Prathimagruhaye Avakashiya Sanvidhanaya, Colombo: S Godage and Brothers, 2016.

[8] P. Fernando and W. Dias, “Some Engineering Aspects of Ancient Structures,” in *6th International Conference on Structural Engineering and Construction Management*, Kandy, 2015.

[9] K. Upasena, “Development of Shell Structrures in Sri Lanka,” in *History of Engineering in Sri Lanka: Dr A N S Kulasinghe Felicitation Volume*, Institution of Engineers, Sri Lanka, 2001, pp. 107-140.

[10] A. Frearson, "Armadillo Vault is a pioneering stone structure that supports itself without any glue," DeZeen, 31 May 2016. [Online]. Available: https://www.dezeen.com/2016/05/31/armadillo-vault-block-research-group-eth-zurich-beyond-the-bending-limestone-structure-without-glue-venice-architecture-biennale-2016/. [Accessed 20 November 2018].

[11] S. Huerta, "The Analysis of Masonry Architecture: A Historical Approach," *Architectural Science Review,* vol. 51, no. 4, pp. 297-328, 2008.

[12] P. Block, T. Ciblac and J. Ochsendorf, "Real-time limit analysis of vaulted masonry buildings," *Computers and Structures,* vol. 84, pp. 1841-1852, 2006.

[13] A. De Luca, A. Giordano and E. Mele, "A simplified procedure for assessing the seismic capacity of masonry arches," *Engineering Structures* , vol. 26, p. 1915–1929, 2004.

[14] P. Roca, M. Cervera, G. Gariup and L. Pela, "Structural Analysis of Masonry Historical Constructions. Classical and Advanced Approaches," *Archives of Computational Methods in Engineering,* vol. 17, pp. 299-325, 2010.

[15] I. Mamaghani, O. Aydan and Y. Kajikawa, "Analysis of masonry structures under static and dynamic loading by discrete finite element method," *JSCE Structural Eng/Earthquake Eng,* vol. 16, no. 2, pp. 75-86, 1999.

[16] O'Dwyer, "Funicular analysis of masonry vaults," *Computers and Structures,* vol. 73, pp. 187-197, 1999.

[17] E. Whiting, J. Ochsendorf and F. Durand, "Procedural modeling of structurally-sound masonry buildings," *ACM Transactions on Graphics,* vol. 28, no. 5, 2009.

[18] M. Ramage, J. Ochsendorf, P. Rich, J. Bellamy and P. Block, "Design and construction of the Mapungubwe National Park Interpretive Centre, South Africa," *ATDF Journal,* vol. 7, no. 1/2, pp. 14-23, 2010.

[19] P. Block and J. Ochsendorf, "Thrust Network Analysis: A New Methodology for Three-Dimensional Equilibrium," *Journal of the IASS,* vol. 48, no. 3, 2007.

[20] Y. Liu, H. Pan, J. Snyder, W. Wang and B. Guo, "Computing Self-Supporting Surfaces by Regular Triangulation," *ACM Transactions on Graphics,* vol. 32, no. 4, 2013.

[21] L. Ney and S. Adriaenssens, "Shaping Force," in *Shell Structures for Architecture,* S. Adriaenssens, P. Block, D. Veenendaal and C. Williams, Eds., New York, Routledge, 2014, pp. 15-20.

[22] P. Block, "Thrust Network Analysis," Boston, 2009.

[23] A. Kilian and J. Ochsendorf, "Particle-spring Systems for Structural Form Finding," *Journal of the IASS,* vol. 46, 2005.

[24] P. Roca, A. Andreu and L. Gil, "Limit Analysis of Masonry Constructions by 3D Funicular Modelling," in *Structural Analysis of Historical Constructions,* New Delhi, 2006.

[25] S. Adriaenssens, P. Block, D. Veenendaal and C. Williams, Eds., Shell Structures for Architecture, New York: Routledge, 2014.

[26] D. Veenendaal and P. Block, "Comparison of Form-Finding Methods," in *Shell Structures for Architecture,* S. Adriaenssens, P. Block, D. Veenendaal and C. Williams, Eds., New York, Routledge, 2014, pp. 115-130.

[27] Schek and H-J, "The force density method for form finding and computation of general networks," *Computer Methods in Applied Mechanics,* pp. 115-134, 1974.

[28] P. Block, L. Lachauer and Rippmann, "Thrust Network Analysis: Design of a cut-stone masonry vault," in *Shell Structures for Architecture,* New York, Routledge, 2014, pp. 71-87.

[29] R. J. Wilson, “Planarity,” in *Introduction to graph theory*, 4th ed., Harlow, Essex, Longman, 1996, pp. 60-80.

[30] W. Whiteley, P. F. Ash, E. Bolker and H. Crapo, “Convex polyhedra, Dirichlet tessellations, and spider webs,” in *Shaping spaces,* Springer, 2013, pp. 231-251.

[31] H. Whitney, “Congruent graphs and the connectivity of graphs,” *Americal Journal of Mathematics,* vol. 54, no. 1, pp. 150-168, 1932.

[32] P. Block and L. Lachauer, “Three-dimensional funicular analysis of masonry vaults,” *Mechanics Research Communications,* vol. 56, pp. 53-60, 2014.

[33] T. Van Mele and P. Block, “Algebraic graph statics,” *Computer-Aided Design,* vol. 53, pp. 104-116, 2014.

[34] R. Penrose, “A generalized inverse for matrices,” *Proceedings of the Cambridge Philosophical Society,* vol. 51, no. 3, pp. 406-413, 1955.

[35] F. Marmo and L. Rosati, “Reformulation and extension of the thrust network analysis,” *Computers and Structures,* vol. 182, pp. 104-118, 2017.

[36] J. W. Eaton, D. Bateman, S. Hauberg and R. Wehbring, *GNU Octave version 4.2.2 manual: a high-level interactive language for numerical computations,* 2018.

[37] J. Hearon, “Generalized inverses and solutions of linear systems,” *Journal of Research of the National Bureau of Standards-B. Mathematical Sciences,* vol. 72B, no. 4, pp. 303-308, 1968.

[38] M. Wild, “Generating all cycles, chordless cycles, and Hamiltonian cycles with the principle of exclusion,” *Journal of Discrete Algorithms,* vol. 6, pp. 93-102, 2008.

[39] K. Pawel, *Null space of a sparse matrix,* MATLAB Central File Exchange, 2006.

[40] C. Gotsman and S. Toledo, “On the computation of null spaces of sparse rectangular matrices,” *SIAM Journal of Matrix Analysis and Applications,* vol. 30, no. 2, pp. 445-463, 2008.

[41] J. D'Errico, *rowspaces,* MATLAB Central File Exchange, 2007.

[42] J. Nocedal and S. J. Wright, Numerical Optimization, 2nd ed., New York: Springer, 2006.

[43] H. Tamai, “Advanced application of the force density method in multidisciplinary design practice by incorporating with optimization using analystical derivatives,” in *Proceedings of the IASS Symposium 2013,* Wroclaw, Poland, 2013.

[44] T. Van Mele, D. Panozzo, O. Sorkine-Hornung and P. Block, “Best-fit thrust network analysis; rationalization of freeform meshes,” in *Shell Structures for Architecture,* New York, Routledge, 2014, pp. 157-168.

[45] M. J. DeJong, “Seismic Assessment Strategies for Masonry Structures,” Boston, 2009.

[46] S. Huerta, “The use of simple models in the teaching of the essentials of masonry arch behaviour,” in *Theory and practice of construction: knowledge, means and models,* Ravenna, 2005.

[47] J. Ochsendorf, “Collapse of Masonry Arches,” Cambridge, 2002.

[48] T. Michiels and S. Adriaenssens, “Form-finding algorithm for masonry arches subjected to in-plane earthquake loading,” *Computers and Structures,* pp. 85-98, 2018.

[49] T. Michiels, S. Adriaenssens and J. J. Jorquera-Lucerga, “Parametric study of masonry shells form-found for seismic loading,” *Journal of the International Association for Shell and Spatial Structures,* 2017.

[50] T. Michiels and S. Adriaenssens, "Identification off key design parameters for earthquake resistance of reinforced concrete shell structures," *Engineering Structures,* pp. 411-420, 2013.

[51] S. Coccia, M. Como and F. Di Carlo, "Wind Strength of Gothic Cathedrals," *Engineering Failure Analysis,* vol. 55, pp. 1-25, 2015.

[52] *Design buildings for high winds,* Ministry of local government, housing and construction, Sri Lanka, 1978.

[53] W. Maduranga and C. Lewangamage, "Development of wind loading maps for Sri Lanka for use with different wind loading codes," *Engineer,* vol. LI, no. 03, pp. 41-49, 2018.

[54] G. L. Johnson, D. Surry and W. K. Ng, "Turbulent Wind Loads on Arch-Roof Structures: A Review of Model and Full-Scale Results, and the Effect of Reynolds Number," in *5th US National Conference on Wind Engineering,* Lubbock, TX, 1985.

[55] A. Abrahm, N. R. Iyer, G. M. S. Knight, K. Muthumani and N. Lakshmanan, "Wind Loads on Curved Roods: Effect of Side Walls," in *8th Asia-Pacific Conference on Wind Engineering,* Chennai, INDIA, 2013.

[56] P. A. Blackmore and E. Tsokri, "Wind Loads on Curved Roofs," *Journal of Wind Engineering and Industrial Aerodynamics,* no. 94, pp. 833-844, 2006.

[57] N. Toy, W. D. Moss and E. Savory, "Wind Tunnel Studies on a Dome in Turbulent Boundary Layers," *Journal of Wind Engineering and Industrial Aerodynamics,* no. 11, pp. 201-212, 1983.

[58] T. Taylor, "Wind Pressures on a Hemispherical Dome," *Journal of Wind Engineering and Industrial Aerodynamics,* no. 40, pp. 199-213, 1991.

[59] C. M. Cheng, C. L. Fu and Y. Y. Lin, "Characteristic of Wind Load on a Hemispherical Dome in Smooth Flow and Turbulent Boundary Layer Flow," in

BBAA VI International Colloquium on: Bluff Boddies Aerodynamics and Applications, Milano, Italy, 2008.

[60] C. Letchford and P. P. Sarkar, “Mean and fluctuating Wind Loads on Rough and Smooth Parabolic Domes,” *Journal of WInd Engineering and Industrial Aerodynamics,* no. 88, pp. 101-117, 2000.

[61] A. Rodrigues, A. Tome and M. Gomes, “Computational Study of the Wind Load on a Free-Form Complex Thin Shell Structure,” *Wind and Structures,* vol. 25, no. 2, pp. 177-193, 2017.

[62] F. Maher, “Wind Loads on Basic Dome Shapes,” *Journal of Structural Division ASCE ST3,* pp. 219-228, 1965.

[63] *MATLAB 2015a,* The MathWorks Inc., Natick, Massachusetts, United States.

[64] K. D. W. Nandalal and H. Abeyruwan, “An attempt towards wind zone demarcation for Sri Lanka,” 2010.

[65] B. S. Institution, *BS6399-2:1997 Loading for buildings. Part 2: Code of practice for wind loads,* London, England: BSI, 1997.

[66] J. Heyman, The Masonry Arch, Chichester: Ellis Horwood Limited, 1982.

[67] K.-U. Bletzinger and E. Ramm, “Computational form finding and optimization,” in *Shell Structures for Architecture,* New York, Routledge, 2014, pp. 45-55.

[68] W. F. Baker, L. L. Beghini, A. Mazurek, J. Carrion and A. Beghini, “Structural Innovation: Combining Classic Theories with New Technologies,” *Engineering Journal, American Institute of Steel Construction,* vol. 52, pp. 203-217, 2015.

[69] A. Tomás and P. Martí, “Shape and size optimisation of concrete shells,” *Engineering Structures,* vol. 32, pp. 1650-1658, 2010.

[70] P. Michalatos and S. Kaijima, “Eigenshells; Structural patterns and modal forms,” in *Shell Structures for Architecture*, New York, Routledge, 2014, pp. 195-209.

[71] A. Pugnale, T. Echengucia and M. Sassone, “Computational morphogenesis; Design of freeform surfaces,” in *Shell structures for architecture*, New York, Routledge, 2014, pp. 225-236.

[72] J. N. Richardson, S. Adriaenssens, R. F. Coelho and P. Bouillard, “Coupled form-finding and grid optimization approach for single layer grid shells,” *Engineering Structures*, vol. 52, pp. 230-239, 2013.

[73] P. Winslow, “Multi-criteria gridshell optimization,” in *Shell Structures for Architecture*, New York, Routledge, 2014, pp. 181-193.

[74] J. Richardson, S. Adriaenssens, R. Coelho and P. Bouillard, “Discrete topology optimization; connectivity for gridshells,” in *Shell Structures for Architecture*, New York, Routledge, 2014, pp. 171-179.

[75] P. Winslow, S. Pellegrino and S. Sharma, “Multi-Objective Optimization of Free-Form Grid Structures,” in *EngOpt 2008 - International Conference on Engineering Optimization*, Rio de Janeiro, 2008.

[76] M. Dini, G. Estrada, M. Froli and N. Baldassini, “Form-finding and buckling optimisation of gridshells using genetic algorithms,” in *Proceedings of the International Association for Shell and Spatial Structures (IASS) Symposium 2013 „BEYOND THE LIMITS OF MAN”*, Wrocław, 2013.

[77] J. N. Richardson, S. Adriaenssens, P. Bouillard and R. F. Coelho, “Multiobjective topology optimization of truss structures with kinematic stability repair,” *Struct Multidisc Optim*, vol. 46, pp. 513-532, 2012.

[78] M. Vyzantiadoua, A. Avdelasa and S. Zafiropoulos, “The application of fractal geometry to the design of grid or reticulated shell structures,” *Computer-Aided Design,* vol. 39, pp. 51-59, 2007.

[79] P. Block and L. Lachauer, “Closest-Fit, Compression-Only Solutions for Freeform Shells,” in *Proceedings of the IABSE-IASS Symposium 2011,* London, 2011.

[80] P. Cuvilliers, R. Danhaive and C. Mueller, “Gradient-based optimization of closest-fit funicular structures,” in *Proceedings of the IASS Annual Symposium 2016 “Spatial Structures in the 21st Century”*, Tokyo, 2016.

[81] F. Fraternali, “A thrust network approach to the equilibrium problem of unreinforced masonry vaults via polyhedral stress functions,” *Mechanics Research Communications,* vol. 37, pp. 198-204, 2010.

[82] A. Borgart, M. de Leuw and P. Hoogenboom, “The relationship of form and force in (irregular) curved surfaces,” in *Proceedings of the 5th International Conference on Computation of Shell and Spatial Structures,* Salzburg, 2005.

[83] D. Kelly and M. Tosh, “Interpreting load paths and stress trajectories in elasticity,” *Engineering Computations,* vol. 17, no. 2, pp. 117-135, 2000.

[84] K. Gharibi, J. Hurley and A. Tamijani, “Determination of Load Paths in Plates and Shells Using Load Path Functions,” in *58th AIAA/ASCE/AHS/ASC Structures, Structural Dynamics, and Materials Conference*, Texas, 2017.

[85] I. Lochner-Aldinger and A. Schumacher, “Homogenization method; distribution of material densities,” in *Shell Structures for Architecture,* New York, Routledge, 2014, pp. 211-223.

APPENDIX A: DETERMINING THE DUAL FORCE DIAGRAM OF A THRUST NETWORK

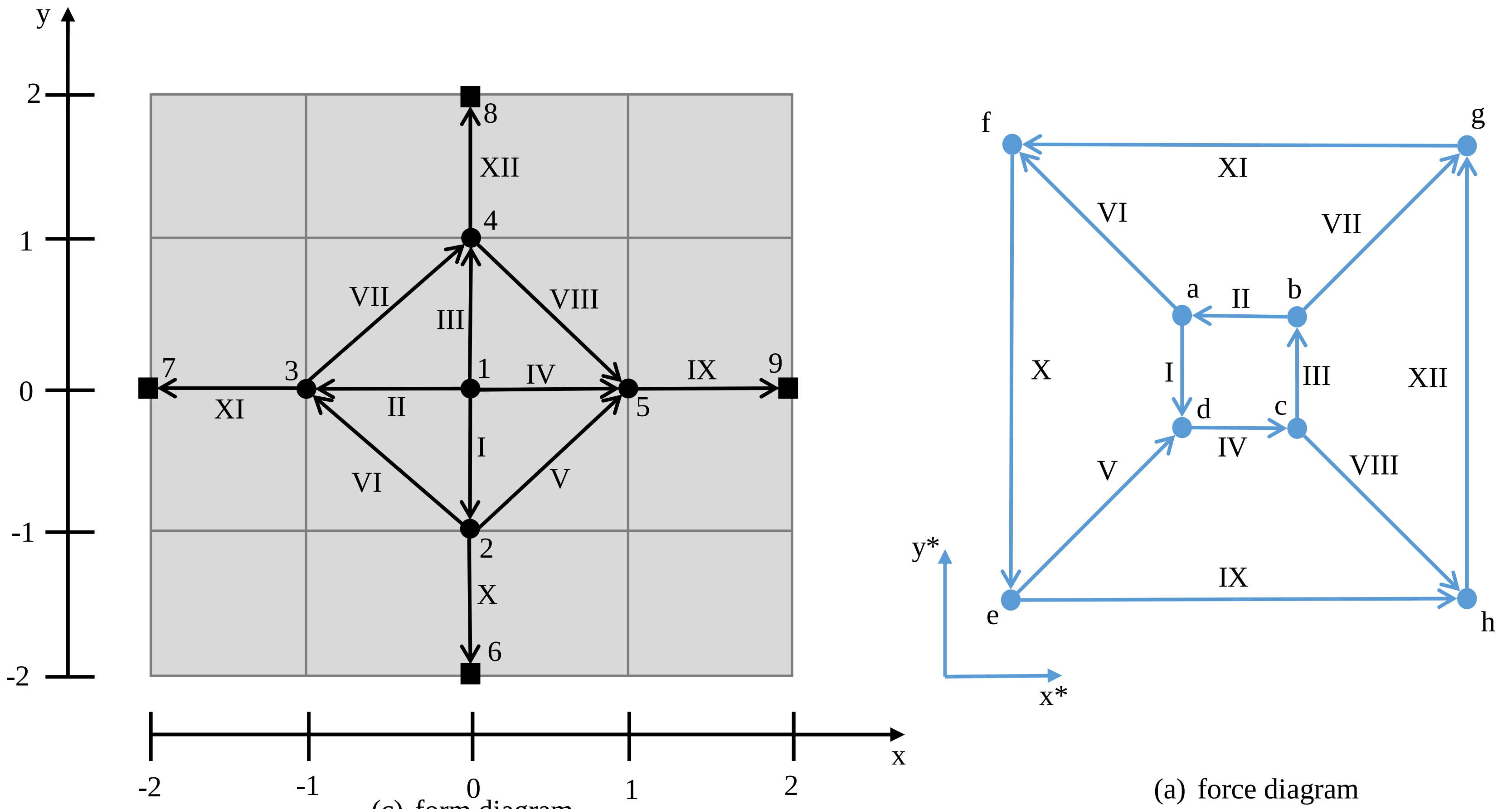

(c) form diagram

(a) force diagram

Figure A.2: (a) Form and (b) force diagrams of an example thrust network. Network contains 12 members, 5 internal nodes and 4 boundary nodes.

Construct topology

Branch-node adjacency matrix (C) as defined in equation 3.1, of the form diagram in Figure A.1 is given in equation A.1. The columns correspond to nodes while rows correspond to branches of the form diagram.

$$C = \begin{array}{cc} \begin{bmatrix} 1 & -1 & 0 & 0 & 0 & 0 & 0 & 0 & 0 \\ 1 & 0 & -1 & 0 & 0 & 0 & 0 & 0 & 0 \\ 1 & 0 & 0 & -1 & 0 & 0 & 0 & 0 & 0 \\ 1 & 0 & 0 & 0 & -1 & 0 & 0 & 0 & 0 \\ 0 & 1 & 0 & 0 & -1 & 0 & 0 & 0 & 0 \\ 0 & 1 & -1 & 0 & 0 & 0 & 0 & 0 & 0 \\ 0 & 0 & 1 & -1 & 0 & 0 & 0 & 0 & 0 \\ 0 & 0 & 0 & 1 & -1 & 0 & 0 & 0 & 0 \\ 0 & 0 & 0 & 0 & 1 & 0 & 0 & 0 & -1 \\ 0 & 1 & 0 & 0 & 0 & -1 & 0 & 0 & 0 \\ 0 & 0 & 1 & 0 & 0 & 0 & -1 & 0 & 0 \\ 0 & 0 & 0 & 1 & 0 & 0 & 0 & -1 & 0 \end{bmatrix} & \begin{matrix} \boldsymbol{I} \\ \boldsymbol{II} \\ \boldsymbol{III} \\ \boldsymbol{IV} \\ \boldsymbol{V} \\ \boldsymbol{VI} \\ \boldsymbol{VII} \\ \boldsymbol{VIII} \\ \boldsymbol{IX} \\ \boldsymbol{X} \\ \boldsymbol{XI} \\ \boldsymbol{XII} \end{matrix} \\ \begin{matrix} \mathbf{1} & \mathbf{2} & \mathbf{3} & \mathbf{4} & \mathbf{5} & \mathbf{6} & \mathbf{7} & \mathbf{8} & \mathbf{9} \end{matrix} & \end{array} \tag{A.1}$$

$$C_i = \begin{bmatrix} 1 & -1 & 0 & 0 & 0 \\ 1 & 0 & -1 & 0 & 0 \\ 1 & 0 & 0 & -1 & 0 \\ 1 & 0 & 0 & 0 & -1 \\ 0 & 1 & 0 & 0 & -1 \\ 0 & 1 & -1 & 0 & 0 \\ 0 & 0 & 1 & -1 & 0 \\ 0 & 0 & 0 & 1 & -1 \\ 0 & 0 & 0 & 0 & 1 \\ 0 & 1 & 0 & 0 & 0 \\ 0 & 0 & 1 & 0 & 0 \\ 0 & 0 & 0 & 1 & 0 \end{bmatrix} \tag{A.2}$$

Solve for horizontal equilibrium

Nodal cordinate vectors (*x*, *y*) of the form diagram in Figure A.1 is as in equation A.3 and A.4.

$$x = [0 \quad 0 \quad -1 \quad 0 \quad 1 \quad 0 \quad -2 \quad 0 \quad 2]^T \tag{A.3}$$

$$y = [0 \quad -1 \quad 0 \quad 1 \quad 0 \quad -2 \quad 0 \quad 2 \quad 0]^T \tag{A.4}$$

Branch length vectors (*u*, *v*) of the form diagram in Figure A.1 is as in equation A.5 and A.6.

$$u = Cx = \; [0 \quad 1 \quad 0 \quad -1 \quad -1 \quad 1 \quad -1 \quad -1 \quad -1 \quad 0 \quad 1 \quad 0]^T \tag{A.5}$$

$$v = Cy = \; [1 \quad 0 \quad -1 \quad 0 \quad -1 \quad -1 \quad -1 \quad 1 \quad 0 \quad 1 \quad 0 \quad -1]^T \tag{A.6}$$

Thus, matrix *A* as defined in equation 3.11 for the form in Figure A.1 is as given in equation A.7.

$$A = \begin{bmatrix} C_i^T U \\ C_i^T V \end{bmatrix} = \begin{bmatrix} 0 & 1 & 0 & -1 & 0 & 0 & 0 & 0 & 0 & 0 & 0 & 0 \\ 0 & 0 & 0 & 0 & -1 & 1 & 0 & 0 & 0 & 0 & 0 & 0 \\ 0 & -1 & 0 & 0 & 0 & -1 & -1 & 0 & 0 & 0 & 1 & 0 \\ 0 & 0 & 0 & 0 & 0 & 0 & 1 & -1 & 0 & 0 & 0 & 0 \\ 0 & 0 & 0 & 1 & 1 & 0 & 0 & 1 & -1 & 0 & 0 & 0 \\ 1 & 0 & -1 & 0 & 0 & 0 & 0 & 0 & 0 & 0 & 0 & 0 \\ -1 & 0 & 0 & 0 & -1 & -1 & 0 & 0 & 0 & 1 & 0 & 0 \\ 0 & 0 & 0 & 0 & 0 & 1 & -1 & 0 & 0 & 0 & 0 & 0 \\ 0 & 0 & 1 & 0 & 0 & 0 & 1 & 1 & 0 & 0 & 0 & -1 \\ 0 & 0 & 0 & 0 & 1 & 0 & 0 & -1 & 0 & 0 & 0 & 0 \end{bmatrix} \tag{A.7}$$

The dimensions and rank of matrix A in equation A.7 are 12 and 9 respectively. From rank-nullity theorem, nullity of A (i.e. the dimensions of the null space of A) is equal to 3 (equation A.9).

$$dim(null(A)) = \dim(A) - rank(A) = 12 - 9 = 3 \tag{A.8}$$

Thus, there are three independent force densities in the force network shown in Figure A.1.

$$null(A) = \begin{bmatrix} -0.0276 & -0.2301 & 0.5288 \\ -0.2102 & 0.4237 & 0.3310 \\ -0.0276 & -0.2301 & 0.5288 \\ -0.2102 & 0.4237 & 0.3310 \\ 0.2556 & 0.0320 & -0.1303 \\ 0.2556 & 0.0320 & -0.1303 \\ 0.2556 & 0.0320 & -0.1303 \\ 0.2556 & 0.0320 & -0.1303 \\ 0.3009 & 0.4877 & 0.0704 \\ 0.4835 & -0.1662 & 0.2681 \\ 0.3009 & 0.4877 & 0.0704 \\ 0.4835 & -0.1662 & 0.2681 \end{bmatrix} \tag{A.9}$$

Null space of A represents the span of the solutions satisfying equation 3.11. I.e. taking any linear combination of the column vectors in *null(A)* as q would satisfy the equation $\boldsymbol{Aq = 0}$. Each row of *null(A)* correspond to the force density in the corresponding branch of the form diagram or length of the corresponding element in the force diagram (see Figure A.1).

Hence, the linearly independent rows of *null(A)* would correspond to the independent branches of the form diagram (or force diagram by duality). It was identified that rows 3, 9, 10 of *null(A)* are a set of independent rows, and corresponds to branches III, IX and X. Note that this choice is not unique (another possible choice is I, II, VII).

$$A_{ind} = \begin{array}{c} \begin{matrix} \textbf{III} & \textbf{IX} & \textbf{X} \end{matrix} \\ \begin{bmatrix} 0 & 0 & 0 \\ 0 & 0 & 0 \\ 0 & 0 & 0 \\ 0 & 0 & 0 \\ 0 & -1 & 0 \\ -1 & 0 & 0 \\ 0 & 0 & 1 \\ 0 & 0 & 0 \\ 1 & 0 & 0 \\ 0 & 0 & 0 \end{bmatrix} \end{array} \tag{A.10}$$

$$A_d{}^{+} = \begin{bmatrix} 0 & 0 & 0 & 0 & 0 & 1 & 0 & 0 & 0 & 0 \\ 1 & 0.5 & 0 & 0.5 & 1 & 1 & 1 & 0.5 & 0 & 0.5 \\ 0 & 0.5 & 0 & 0.5 & 1 & 1 & 1 & 0.5 & 0 & 0.5 \\ 0 & -0.375 & 0 & -0.125 & 0 & -0.5 & -0.5 & -0.125 & 0 & 0.125 \\ 0 & 0.375 & 0 & 0.125 & 0 & -0.5 & -0.5 & 0.125 & 0 & -0.125 \\ 0 & 0.125 & 0 & 0.375 & 0 & -0.5 & -0.5 & -0.625 & 0 & -0.375 \\ 0 & -0.125 & 0 & -0.375 & 0 & -0.5 & -0.5 & -0.375 & 0 & -0.625 \\ 1 & 1 & 1 & 1 & 1 & 0 & 0 & 0 & 0 & 0 \\ 0 & 0 & 0 & 0 & 0 & -1 & -1 & -1 & -1 & -1 \end{bmatrix} \tag{A.11}$$

Now we can make a choice on q_{ind} and determine q satisfying equation 3.11 (i.e. self-stressed equilibrium in horizontal direction)

$$q_{dep} = \begin{array}{ccc} \textbf{III} & \textbf{IX} & \textbf{X} \\ [1 & 4 & 4]^T \end{array} \tag{A.12}$$

$$q_{ind} = \begin{array}{ccccccccc} \textbf{I} & \textbf{II} & \textbf{IV} & \textbf{V} & \textbf{VI} & \textbf{VII} & \textbf{VIII} & \textbf{XI} & \textbf{XII} \\ [1 & 1 & 1 & 1.5 & 1.5 & 1.5 & 1.5 & 4 & 4]^T \end{array} \tag{A.13}$$

Thus, the self-equilibrating force densities in horizontal direction are as in equation A.14, given the force densities in branches III, IX and X are as given in equation A.12.

$$q = [1 \quad 1 \quad 1 \quad 1 \quad 1.5 \quad 1.5 \quad 1.5 \quad 1.5 \quad 4 \quad 4 \quad 4 \quad 4]^T \tag{A.14}$$

The force density vector (*q*) can be transformed to a member force vector (*f*) by multiplying each element of the *q* by the corresponding member length.

$$L = \sqrt{uu^T + vv^T} = [1 \quad 1 \quad 1 \quad 1 \quad 1.414 \quad 1.414 \quad 1.414 \quad 1.414 \quad 1 \quad 1 \quad 1 \quad 1]^T \tag{A.15}$$

$$f = [1 \quad 1 \quad 1 \quad 1 \quad 2.121 \quad 2.121 \quad 2.121 \quad 2.121 \quad 4 \quad 4 \quad 4 \quad 4]^T \tag{A.16}$$

By the duality between force and form diagrams, the vector *f* is graphically represented in the force diagram in Figure A.1.

Coordinates of the force diagram

The connectivity of the force diagram can be presented in the form of a branch node adjacency matrix (C^* - see equation A.17). This is generated manually by following the rules of graphic statics.

$$C^* = \begin{array}{cc} \begin{bmatrix} 1 & 0 & 0 & -1 & 0 & 0 & 0 & 0 \\ -1 & 1 & 0 & 0 & 0 & 0 & 0 & 0 \\ 0 & -1 & 1 & 0 & 0 & 0 & 0 & 0 \\ 0 & 0 & -1 & 1 & 0 & 0 & 0 & 0 \\ 0 & 0 & 0 & -1 & 1 & 0 & 0 & 0 \\ 1 & 0 & 0 & 0 & 0 & -1 & 0 & 0 \\ 0 & 1 & 0 & 0 & 0 & 0 & -1 & 0 \\ 0 & 0 & 1 & 0 & 0 & 0 & 0 & -1 \\ 0 & 0 & 0 & 0 & 1 & 0 & 0 & -1 \\ 0 & 0 & 0 & 0 & -1 & 1 & 0 & 0 \\ 0 & 0 & 0 & 0 & 0 & -1 & 1 & 0 \\ 0 & 0 & 0 & 0 & 0 & 0 & -1 & 1 \end{bmatrix} & \begin{matrix} \boldsymbol{I} \\ \boldsymbol{II} \\ \boldsymbol{III} \\ \boldsymbol{IV} \\ \boldsymbol{V} \\ \boldsymbol{VI} \\ \boldsymbol{VII} \\ \boldsymbol{VIII} \\ \boldsymbol{IX} \\ \boldsymbol{X} \\ \boldsymbol{XI} \\ \boldsymbol{XII} \end{matrix} \\ \begin{matrix} \mathbf{a} & \mathbf{b} & \mathbf{c} & \mathbf{d} & \mathbf{e} & \mathbf{f} & \mathbf{g} & \mathbf{h} \end{matrix} & \end{array} \tag{A.17}$$

To fully define the force diagram nodal coordinate vectors x^* and y^* corresponding to the force diagram should also be determined. This can be done by either scaling of the values from force diagram or algebraically, as explained next.

We can first determine the branch vectors u* and v*, considering the parallelism between corresponding members in the force and form diagrams (see equation 3.2 and 3.3).

$$u^* = Uq = \begin{bmatrix} 0 & 0 & 0 & 0 & 0 & 0 & 0 & 0 & 0 & 0 & 0 & 0 \\ 0 & 1 & 0 & 0 & 0 & 0 & 0 & 0 & 0 & 0 & 0 & 0 \\ 0 & 0 & 0 & 0 & 0 & 0 & 0 & 0 & 0 & 0 & 0 & 0 \\ 0 & 0 & 0 & -1 & 0 & 0 & 0 & 0 & 0 & 0 & 0 & 0 \\ 0 & 0 & 0 & 0 & -1 & 0 & 0 & 0 & 0 & 0 & 0 & 0 \\ 0 & 0 & 0 & 0 & 0 & 1 & 0 & 0 & 0 & 0 & 0 & 0 \\ 0 & 0 & 0 & 0 & 0 & 0 & -1 & 0 & 0 & 0 & 0 & 0 \\ 0 & 0 & 0 & 0 & 0 & 0 & 0 & -1 & 0 & 0 & 0 & 0 \\ 0 & 0 & 0 & 0 & 0 & 0 & 0 & 0 & -1 & 0 & 0 & 0 \\ 0 & 0 & 0 & 0 & 0 & 0 & 0 & 0 & 0 & 0 & 0 & 0 \\ 0 & 0 & 0 & 0 & 0 & 0 & 0 & 0 & 0 & 0 & 1 & 0 \\ 0 & 0 & 0 & 0 & 0 & 0 & 0 & 0 & 0 & 0 & 0 & 0 \end{bmatrix} \begin{bmatrix} 1 \\ 1 \\ 1 \\ 1 \\ 1.5 \\ 1.5 \\ 1.5 \\ 1.5 \\ 4 \\ 4 \\ 4 \\ 4 \end{bmatrix} = \begin{bmatrix} 0 \\ 1 \\ 0 \\ -1 \\ -1.5 \\ 1.5 \\ -1.5 \\ -1.5 \\ -4 \\ 0 \\ 4 \\ 0 \end{bmatrix} \tag{A.18}$$

$$v^* = Vq = \begin{bmatrix} 1 & 0 & 0 & 0 & 0 & 0 & 0 & 0 & 0 & 0 & 0 & 0 \\ 0 & 0 & 0 & 0 & 0 & 0 & 0 & 0 & 0 & 0 & 0 & 0 \\ 0 & 0 & -1 & 0 & 0 & 0 & 0 & 0 & 0 & 0 & 0 & 0 \\ 0 & 0 & 0 & 0 & 0 & 0 & 0 & 0 & 0 & 0 & 0 & 0 \\ 0 & 0 & 0 & 0 & -1 & 0 & 0 & 0 & 0 & 0 & 0 & 0 \\ 0 & 0 & 0 & 0 & 0 & -1 & 0 & 0 & 0 & 0 & 0 & 0 \\ 0 & 0 & 0 & 0 & 0 & 0 & -1 & 0 & 0 & 0 & 0 & 0 \\ 0 & 0 & 0 & 0 & 0 & 0 & 0 & 1 & 0 & 0 & 0 & 0 \\ 0 & 0 & 0 & 0 & 0 & 0 & 0 & 0 & 0 & 0 & 0 & 0 \\ 0 & 0 & 0 & 0 & 0 & 0 & 0 & 0 & 0 & 1 & 0 & 0 \\ 0 & 0 & 0 & 0 & 0 & 0 & 0 & 0 & 0 & 0 & 0 & 0 \\ 0 & 0 & 0 & 0 & 0 & 0 & 0 & 0 & 0 & 0 & 0 & -1 \end{bmatrix} \begin{bmatrix} 1 \\ 1 \\ 1 \\ 1 \\ 1.5 \\ 1.5 \\ 1.5 \\ 1.5 \\ 4 \\ 4 \\ 4 \\ 4 \end{bmatrix} = \begin{bmatrix} 1 \\ 0 \\ -1 \\ 0 \\ -1.5 \\ -1.5 \\ -1.5 \\ 1.5 \\ 0 \\ 4 \\ 0 \\ -4 \end{bmatrix} \tag{A.19}$$

However,

$$u^* = C^* x^* \tag{A.20}$$

The adjacency matrix *C** is not a square matrix and thus is not invertible to directly determine *x**. The rank of the branch-node adjacency matrix is equal to difference between the number of members and the first Betti number of the graph. Thus, the rank of matrix C* for the force diagram in Figure A.1 is equal to 7 (= $m - b_0 = m - (m - n + k) = 8 - 1$). Considering the 7 linearly independent rows in *C**, and the corresponding elements in branch length vector *u**, equation A.20 can be reformed as in equation A.21.

$$u_{ind}{}^{*} = C_{ind}{}^{*}x^{*} \tag{A.21}$$

The system of equations represented by equation A.21 is an underdetermined system as the number of equations (seven) is lesser than the number of variables (eight *x**-coordinates). By specifying one *x** coordinate the system can be made a determinate system with the possibility of a unique solution. In fact, a unique system would exist as the system of equations are independent.

$$u_{ind}{}^{*} = C^{*}{}_{ind,\ 2:8}x^{*}{}_{2:8} + C^{*}{}_{ind,1}x^{*}{}_{1}$$

$$x^{*}{}_{2:8} = inv(C^{*}{}_{ind,\ 2:8})\left(u_{ind}{}^{*} - C^{*}{}_{ind,1}x^{*}{}_{1}\right) \tag{A.22}$$

In equation A.22, $x^{*}{}_{2:8}$ denotes 2nd to 8th elements in *x** and $C^{*}{}_{ind,\ 2:8}$ denotes the intersection of the independent rows and 2nd to 8th column in *C**. Taking the *x** coordinate of node *a* of the force diagram as -0.5, the *x** nodal coordinate vector is as in equation A.23.

$$x^{*} = [-0.5 \quad 0.5 \quad 0.5 \quad -0.5 \quad -2.0 \quad -2.0 \quad 2.0 \quad 2.0]^{T} \tag{A.23}$$

By similar procedure, taking the *y** coordinate of node *a* of the force diagram as 0.5, the *y** nodal coordinate vector is as in equation A.24.

$$y^{*} = [0.5 \quad 0.5 \quad -0.5 \quad -0.5 \quad -2.0 \quad 2.0 \quad 2.0 \quad -2.0]^{T} \tag{A.24}$$

The alternative approach would be to carry out the minimization procedures in equations 3.6 through 3.10. However, the matrix Aeq, presented in equation A.25 is a 34 x 36 matrix and operating on this would be highly inefficient.

$$A_{eq} =$$

$$\begin{bmatrix}
1&&&&&&&&&&&&&&&&&&&&&&&&0 \\
&1&&&&&&&&&&&&&&&&&&&&&&&&-1 \\
&&1&&&&&&&&&&&&&&&&&&&&&&&&0 \\
&&&1&&&&&&&&&&&&&&&&&&&&&&&&1 \\
&&&&1&&&&&&&&&&&&&&&&&&&&&&&&1 \\
&&&&&1&&&&&&&&&&&&&&&&&&&&&&&&-1 \\
&&&&&&1&&&&&&&&&&&&&&&&&&&&&&&&1 \\
&&&&&&&1&&&&&&&&&&&&&&&&&&&&&&&&1 \\
&&&&&&&&1&&&&&&&&&&&&&&&&&&&&&&&&1 \\
&&&&&&&&&1&&&&&&&&&&&&&&&&&&&&&&&&0 \\
&&&&&&&&&&1&&&&&&&&&&&&&&&&&&&&&&&&-1 \\
&&&&&&&&&&&1&&&&&&&&&&&&&&&&&&&&&&&&0 \\
&&&&&&&&&&&&1&&&&&&&&&&&&-1 \\
&&&&&&&&&&&&&1&&&&&&&&&&&&0 \\
&&&&&&&&&&&&&&1&&&&&&&&&&&&1 \\
&&&&&&&&&&&&&&&1&&&&&&&&&&&&0 \\
&&&&&&&&&&&&&&&&1&&&&&&&&&&&&1 \\
&&&&&&&&&&&&&&&&&1&&&&&&&&&&&&1 \\
&&&&&&&&&&&&&&&&&&1&&&&&&&&&&&&1 \\
&&&&&&&&&&&&&&&&&&&1&&&&&&&&&&&&-1 \\
&&&&&&&&&&&&&&&&&&&&1&&&&&&&&&&&&0 \\
&&&&&&&&&&&&&&&&&&&&&1&&&&&&&&&&&&-1 \\
&&&&&&&&&&&&&&&&&&&&&&1&&&&&&&&&&&&0 \\
&&&&&&&&&&&&&&&&&&&&&&&1&&&&&&&&&&&&1 \\
1&1&1&1&0&0&0&0&0&0&0&0 \\
-1&0&0&0&1&1&0&0&0&1&0&0 \\
0&-1&0&0&0&-1&1&0&0&0&1&0 \\
0&0&-1&0&0&0&-1&1&0&0&0&1 \\
0&0&0&-1&-1&0&0&-1&1&0&0&0 \\
&&&&&&&&&&&&1&1&1&1&0&0&0&0&0&0&0&0 \\
&&&&&&&&&&&&-1&0&0&0&1&1&0&0&0&1&0&0 \\
&&&&&&&&&&&&0&-1&0&0&0&-1&1&0&0&0&1&0 \\
&&&&&&&&&&&&0&0&-1&0&0&0&-1&1&0&0&0&1 \\
&&&&&&&&&&&&0&0&0&-1&-1&0&0&-1&1&0&0&0
\end{bmatrix} \quad (A.25)$$